

MATER. TEHNOL.	LETNIK VOLUME	42	ŠTEV. NO.	1	STR. P.	1–47	LJUBLJANA SLOVENIJA	JAN.-FEB. 2008
-------------------	------------------	----	--------------	---	------------	------	------------------------	-------------------

**VSEBINA – CONTENTS*****IZVIRNI ZNANSTVENI ČLANKI – ORIGINAL SCIENTIFIC ARTICLES*****A failure criterion for single-crystal superalloys during thermocyclic loading**

Merilo za prelom monokristala superzlitine pri termociklični obremenitvi

L. Getsov, A. Semenov, A. Staroselsky ..... 3

**Accelerated creep testing of new creep resisting weld metals**

Preizkusi pospešenega lezenja zvarov novega jekla, odpornega proti lezenju

S. T. Mandziej, A. Výrostková, M. Šolar ..... 13

**Zveza med analiznimi rezultati – karbonatna bomba in termična analiza**

Connection between analysis results – carbonate bomb and thermal analysis

Ž. Pogačnik ..... 27

***STROKOVNI ČLANKI – PROFESSIONAL ARTICLES*****Developing and testing a new type-8K mould for tool-steel ingot casting**

Razvoj in preizkus nove kokile vrste 8K za ulivanje ingotov iz orodnega jekla

M. Balcar, L. Sochor, R. Železný, P. Fila, L. Martínek, L. Kraus, D. Kešner, J. Bažan ..... 33

**An AES investigation of brushed AISI 304 stainless steel after corrosion testing**

AES-preiskave krtačenega nerjavnega jekla AISI 304 po koroziskem preskusu

M. Torkar, D. Mandrino, M. Lamut ..... 39

**Using a FIB to prepare Al(OH)<sub>3</sub> samples for the TEM**Uporaba FIB za pripravo vzorcev Al(OH)<sub>3</sub> za TEM

I. Nikolic, V. Radmilovic, T. Z. Sholklapper, D. Blečić ..... 45



# A FAILURE CRITERION FOR SINGLE-CRYSTAL SUPERALLOYS DURING THERMOCYCLIC LOADING

## MERILO ZA PRELOM MONOKRISTALA SUPERZLITINE PRI TERMOCIKLIČNI OBREMENITVI

Leonid Getsov<sup>1</sup>, Artem Semenov<sup>1</sup>, Alexander Staroselsky<sup>2</sup>

<sup>1</sup>St. Petersburg State Polytechnical University, Russia, St. Petersburg, Polytechnicheskaja 29

<sup>2</sup>Pratt and Whitney, MS 165-16, East Hartford, CT, 06108 USA

getsov@online.ru

Prejem rokopisa – received: 2007-09-12; sprejem za objavo – accepted for publication: 2007-12-18

The accumulation of deformation affects the lifetime of a monocrystal submitted to low cyclic mechanical and thermal loading. An analytical method was developed considering the damages due to cyclic and axial plastic and creep deformation. The method was checked with test in vacuum on specimens of monocrystals with different space orientation, also specimens with stress concentrators. The distribution of stresses was FEM modelled. The fracture depends on the space orientation of the specimen and of the loading parameters. A new experimental-computational method using deformation-fracture criteria is suggested for the evaluation of the crystal life time

Keywords: single crystals, cyclic and axial loading, thermal fatigue, failure criteria

Kopičenje deformacije vpliva na trajnostno dobo kovine, ki prenaša malociklično mehansko in termično obremenitev. Razvita je bila analitična metoda, ki sešteva poškodbe zaradi cikličnih in enočasnih plastičnih deformacij in deformacij z lezenjem. Metoda je preverjena s preizkusi v vakuumu na vzorcih monokristalov z različno prostorsko orientacijo. Preizkusi so bili izvršeni tudi z vzorci z obliko, ki je povzročala lokalno koncentracijo napetosti. Porazdelitev napetosti je bila modelirana po metodi končnih elementov. Prelom je odvisen od prostorske orientacije in od parametrov obremenitve. Predlagana so nova deformacijsko-prelomna merila za oceno trajnostne dobe monokristala na podlagi eksperimentalno-računske analize.

Ključne besede: monokristali, ciklična in aksialna obremenitev, termična utrujenost, pogoji za prelom

## 1 INTRODUCTION

The deformation criterion

$$D_1(\Delta\epsilon_{pl}) + D_2(\Delta\epsilon_{ci}) + D_3(\epsilon_{pl}) + D_4(\epsilon_{ci}) = 1 \quad (1)$$

for the fracture of metal in conditions of low-cycle and thermal-cycle loading was proposed in <sup>1</sup>. The quantitative result of the lifetime test on the basis of this criterion depends on the choice of the deformation parameters.

The proposed deformation criterion is based on the summation of the damage caused by cyclic plastic deformations  $D_1 = \frac{1}{C_1} \sum_n (\Delta\epsilon_i^{pl})^k$ , cyclic creep deformations  $D_2 = \frac{1}{C_2} \sum_n (\Delta\epsilon_i^{pl})^k$ , unilaterally accumulated plastic deformations  $D_3 = \frac{1}{C_3} \sum_n \frac{\epsilon_i^{pl}}{\epsilon_r}$  and unilaterally accumulated creep deformations  $D_4 = \frac{1}{C_4} \sum_n \frac{\epsilon_i^{pl}}{\epsilon_r}$ .

In the case of interference of the above-mentioned types of damage the relevant corrections are made by considering the limiting characteristics of the material,  $C_1$ ,  $C_2$ ,  $\epsilon_r$ , and  $\epsilon_{cr}$ . This criterion was tested experimentally under conditions of uniaxial and composite tension for various samples, and the GTE details made of

isotropic heat-resistant steels and alloys that fracture are caused by low-cycle or thermal fatigue (see Figure 1 and [2–4 and others]).

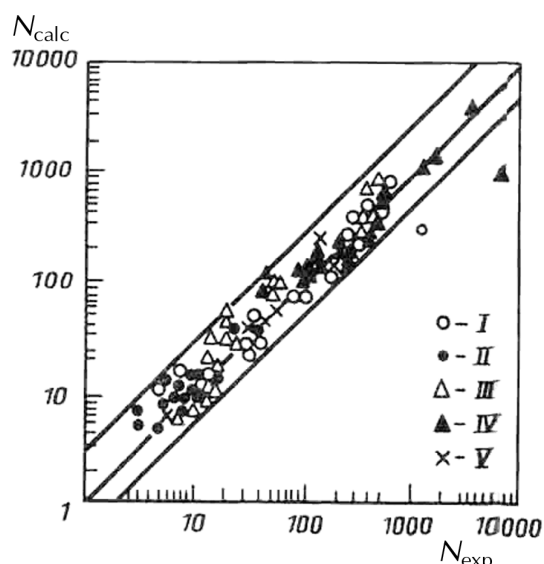


**Figure 1:** The correlation between the experimental and calculated values of the lifetime: I- $D_1+D_2$ , II- $D_3+D_4$ , III- $D_1+D_2+D_4$ , IV- $D_1+D_3+D_4$ , V- $D_1+D_2+D_3+D_4$

**Slika 1:** Korelacija med eksperimentalnimi in izračunanimi vrednostmi za trajnostno dobo I- $D_1+D_2$ , II- $D_3+D_4$ , III- $D_1+D_2+D_4$ , IV- $D_1+D_3+D_4$ , V- $D_1+D_2+D_3+D_4$

The quantitative result of the details' lifetime test on the basis of this criterion depends on the choice and precision of its deformation parameters. As for the isotropic materials, normally the role of such parameters is played by the intensities of the total amplitudes of the deformations

$$\Delta\varepsilon_i^{pl} = \sqrt{\frac{2}{9}[(\Delta\varepsilon_1^{pl} - \Delta\varepsilon_2^{pl})^2 + (\Delta\varepsilon_2^{pl} - \Delta\varepsilon_3^{pl})^2 + (\Delta\varepsilon_3^{pl} - \Delta\varepsilon_1^{pl})^2]} \quad (2a)$$

$$\Delta\varepsilon_i^c = \sqrt{\frac{2}{9}[(\Delta\varepsilon_1^c - \Delta\varepsilon_2^c)^2 + (\Delta\varepsilon_2^c - \Delta\varepsilon_3^c)^2 + (\Delta\varepsilon_3^c - \Delta\varepsilon_1^c)^2]} \quad (2b)$$

and the intensities of the accumulated deformations,

$$\varepsilon_i^{pl} = \sqrt{\frac{2}{9}[(\varepsilon_1^{pl} - \varepsilon_2^{pl})^2 + (\varepsilon_2^{pl} - \varepsilon_3^{pl})^2 + (\varepsilon_3^{pl} - \varepsilon_1^{pl})^2]} \quad (3a)$$

$$\varepsilon_i^c = \sqrt{\frac{2}{9}[(\varepsilon_1^c - \varepsilon_2^c)^2 + (\varepsilon_2^c - \varepsilon_3^c)^2 + (\varepsilon_3^c - \varepsilon_1^c)^2]} \quad (3b)$$

In this research we studied the possibility of generalizing the above-mentioned criterion for the case of single-crystal alloys. This generalization was based on the following relationships for fatigue-crack initiation and growth in the references <sup>5-12</sup>.

According to the experimental data, the increase of temperature <sup>5</sup> and the reduction in the frequency <sup>6</sup> change the mechanism of fracture in single crystals, which means that the transition from crack growth along *crystallographic* (octahedral) planes to growth in other directions does not depend on the crystal orientation, but on the conditions of loading (according to **Mode I**). The non-crystallographic growth is observed predominantly on the boundary of the  $\gamma/\gamma'$  phases.

One of the possible explanations <sup>20</sup> for such a transition is the initiation of additional damage owing to the influence of the environment. Oxygen-related brittle behavior in the vicinity of the crack tip takes place according to the diffusion mechanism, and is sensitive to the temperature, the time (frequency) and the concentration of oxygen. A comparison of the results of the experiments made in air <sup>5</sup> and in vacuum <sup>7</sup> has shown that the transition temperature is considerably higher in vacuum. When the frequency is decreased, the time of the brittle behavior within the cycle increases, which promotes the further penetration of oxygen, and this initiates the transition from the crystallographic mode of crack growth to the non-crystallographic mode I. Also, the increase in the temperature accelerates the diffusion process, promoting the transition from a crystallographic to a non-crystallographic mechanism of crack growth.

As shown in <sup>8</sup>, the threshold value for non-crystallographic fractures,  $\Delta K_{thl}$ , is lower than the value of  $\Delta K_{th(111)}$  for cracks growing along a crystallographic plane, and when  $\Delta K_{eq}$  becomes lower than  $\Delta K_{th(111)}$  the crack cannot continue growing according to the crystallographic mechanism and goes over to growth according to mode I. Thus, the experiments show that the transition from the crystallographic to the non-cry-

stallographic stage is controlled by the temperature  $T$ , the frequency  $f$ , and the total amplitude of SIF,  $\Delta K$ .

For the set of above-mentioned parameters it is possible to create maps of mechanisms for the growth of fatigue cracks (analogous to the maps for static loading in <sup>9</sup>, showing the boundaries between the crystallographic and non-crystallographic areas of crack growth). As an example of such a map, the reader is referred to the map in <sup>10</sup> (see **Figure 2**), obtained on the basis of an examination of thermally activated slip processes in the vicinity of the crack tip.

The transition from the crystallographic mode of growth at high temperatures is also promoted by the decrease in the anisotropy of the elastic and strength characteristics of crystals. So, at high temperatures ( $\approx 980$  °C) the growth rate of the fatigue cracks does not, in practice, depend <sup>11</sup> on the orientation of single crystals under the conditions of a uniaxial and composite deformation mode. This probably explains the absence of anisotropy in high-temperature multi-cycle fatigue.

It is important to note that the arborescent structure also influences the change of the orientation of the fatigue-crack growth and it could provoke the transition from one crystallographic plane to another. The equalization of the crack-growth rates for single crystals with orientations [111] and [001] can be explained <sup>11,12</sup> by the fact that as  $\Delta K$  grows, the fatigue-crack trajectory diverts from the plane (111) perpendicular to the loading axis and evolves into the plane (001), where inter-dendrite areas are concentrated, i.e., to the same plane in which the fatigue cracks grow in samples with the orientation [001].

As a two-dimensional model, interpreting simply the fatigue crack's growth in the area surrounding the cooling duct, the problem of crack growth in a plate with

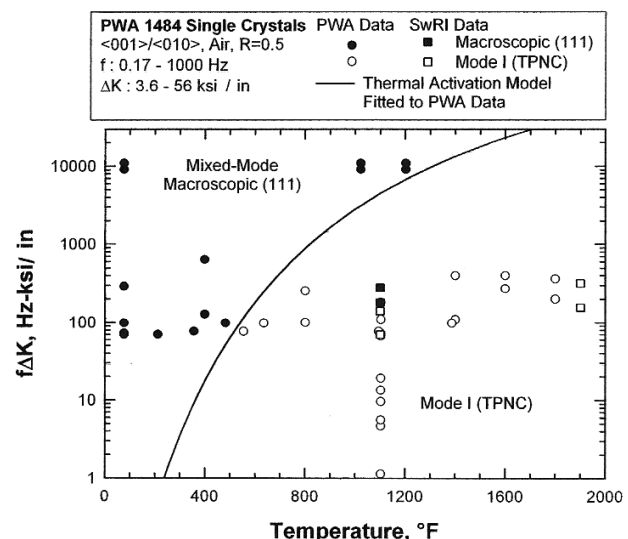


**Figure 2:** Map of fatigue-crack growth mechanisms for monocrystals <001>/<010> PWA 1484 <sup>10</sup>

**Slika 2:** Shema mehanizma rasti utrujenostne razpoke za monokristale <001>/<010> PWA 1484 <sup>10</sup>

a circular hole can be considered. The plate is in non-uniform temperature conditions with the minimum value of the temperature on the edge of the hole: the greater is the distance from the hole, the higher are the temperature and the SIF. The crack-growth process on the plane of parameters corresponding to the map of mechanisms of fatigue-crack growth in a single crystal is shown schematically in **Figure 5** with the line ABC. When the boundary between the crystallographic and non-crystallographic stages is crossed at the point B, the crack changes its growth direction. With the change in the mechanism and the direction of the crack growth, the speed of growth also changes.

Depending on the load level and the frequency, the sample orientation, the geometrical parameters of the plate with a hole and the material properties, different schemes of crack growth are possible. Among them are both the modes without a direction change (in one plane, crystallographic or non-crystallographic) and modes with one or multiple direction changes.

The extrapolation of the research results described in <sup>12</sup> for the conditions of thermal-cycle loading and, as a final goal, the development of a new fracture criterion, have become the object of the present research. At the same time, we are not discussing here the problems of the choice of models for the visco-elastic plasticity for the calculation of parameter values of criterion (1).

## 2 TEST METHODS

The thermal fatigue tests were performed for samples made of a single-crystal high-temperature alloy with five different orientations, including <001>, <011> and <111>. During the tests, the samples in sand-glass form were rigidly fixed in vacuum <sup>13</sup>.

A comprehensive procedure is developed in NPO CKTI for the definition of the thermal fatigue resistance of various materials and coatings, applying a special appliance that allows us to clamp flat the sand-glass shaped test pieces and to ensure their cyclic heating with a conducting current (**Figure 3**). The heating takes place according to a specified program (**Figure 4**), maintained automatically during the testing. The appliance is fixed in a vacuum chamber. The ultimate cycle temperature, defined by the rate of oxide-film formation on the sample surface, increases with the vacuum. The sample material's behavior at various surface points on the sample is observed using a microscope with a 250× magnification. During the test the following parameters are recorded: the characteristic properties of the deformation relief defining the mechanism of the accumulation of thermal fatigue damage; the number of cycles to the first microcrack formation in various elements of the metal and the coating; the growth rate of the incipient cracks; the number of cycles to sample failure and the accumulated deformations in the ruptured zone.

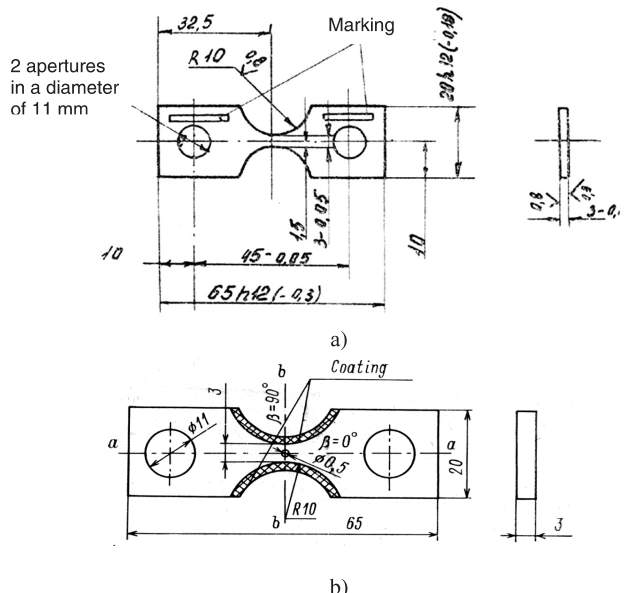


**Figure 3:** Shape of the specimen (a) and a sketch of the specimen with a coating and with a central hole (b)

**Slika 3:** Oblika preizkušanca (a) in shema preizkušancev s prekrivjem in z osrednjo izvrtino (b)

The range of the conditionally elastic stresses  $\Delta\sigma$  and the range of the total deformation  $\Delta\varepsilon$  in the specimen's working part in the cycle were calculated from thee equations:

$$\begin{aligned}\Delta\sigma &= (E_{st1} \alpha_1 T_{max} - E_{st2} \alpha_2 T_{max})\varphi \\ \Delta\sigma &= (\alpha_1 T_{max} - \alpha_2 T_{max})\varphi \\ \varphi &= 1 - \Delta k / \Delta l\end{aligned}\quad (4)$$

where  $E_{st}$  is the static elastic modulus;  $\Delta l$  is the free travel of the test points during heating from  $T_{mi}$  to  $T_{max}$ ; and  $\Delta k$  is the measured value of the displacement of the control microhardness marks, applied to the sample surface along its working-part edges during the cycle.

In this calculation the values  $\Delta k$  and  $\varphi$  were used after being averaged on the basis of the hypotheses of their linear summability.

Some 9-mm-wide plates of a single-crystal alloy with different orientations were prepared for the tests (see **Table 1**).

**Table 1:** Sample orientation

**Tabela 1:** Orientacija preizkušancev

Number of the sample series	Orientation	Deviation from the exact axial orientation in degrees	Azimuthal orientation of the crystallographic planes in degrees
1	111	5.64	8.26
2	011	4.51	11.27
3	011	8.33	14.43
4	011	9.67	7.86
5	001	5.47	41.97

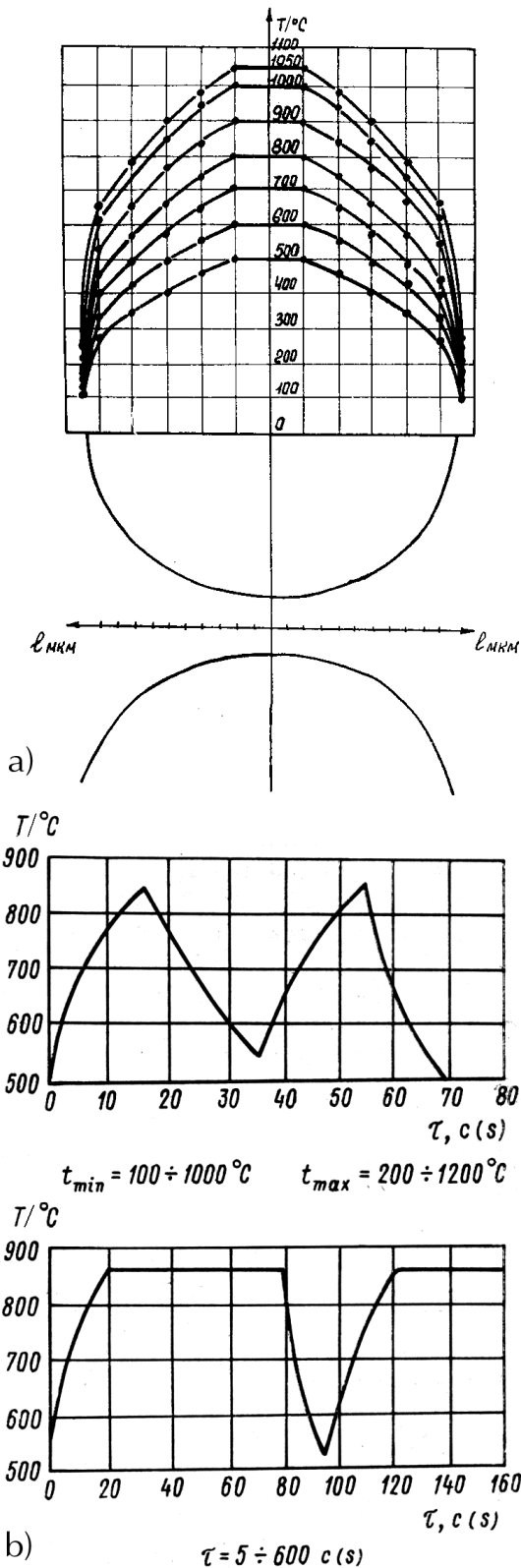
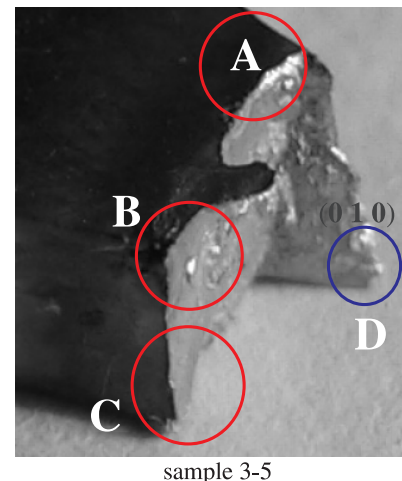
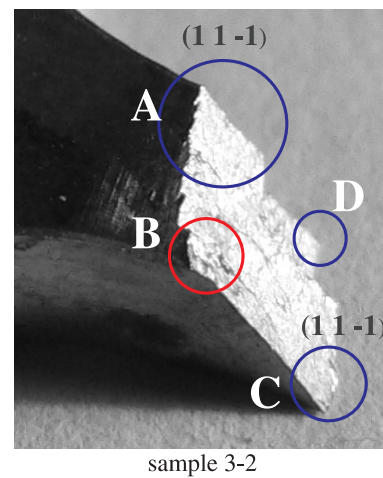


**Figure 4:** Experimentally determined distribution of the temperature along the length of the sample (a) and an example of the change of the maximum temperature in the working part of the sample during the cycle (b)

**Slika 4:** Eksperimentalno določena porazdelitev temperature po dolžini preizkušanca (a) in primer spremembe najvišje temperature v delovnem delu preizkušanca med ciklom (b)

Some tests were made on samples with stress concentrators in the form of holes with a diameter of 0.5 mm. The tests were conducted under different maximum temperatures in the cycle  $T_{\max}$  ( $850 \text{--} 1050 \text{ } ^\circ\text{C}$ ) with and without 2–5 min of holding at  $T_{\max}$ . The positions of the slip lines on the sample's surface were calculated and confirmed experimentally, as was the crack orientation up to the moment of the sample's rupture. The values of the irreversible deformations (characterizing the ratcheting) taking place in the central part of the samples were also determined.

For the interpretation of the test results we: a) analyzed the character of the fracture from the four sides of the sample (see **Figure 5**) and b) carried out finite-element calculations for the change of the sample's deformation mode in order to find the orientations of the rupture surfaces with the help of methods for deformable solid-body mechanics and to compare the results with crystallographic predictions and experimental data.



O – Crystallographic fracture, O – Non-crystallographic fracture.

**Figure 5:** Interpretation of the fracture character of the samples 3-2 and 3-5

**Slika 5:** Interpretacija značilnosti preloma preizkušancev 3-2 in 3-5

### 3 EXPERIMENTAL RESULTS AND THEIR ANALYSIS

The results of the performed experiments were compared to the results of the crystallographic analysis and the calculation of the samples' deformation mode. The stress analysis of the samples was performed with the help of the PANTOCRATOR finite-element program<sup>14</sup> (see <http://www.pantocrator.narod.ru>) based on the following assumptions:

- 1) in the tension phase, the cleavage cracks can originate and grow, and their growth direction is determined by the orientation of the platform of the maximum principal value of the stress tensor,
- 2) in the compression phase, the shear cracks can originate and grow, and their growth direction is determined by the orientation of the platforms of the maximum tangent stresses.

From now on the concept of non-crystallographic fracture mode is used in the phenomenological context, as a fracture (observed at the macro-level) not coinciding with any of the crystallographic slip planes.

As an example, let us consider the place of origin of a shear crack on the basis of the hypothesis of maximum

tangential stresses for a sample of the 3<sup>rd</sup> group tested in the mode 150–900 °C. We found that there are two equal, centrally symmetric maximums  $\tau_{\max} = 856$  MPa with a bias located at a distance of 0.64 mm from the center (see **Figure 6**), and the stresses localized in the lateral zones (with a maximum on the center line) (see **Figure 6b**).

For the same sample, we identified the tensile-crack initiation point using the hypothesis of maximum principal stresses. We found that there are two equal, centrally symmetric maximums  $\sigma_1 = 1559$  MPa at a distance of 0.45 mm from the centre (see **Figure 7**); there is also a localization of stresses in the lateral zones (with a maximum at the edge) (see **Figure 7b**).

An analysis of the calculation results showed that the distribution of stresses  $\sigma_x$  and the locations of the maximum stress zones are very different for different groups of samples.

An example of the experimental data analysis is shown in **Table 2**, containing the results for sample 2-1 tested under the mode 150–900 °C.

For this sample the crystallographic and the finite-element results are similar and show only an insignificant difference compared to the experiment (a

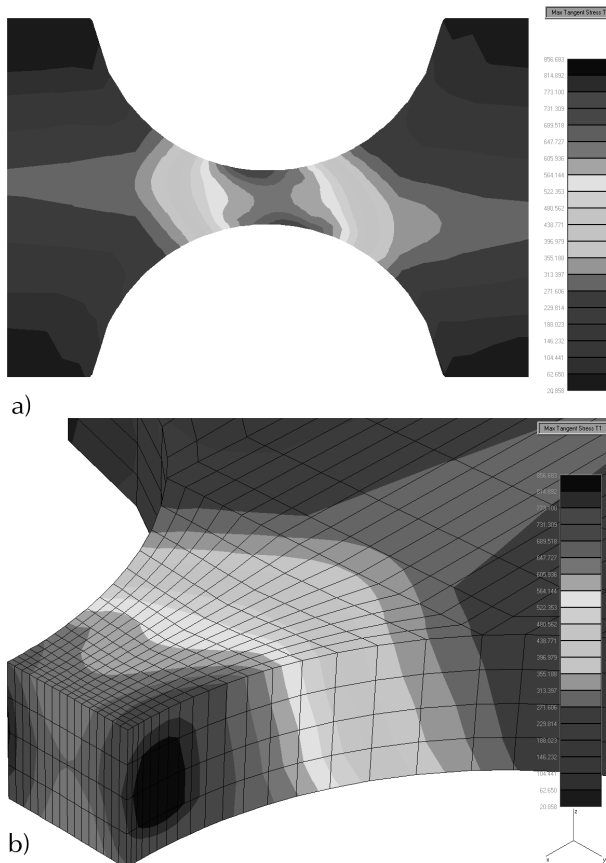


**Figure 6:** Distribution of the fields of maximum tangential stress (sample 3-0, 3<sup>rd</sup> cycle)

**Slika 6:** Porazdelitev polj največjih tangencialnih napetosti (preizkušanec 3-0, 3. cikel)

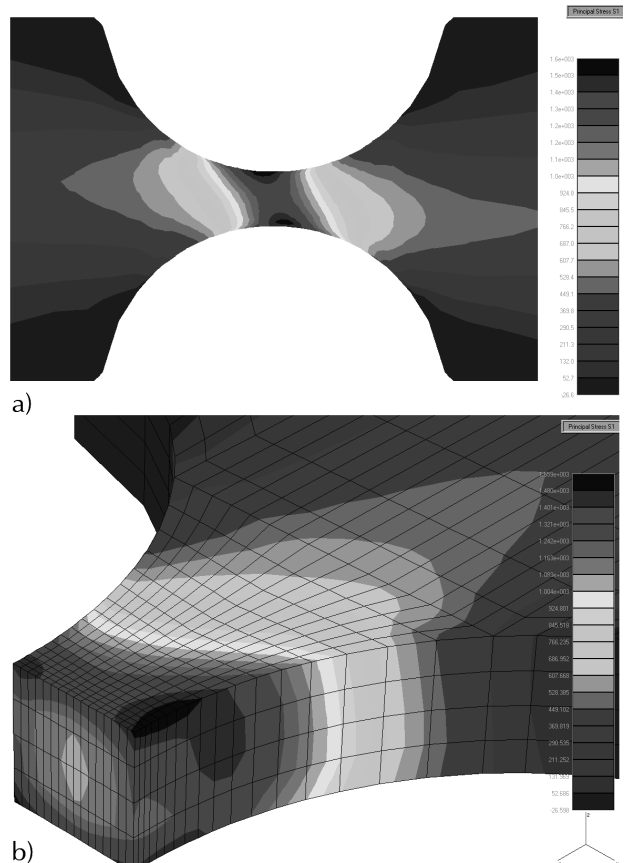


**Figure 7:** Distribution of fields of maximum principal stress (sample 3-0, 3<sup>rd</sup> cycle)

**Slika 7:** Porazdelitev polj največjih glavnih napetosti (preizkušanec 3-0, 3. cikel)

**Table 2:** Comparison of the experimental data with the results of the crystallographic and finite-element analyses of specimen 2-1

**Tabela 2:** Primerjava eksperimentalnih podatkov in rezultatov kristalografske analize in analize po metodi končnih elementov za preizkušanec 2-1

	Experiment	crystallography	FEA	
			cleavage mode	shear mode
A	84 / 49	84 / 51 (1-11)	90 / 90	88 / 45
B	90 / 47	84 / 51 (1-11)		
C	86 / 49	84 / 51 (1-11)		
D	86 / 49	84 / 51 (1-11)		

maximum of 4°). Symbolically, we designate fractures of this type as "Mode 90 / 45".

Owing to the absence of pure modes of crystallographic or non-crystallographic fracture and, in some

cases, to the ambiguities of the choice between the modes caused by the neighboring prognoses of the crystallographic and the finite-element analysis, in order to map the fracture mechanisms we use the classification of modes on the basis of the orientation of the middle fracture "plane" instead of the concepts of crystallographic or non-crystallographic fracture modes the four modes are considered:

- Mode 90 / 45      }
- Mode 90 / 90      } crystallographic or SSS
- Mode 45 / 45      }
- Mode 45 / 90      } crystallographic

In **Table 3** the results of the analyses of the fracture modes for the samples from group 3 are shown. The results show that the sample's rupture occurred in the

**Table 3:** Dominant fracture modes of the samples of the 3<sup>rd</sup> group ( $\tau$ -duration of cycle)**Tabela 3:** Prevladajoči načini preloma preizkušanca iz 3. skupine ( $\tau$ -trajanje cikla)

Sam ple	$T_{\min}/^{\circ}\text{C}$	$T_{\max}/^{\circ}\text{C}$	$\tau/\text{s}$	N	$\Delta\varepsilon/\%$	Isometric view	Front view	Side view	Mode
3-0	150	900	80	951	0.77				90/90 (Non-Crystal)
3-1	200	950	60	450	0.88				90/45 (Crystal)
3-2	250	1000	64	63	0.68				90/45 (Crystal)
3-3	500	1000	25	1220	0.68				90/45 (Crystal)
3-4	550	1050	23	356	0.41				90/45 (Crystal)
3-5	450	950	20	2535	0.49				90/90 (Non-Crystal)
3-0	150	900	80	951	0.77				90/90 (Non-Crystal)
3-1	200	950	60	450	0.88				90/45 (Crystal)

Non-FE, non-forecasting with the finite-element analysis

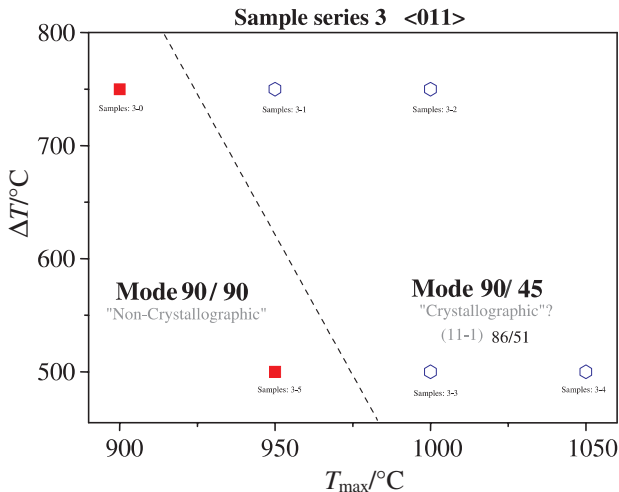


**Figure 8:** Map of the fracture mechanisms for the samples of the 3<sup>rd</sup> series

**Slika 8:** Shema mehanizma za preloma za preizkušanje iz 3. serije

crystallographic, the non-crystallographic and the mixed modes. The conditions for the occurrence of the crack type (dominant type (mode) of fracture) are generalized with the help of maps of fracture mechanisms plotted in

the coordinates  $T_{\text{MAX}} - \Delta T$  (see, for example, **Figure 8**). With the help of such maps of fracture mechanisms it is possible to separate the loading conditions.

**Fracture criterion.** The above-mentioned facts make it evident that, depending on the fracture mode of single-crystal alloys, in each concrete case it is necessary to choose the corresponding deformation-fracture criteria:

- criterion 1:

$$D_1(\Delta\gamma_{\text{pl}}) + D_2(\Delta\gamma_c) + D_3(\gamma_{\text{pl}}) + D_4(\gamma_c) = 1 \quad (4)$$

- criterion 2

$$D_1(\Delta\varepsilon_{\text{pl1}}) + D_2(\Delta\varepsilon_{\text{cl}}) + D_3(\varepsilon_{\text{pl1}}) + D_4(\varepsilon_{\text{cl}}) = 1 \quad (5)$$

Namely, for crystallographically oriented fracture modes, the following criterion parameters must be chosen: shear deformations and their total amplitudes  $\gamma_{\text{pl}}$  and  $\Delta\gamma_{\text{pl}}$  ( $\gamma_c$ ,  $\Delta\gamma_c$ ), and for non-crystallographic fracture modes, the tensile deformations and their total amplitudes  $\varepsilon_{\text{pl1}}$ ,  $\Delta\varepsilon_{\text{pl1}}$ ,  $\varepsilon_{\text{cl}}$ , and  $\Delta\varepsilon_{\text{cl}}$ .

Let us take as a basis the fact that the performed thermal fatigue tests are described, on the one hand, by the total number of cycles and, on the other hand, by the level of the ratcheting deformation.

**Table 4:** Comparison of the ratcheting deformation  $\varepsilon_{\text{max}}$  with the thermal fatigue and plasticity (short-time plasticity  $\varepsilon_r$  and creep-rupture plasticity  $\varepsilon_{\text{cr}}$ ) at high temperature

**Tabela 4:** Primerjava prelomnih deformacij  $\varepsilon_{\text{max}}$  s termično utrujenostjo in plastičnostjo (kratkotrajna plastičnost  $\varepsilon_r$  in plastičnost pri prelomu z lezenjem  $\varepsilon_{\text{cr}}$ ) pri visoki temperaturi

Orientation	$T_{\text{max}}/^\circ\text{C}$	Time of stay, min	$\varepsilon_{\text{max}}/\%$	$\varepsilon_{\text{max1}}/\varepsilon_{\text{max2}}$	$N$	$N_2/N_1$	$\varepsilon_r$ % at $T_{\text{max}}$	$\varepsilon_{\text{cr}}$ % at $T_{\text{max}}$	$D_3$	$D_4$
001	900	0	9.0	0.75	560	0.17	27	12.8–16.4	0.1	0
	1000	0	12		95		19	8–23	0.25	0
111	900	0	10.7 24.3*		823 50		19,5	14–24	0.22 0.5	0
		2	21		140				0	0.35–0.6
		5	18.3		16				0	0.3–0.52
	1000	2	23.7		194		21,5	7.2–23.8	0	0.4–1.3
011(2)	850	0	9.3*		2952					
	900	0	15.3		100					
	1000	0	20	0.67	472	0.67				
		5	29.7		317					
		0	10.6*	0.77	187	0.33				
		2	13.7*		62					
011(3)	900	0	10.3		951					
	950	0	4.3	0.4	2535	0.18				
	950	0	10.7		450					
	1000	0	7.3	0.6	1220	0.05				
	1000	0	12		63					
	1050	0	14.7		356					
011(4)	900	0	10	0.47 0.55	308	0.06 0.08				
	900	2	21.3		17					
	900	5	18		26					
	900	0	9.7*		25					
	950	0	9.7	0.94	626	0.20				
	950	2	10.3		128					

\*-specimen with concentrator

**Table 5:** Calculation of damage by means of (5)**Tabela 5:** Izračun poškodb z uporabo (5)

Orientation	The minimum temperature of a cycle, °C	The maximum temperature of a cycle, °C	Time of cycle, sec	Number of cycles before formation of the main crack, $N_m$	$\Delta\epsilon$ %	$2\sigma_{-1}/E$	$\Delta\epsilon_{el}$ %	$\Delta\epsilon_{pl,c}$ %	$D_1$	$D_2$	$D_3$	$D_4$	$\Sigma D_i$
[111]	150	900	72	190	0.73	$860/2.4 \cdot 10^5$	0.36	0.37	0.273	0	0.22	0	0.59
			247	50	0.69	$860/2.4 \cdot 10^5$	0.36	0.33	0	0.34	0	0.35	1.27
			378	12	0.73	$860/2.4 \cdot 10^5$	0.36	0.37	0	0.09	0	0.52	0.61
	500	1000	149	80	0.64	$648/2.3 \cdot 10^5$	0.28	0.36	0	0.60	0	0.40	1.00
[001]	150	900	72	500	0.86	$700/0.998 \cdot 10^5$	0.70	0.16	0.013	0	0.10	0	0.11
	250	1000	48	40	0.855	$500/0.95 \cdot 10^5$	0.52	0.33	0.18	0	0.25	0	0.43
	500	1000	28	1400	0.655	$500/0.95 \cdot 10^5$	0.52	0.13	1.13	0	0.25	0	1.38

The data in **Table 4** show that a) a decrease of the ratcheting deformation results in a sample lifetime increase, b) the number of cycles to fracture in tests with holding at  $T_{MAX}$  is considerably lower than the numbers of cycles in the case of tests without such holding. The research of Sizova R.N.<sup>15</sup> has shown that, in conditions of compression, the time to fracture is 2.5–3.0 times longer than in the case of tension. Using the deformation criterion of destruction, it is equivalent to the updating of the ratio  $D_3 = \epsilon_{max}/\epsilon_r$  and  $D_4 = \epsilon_{max}/\epsilon_{cr}$ , with the help of the correction factor 0.4. We then have:

$$D_3 = 0.4 \frac{\epsilon_{max}}{\epsilon_r} \quad (6)$$

$$D_4 = 0.4 \frac{\epsilon_{max}}{\epsilon_{cr}} \quad (7)$$

where  $\epsilon_r$  and  $\epsilon_{cr}$  are the corresponding deformations in the case of short-time fracture and fracture in the creep test at  $T_{MAX}$  under tension.

Let us compare the deformations  $\epsilon_{max}$  for two tests,  $\epsilon_{max1}$  and  $\epsilon_{max2}$ . We can see that the relation  $(\epsilon_{max1}/\epsilon_{max2}) - N_2/N_1$  varies from 0.12 up to 1.00. This means that the ratcheting deformation value cannot characterize the fracture conditions and only helps to identify the trend.

Here are  $\epsilon_{max} = \max(\epsilon_1, \epsilon_2)$ , where  $\epsilon_1$  and  $\epsilon_2$  are the deformations measured in two directions of the sample's cross-section.

To apply the proposed deformation criterion (1) to the results of the performed tests it is necessary: a) to calculate appropriately (using creep parameters and deformation curves in conditions of short-time tension) the width of the hysteresis curve, with reference to the known temperature-change graph, b) to have the values of the short-time and long-time plasticity at  $T_{MAX}$ . A comparison of the single-crystal alloy plasticity values  $\epsilon_r$

obtained during the simple tension tests and the  $\epsilon_r$  in long-term tests prove that, like for polycrystalline materials, in creep conditions the plasticity of the material is less than the short-time plasticity.

Having the experimental values of ratcheting deformations and supposing that the exponents in the expressions for  $D_1$  and  $D_2$  are equal to 2.0 and 1.25 (like in the case of polycrystalline materials), the calculation of the number of cycles until fracture turns out to be dependent on the two material parameters and the maximum temperature in the cycle. As a first approximation, these material parameters can be evaluated from the values  $\epsilon_r$  and  $\epsilon_{cr}$  ( $C_1 = (0.5\epsilon_r)^2$ ,  $C_2 = (0.75\epsilon_{cr})^{1.25}$ ).

Let us consider some results of the calculation of the interruption mechanism damage. The calculation of the damage  $D_1$  and  $D_2$  (see **Table 5**) was carried out with reference to the number of cycles before the occurrence of the main crack,  $N_m$ . The size of the range of the non-elastic deformation  $\Delta\epsilon_{pl}$  and  $\Delta\epsilon_c$  was determined as the difference of the range of full deformations,  $\Delta\epsilon$ , and the sizes  $2\sigma_{-1}/E$ . Thus, it was accepted that the cyclic limit of the elasticity is equal to the fatigue strength at the maximum temperature of the cycle. For the calculation the  $D_1$  and  $D_2$  values of plasticity were accepted under a simple tension ( $\epsilon_r$ ) and at the long rupture time ( $\epsilon_{cr}$ ) given in **Table 6**. The values of the damage  $D_3$  and  $D_4$  are calculated by means of Equations (6) and (7) and the experimentally obtained values of ratcheting and plasticity during compression. The data in Table 5 confirm the satisfactory description of the conditions of the origin of the main cracks found during thermocyclic loading of a single-crystal alloy.

**Table 6:** Input data**Tabela 6:** Vhodni podatki

Temperature/ °C	Elongation ( $\epsilon_r$ )/%		Long time elongation ( $\epsilon_{cr}$ )/%		Fatigue limit $\sigma_{-1}$ /MPa		
	[001]	[111]	[001]	[111]	[001]	[011] approximately	[111]
900	27	19.5	8.6–16.4	14.1–24	350	360	430
1000	19	21.5	8–23	7.2–23.8	–	–	–
1100	22	21.5	–	–	170	170	170

**Table 7:** Relations between the shear strain  $\gamma_{nl}$  and the axial strain  $\varepsilon_x$   
**Tabela 7:** Razmerje med strižno deformacijo  $\gamma_{nl}$  in axialno deformacijo  $\varepsilon_x$

Specimen series	Specimen orientation	$\gamma_{nl}/\varepsilon_x$
1.	[111]	4.25
2.	[011]	4.50
3.	[011]	4.09
4.	[011]	2.80
5.	[001]	2.16

**Shear-strain computation.** The criterion (4) requires a shear-strain ( $\Delta\gamma_{pl}$ ,  $\Delta\gamma_c$ ,  $\gamma_{pl}$ , and  $\gamma_c$ ) computation. The shear strain  $\gamma_{nl}$  at the plane with the normal vector  $\mathbf{n}$  in the slip direction  $\mathbf{l}$  is defined on the basis of the strain tensor  $\boldsymbol{\varepsilon}$  by the relation

$$\gamma_{nl} = 2\varepsilon_{nl} = 2\mathbf{n} \cdot \boldsymbol{\varepsilon} \cdot \mathbf{l} \quad (8)$$

or, by using a presentation with components

$$\gamma_{nl} = 2\varepsilon_{nl} = 2(n_x \varepsilon_{xx} l_x + n_x \varepsilon_{xy} l_y + n_x \varepsilon_{xz} l_z + n_y \varepsilon_{xy} l_x + n_y \varepsilon_{yy} l_y + n_y \varepsilon_{yz} l_z + n_z \varepsilon_{xz} l_x + n_z \varepsilon_{yz} l_y + n_z \varepsilon_{zz} l_z) \quad (9)$$

The presented equations are valid for all cases,  $\Delta\gamma_{pl}$ ,  $\Delta\gamma_c$ ,  $\gamma_{pl}$  and  $\gamma_c$ , with a special choice of the strain tensor for each case.

The components of the normal vector  $\mathbf{n}$  and the slip direction  $\mathbf{l}$  in the global coordinate system are related to the components in the crystallographic coordinate system by the following relations

$$\begin{aligned} n_x &= A_{11} n_{<100>} + A_{21} n_{<010>} + A_{31} n_{<001>} \\ n_y &= A_{12} n_{<100>} + A_{22} n_{<010>} + A_{32} n_{<001>} \\ n_z &= A_{13} n_{<100>} + A_{23} n_{<010>} + A_{33} n_{<001>} \end{aligned} \quad (10)$$

and

$$\begin{aligned} l_x &= A_{11} l_{<100>} + A_{21} l_{<010>} + A_{31} l_{<001>} \\ l_y &= A_{12} l_{<100>} + A_{22} l_{<010>} + A_{32} l_{<001>} \\ l_z &= A_{13} l_{<100>} + A_{23} l_{<010>} + A_{33} l_{<001>} \end{aligned} \quad (11)$$

where  $A_{ij}$  is the matrix of crystallographic orientations, which is different for each specimen.

The results of the computations of  $\gamma_{nl}$  for all the specimen series are given in **Table 7**. The diagonal

components of the strain tensor are obtained from the experimental data and the non-diagonal components are taken from the finite-element simulations.

The results of the calculation of damage with the use of criterion (4) are shown in **Table 8**.

For the definition of the damage size the following relations were used:

$$\begin{aligned} D_1 &= \frac{1}{C_3} \sum_n (\Delta\gamma_i^{pl})^k; D_2 = \frac{1}{C_4} \sum_n (\Delta\gamma_i^{pl})^k; \\ D_3 &= 0.4\gamma_{max}/\gamma_r; D_4 = 0.4\gamma_{max}/\gamma_{cr} \end{aligned} \quad (12)$$

where the values of the constants  $C_3$ ,  $C_4$ ,  $\gamma_r$ , and  $\gamma_{cr}$  were defined using the ratio

$$C_3 = 2.25 C_1; C_4 = 1.66 C_2; \gamma_r = 1.5 \varepsilon_r; \gamma_{cr} = 1.5 \varepsilon_r \quad (13)$$

For the orientation [111], the sum of the damage agrees with the criterion (4) at the moment of formation of the main crack, and appears to be much more than 1.0, while calculations that use this criterion (5) are in good agreement with the experiment. Thus, criterion (4) gives, in this case, an underestimated number of cycles. At the same time the use of this criterion for two samples with the orientation [001] gives the best agreement with the experiment in comparison to criterion (5), and for one specimen the agreement is worse.

The use of diagrams of maps of destruction (see **Figure 8**) allows us to predict the criterion of destruction during the thermal cyclic loading of objects made from single-crystal alloys.

The use of the forgoing modification of the deformation fracture criterion will make it possible to solve reliably the problems of the prediction of the conditions of initiation of the thermal-fatigue cracks in the turbine blades made of single-crystal alloys.

## 4 CONCLUSIONS

The performed experimental investigation and the analysis led to the following conclusions:

1. The character of fracture of single-crystal alloys under thermal-cycle loading depends on the crystallographic orientation of the material and on the

**Table 8:** Calculation of damages by means of (4)

**Tabela 8:** Izračun poškodb z uporabo (4)

Oriental-	The minimum temperature of a cycle, °C	The maximum temperature of a cycle, °C	Time of cycle, s	Number of cycles before formation of the main crack, $N_m$	$\Delta\gamma_{pl,c}$ %	$D_1(\Delta\gamma_{pl})$	$D_2(\Delta\gamma_c)$	$D_3(\gamma_{pl})$	$D_4(\gamma_c)$	$\Sigma D_i$
[111]	150	900	72	190	1.57	2.19	0	0.62	0	2.81
			247	50	1.40	0	3.6	0	0.99	4.59
			378	12	1.57	0	0.16	0	1.47	1.63
	500	1000	149	80	1.53	0	11.7	0	1.13	12.83
[001]	150	900	72	500	0.345	0.027	0	0.144	0	0.171
	250	1000	48	40	0.71	0.37	0	0.36	0	0.73
	500	1000	28	1400	0.28	2.34	0	0.36	0	2.70

- temperature and time parameters of the loading mode.
2. The difference of the fracture mechanisms for each case of crystallographic orientation of the material can be represented with the help of the proposed fracture maps using the coordinates  $T_{\text{MAX}} - \Delta T$ .
  3. New definitions for the deformation fracture criteria of single-crystal alloys in conditions of thermal-cycle loading have been proposed; they make it possible to evaluate the lifetime of blades made of single-crystal alloys using a computational-experimental approach.
- In summary, the use of the deformation criterion for the calculation of fracture conditions for single-crystal alloys submitted to thermal-cycle loading requires, on the one hand, a knowledge of the creep and plasticity characteristics of the material for different crystallographic orientations in the working temperature range, and, on the other hand, the appropriate choice of the thermo-visco-elasto-plasticity model.

## 5 REFERENCES

- <sup>1</sup>L. B. Getsov: Problems of creation of the "universal" theory of destruction of materials. Journal of machinery manufacture under reliability problem. (2001) 5, 49–55
- <sup>2</sup>K. M. Kononov, L. B. Getsov: Failure criteria of materials under cyclic loading. Strength of materials, N2, 1984
- <sup>3</sup>P. A. Pavlov, L. B. Getsov: Deformation criteria for material rupture estimation in complex stress-strain conditions under cyclic loadings. Strength of materials, N3, 1989
- <sup>4</sup>L. B. Getsov, A. A. Nigin, M. G. Kabelevskiy: Use of finite-element method for numerical evaluation of thermal cycling endurance of disks. Strength of materials, N4, 1979, 17
- <sup>5</sup>Cunningham S. E., DeLuca D. P., Haake F. K.: Crack growth and life prediction in single crystal nickel Superalloys. Vol. I, WL-TR-94-4089, 1994
- <sup>6</sup>Leverant G. A., Gell M.: The influence of temperature and cyclic frequency on the fatigue fracture of cube oriented nickel-base superalloy single crystal. Metall. Trans. A. 6 (1975), 367–371
- <sup>7</sup>Telesman J., Ghosh L. J.: Fatigue Crack Growth Behavior of a PWA 1484 Single Crystal Superalloy at Elevated Temperatures. ASME Paper 95-GT-452, 1995
- <sup>8</sup>Chan K. S., Feiger J., Lee Y.-D., John R., Hudak S. J.: Fatigue Crack Growth Thresholds of Deflected Mixed-Mode Cracks in PWA1484; Journal of Engineering Materials and Technology.127 (2005), 2–7
- <sup>9</sup>Frost H. J., Ashby M. F.: Deformation- mechanism maps. 1982
- <sup>10</sup>Report P&W. Dayton, 2005
- <sup>11</sup>Shalin R. E., Svetlov I. L., Kachanov E. B. et al. Single crystals of nickel base superalloys. Machinery, 1997, 333
- <sup>12</sup>Dulnev R. A., Svetlov I. L., Bychkov N. G. et al. Orientation dependence of thermal fatigue of nickel alloy single crystal; Strength problems (1988) 11, 3–9. (In Russian)
- <sup>13</sup>A. I. Rybnikov, L. B. Getsov: New technique and results of thermal fatigue tests of superalloys and coatings; Proceedings of the sixth International congress on thermal stresses. Vienna, Austria, (2005) 1, 305–309
- <sup>14</sup>Semenov A. S. PANTOCRATOR – Finite-element program specialized on the solution of non-linear problems of solid body mechanics; Proc. V-th Int. Conf. "Scientific and engineering problems of predicting the reliability and service life of structures and methods of their solution", St-Petersburg, 2003, 466-480
- <sup>15</sup>Thermal strength of machine details. The theory. Experimental researches. Calculation. Editor Birger I. A. and Shorr B. F. Mechanical engineering, 1975 (In Russian)

## ACCELERATED CREEP TESTING OF NEW CREEP RESISTING WELD METALS

### PREIZKUSI POSPEŠENEGA LEZENJA ZVAROV NOVEGA JEKLA, ODPORNEGA PROTI LEZENJU

Stan T. Mandziej,<sup>1</sup> Anna Výrostková,<sup>2</sup> Mojca Šolar<sup>3</sup>

<sup>1</sup>Advanced Materials Analysis, P.O.Box 3751, 7500 DT Enschede, Nederland

<sup>2</sup>Institute of Materials Research SAS, Watsonova 47, 043 53 Košice, Slovakia

<sup>3</sup>Elektrode Jesenice, Cesta Železarjev 8, 4270 Jesenice, Slovenia

100422.3355@compuserve.com

Prejem rokopisa – received: 2007-09-04; sprejem za objavo – accepted for publication: 2007-10-11

New creep-resisting weld metals of P91 grade were manufactured by MMA process producing multi-bead multi-layer test coupons, from which specimens were taken for accelerated creep testing on Gleeble physical simulator. The recently developed accelerated creep testing (ACT) procedure on Gleeble allows transforming in a relatively short time (less than 100 hours) the microstructure of creep-resisting materials near to the thermodynamic equilibrium state, resembling that of multi-years application at creep condition. Such advanced transformation of microstructure in the investigated weld metals after ACT was confirmed with microscopy and microanalytical study. The results also appeared to be in agreement with Thermocalc calculations. Using optimum combination of chemical compositions of the electrodes with welding procedure and post-weld heat-treatment, advantageous mechanical properties were achieved as well as results of ACT indicating potentially long creep life in exploitation conditions. In discussion of the ACT results, comparisons with results of conventional creep testing have been made. The ACT procedure appears to be useful in fast screening of newly developed creep resisting materials.

Keywords: P91 welds, accelerated creep tests, microstructure, Gleeble

Večvarkovni zvari jekla P91, odporni proti lezenju so bili pripravljeni po MMA-postopku in iz njih so bili izdelani večvarkovni vzorci za preizkuse na simulatorju Gleeble. Pred kratkim razvit preizkus pospešenega lezenja (ACT) na napravi Gleeble omogoča, da se pretvorji v relativno kratkem času (manj od 100 h) mikrostruktura jekla, odpornega proti lezenju, v stanje blizu termodinamičnega ravnotežja, ki je podobno kot po mnogih letih obremenitve z lezenjem. Tako pretvorbo mikrostrukture po ACT smo potrdili z mikroskopsko in mikroanalitsko preiskavo. Zdi se, da so rezultati v skladu z izračuni na podlagi podatkov Themocalc. Z uporabo optimalne kombinacije kemične sestave elektrod, postopka varjenja in toplotne obdelavo po varjenju so bile dosežene dobre mehanske lastnosti in rezultati ACT, ki nakazujejo na potencialno dolgotrajno stabilnost pri obremenitvi z lezenjem. V razpravi primerjamo rezultate ACT z rezultati konvencionalnih preizkusov lezenja. Videti je, da je ACT-postopek koristen za hitro oceno na novo razvitih jekel, ki so odporna proti lezenju.

Ključne besede: zvari P91, poskusi pospešenega lezenja, mikrostruktura, simulator Gleeble

## 1 INTRODUCTION

Design of the power plant components and estimation of power plants lifetime are based on long-term creep data, which are generally available for the manufactured plate and pipe materials but seldom available for the welds on the components of the power plants. This last is mainly due to the large variety of factors appearing in the fabrication procedure, which affect the creep strength and creep life of the welds. To predict the exploitation behaviour of the welds under creep, especially of the repair welds, accelerated creep testing (ACT) procedures can be used. Such procedures of accelerated tests often apply small strains and/or constant slow deformation rates to speed-up transformation of microstructure towards that of metal alloys exploited for many years at creep conditions <sup>6</sup>. In general, they aim to determine in a relatively short time the remaining strength or ductility which the creep resisting materials would have after long exposure to stresses at the elevated temperatures characteristic of their exploitation.

An accelerated creep test recently developed by the Advanced Materials Analysis, Enschede, Netherlands, in collaboration with Dynamic Systems Inc, Poestenkill NY, USA <sup>4</sup>, is a low-cycle thermal-mechanical fatigue procedure executed on Gleeble physical simulator, based on the actual knowledge of the micro- and sub-structural changes causing decay of properties during the creep. To simulate the situation of the material during creep, the following demands had to be achieved in the ACT:

- Total deformation at fracture being like at real creep – just a few percent only.
- Depletion of material's matrix in alloying elements similar to that of long-term crept steels and the carbide phases at onset of cracks being not different.
- Basic temperature and applied strains in the ACT preventing odd transformations like dissolution of carbides and/or formation of far from equilibrium phases.

These aims have been reached by considering that certain dislocations can effectively dissolve and then transport interstitial elements like C and N, and that the

annihilation of these dislocations may control the precipitation of carbides<sup>3</sup>. Thus accumulation of strains, generating appropriate dislocation configurations and increasing level of stored energy in the steel, was used to speed-up the transformation of microstructure. An additional factor used in the development of the ACT, known for a long time as capable of accelerating recrystallization of matrix and coagulation of carbides<sup>1</sup>, is an electric resistance heating with controlled thermal gradients.

An initial version of this ACT procedure<sup>4</sup> was implemented in the "SmartWeld" EU R&D project and on purpose modified in the course of it<sup>5</sup>. What follows in this article is the presentation of selected ACT results and their comparison with the conventional creep-rupture tests. Further, the reliability of the ACT is confirmed by the microstructure evolution i.e. the precipitation processes and sequence of changes leading to failure, that reproduce the situations occurring in real creep. Presented here are data obtained for P91 type weld metals, manufactured in the company Elektrode Jesenice from Slovenia.

## 2 THE ACCELERATED CREEP TEST ON GLEEBLE – ACT

To carry out the simulative accelerated creep tests, Gleeble 3500 physical simulator was used. In this simulator in a rod-like sample made of the electrically-conductive alloy the balance between electric resistance heating of the sample and the heat flow by thermal conductivity from this sample towards the cold copper jaws allows forming a uniformly heated zone in the middle-span of the sample (see **Figure 1**). To define this zone better, on samples for the ACT a gauge portion of reduced diameter was made. Samples for the ACT were taken across multi-bead, multi-layer P91 MMA welded joints, as shown in **Figure 2**. The samples were in as-welded (marked 5s and 10s) and in post-weld heat-treated condition (marked 6s and 8s). Their chemical compositions are given in **Table 1**.

Most of the ACT samples were tested till fracture occurred, however some of them especially those for fine fractographic observations and microanalytical investigations were stopped before fracturing. As the tests for different materials were run at different temperatures, the need occurred to compare the ACT results obtained at various temperatures, to the duration

of the test and its temperature had to be included in the following parameter:

$$P_{ACT} = (7 + \lg t) \cdot T/100$$

where:  $t$  = time of test in ks, and  $T$  = temperature in K.

Then, the creep strength factor in ACT has been calculated as

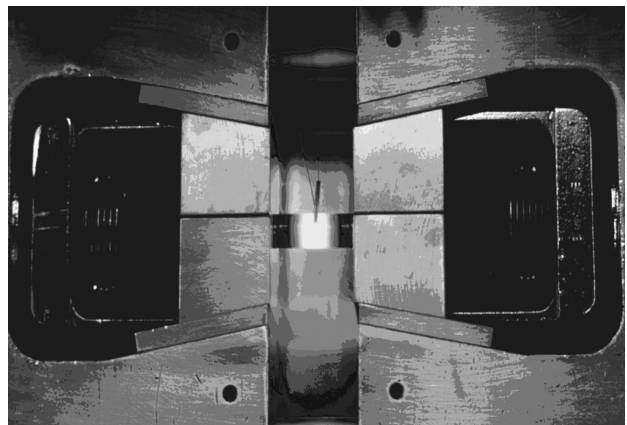
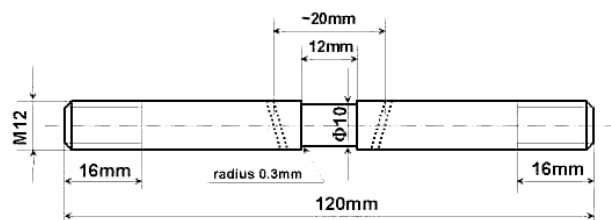
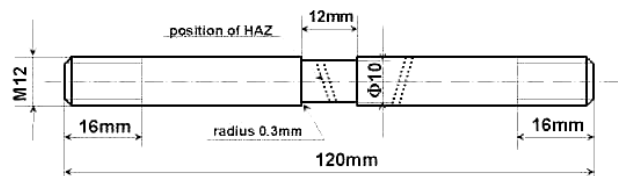


**Figure 1:** Example of a uniformly heated zone formed in Gleeble at the mid-span of the rod-like specimen (at temperature much higher than used in the ACT)

**Slika 1:** Primer enakomerno ogrete cone na napravi Gleeble na polovici dolžine paličastega preizkušanca (pri temperaturi, ki je mnogo nad tisto, uporabljeno pri preizkusih Gleeble)



**ACT sample for testing of all weld metal**



**ACT sample for testing of weld's HAZ**

**Figure 2:** Cross-weld samples used for ACT on all-weld-metal and on weld's HAZ in the "SmartWeld" EU project

**Slika 2:** Preizkušanci z zvarom uporabljeni pri ACT, ki obsegajo cel zvar in toplotno cono pri projektu EU "SmartWeld"

**Table 1:** Chemical compositions of P91 weld metals

**Tabela 1:** Kemična sestava zvarov P91

Material	Element, w/%										
	C	Mn	Si	Cr	Ni	Mo	Nb	V	Ti	W	N
5s & 8s	0.06	0.59	0.36	9.49	0.94	0.98	0.005	0.21	0.000	0.21	
6s	0.06	0.60	0.37	9.12	0.90	0.97	0.005	0.20	0.000	0.20	
10s	0.09	0.84	0.40	8.70	0.40	0.93	0.061	0.21	0.008	0.01	+

$$F_{ACT} = P_{ACT} \cdot R_S / 100$$

where  $R_S$  is the average stress of all ACT cycles measured during relaxation on tension.

Selected examples of strain-time and stress-time graphs from ACT are in **Figures 3 to 6**; in the "soft", e.g. over-tempered material like sample 6s, the zero-stress line on the strain-time curve resembles well a normal creep graph with its three characteristic stages, see **Figure 3**, while for the "hard" materials like as-welded sample 5s and 10s, a straight continuous elongation in each cycle was observed from beginning till the end of test, **Figure 5**.

Selected examples of the ACT results on P91 weld metals are given in **Table 2** below. They show in general higher creep strength of non heat-treated weld metals, with tendency of increasing time to fracture by PWHT due to changing of failure micromechanism (compare 5s with 6s). They also show positive results of optimizing heat treatment (6s vs. 8s) as well as of the improved chemical composition (5s vs. 10s).

**Table 2:** Examples of ACT results

**Tabela 2:** Primeri ACT-rezultatov

Sample number	Material & state	ACT temp. °C	ACT time to fracture ks	Tensile relax stress $R_S$ /MPa	Creep strength factor $F_{ACT}$ /MPa
5s	P91-AW	600	28.3	325	240
6s	P91-HT	620	45.2	177	137
8s	P91-HT	600	26.3	318	233
10s	P91-AW	600	82.6	336	262

In parallel, short-term creep-rupture tests (STCT) were run on these materials and the results of both tests compared. Selected results of the STCT are given in Table 3 and compared with those of the ACT. The creep strength factor –  $F_{CS}$  – given in this table was calculated from the STCT results like:

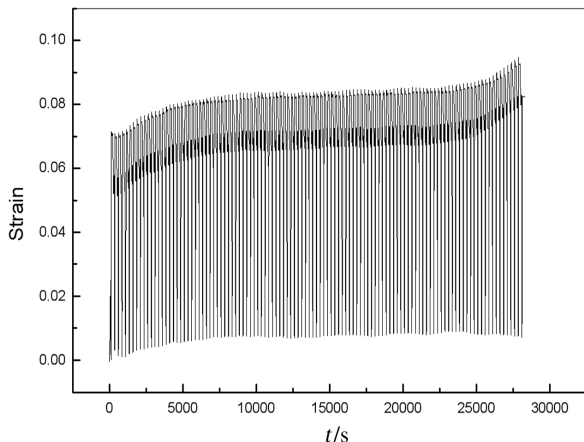


**Figure 3:** Typical strain-time graph from ACT on a "soft" weld metal – sample 6s

**Slika 3:** Značilna odvisnost deformacija-čas za ACT mehkega materiala zvara – vzorec 6s

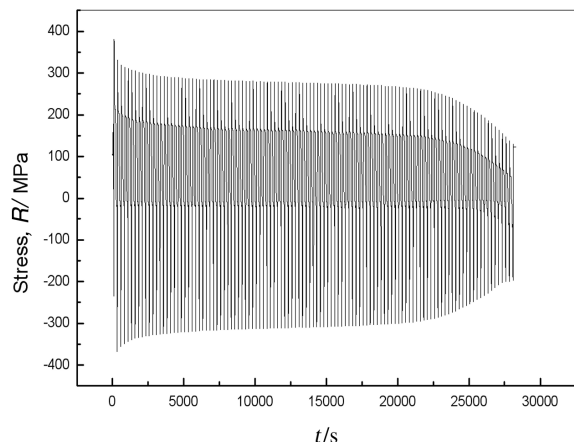


**Figure 4:** Typical stress-time graph from ACT on a "soft" weld metal – sample 6s

**Slika 4:** Značilna odvisnost napetost-čas za ACT mehkega materiala zvara – vzorec 6s

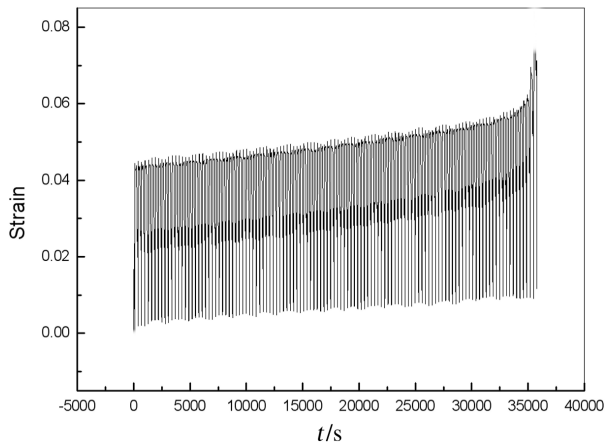


**Figure 5:** Typical strain-time graph from ACT on a "hard" weld metal – sample 5s

**Slika 5:** Značilna odvisnost deformacija-čas za ACT trdega materiala zvara – vzorec 5s

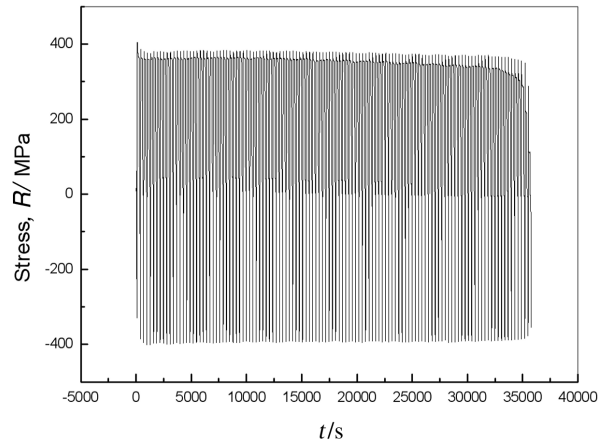


**Figure 6:** Typical stress-time graph from ACT on a "hard" weld metal – sample 5s

**Slika 6:** Značilna odvisnost napetost-čas za ACT trdega materiala zvara – vzorec 5s

**Table 3:** Comparison of results: ACT vs. STCT**Tabela 3:** Primerjava rezultatov ACT in STCT

Sample No.	Material & state	STCT results: [temp/stress/time]	F <sub>CS</sub> /MPa	F <sub>ACT</sub> /MPa	F <sub>CS</sub> /F <sub>ACT</sub>
5s	P91-AW	620/130/381	262	240	1.09
6s	P91-HT	620/130/27	248	137	1.82
8s	P91-HT	620/130/31	249	233	1.07

$$F_{CS} = P_{LM} \cdot R_L / 100$$

Where  $R_L$  is the initial stress of the constant-load short-term creep experiment and  $P_{LM}$  is the Larson-Miller parameter:  $P_{LM} = (20 + \lg t) \cdot T/100$ , with  $T$  = testing temp. in K and  $t$  = time to rupture in h.

### 3 INITIAL MICROSTRUCTURES

#### 3.1 As welded samples 5s and 10s

The main component of the microstructure is acicular low-carbon martensite with high density of tangled dislocations (**Figures 7–10**). In this martensite numerous

spheroidal inclusions of sub-micron size are present. In sample 5s fine cementite and very fine MX particles interact with dislocations, **Figure 8**. In sample 10s, in the inter-bead heat-affected zones along grain boundaries of former austenite, chains of middle-sized  $M_2C_6$  carbides appear, **Figure 9**. In the columnar grain regions of very high dislocation density in sample 10s, (**Figure 10**), hexagonal  $M_2X$  particles as well as MX particles were identified. This martensitic microstructure should be considered as auto-tempered or tempered due to welding cycles, more in sample 10s than in 5s.

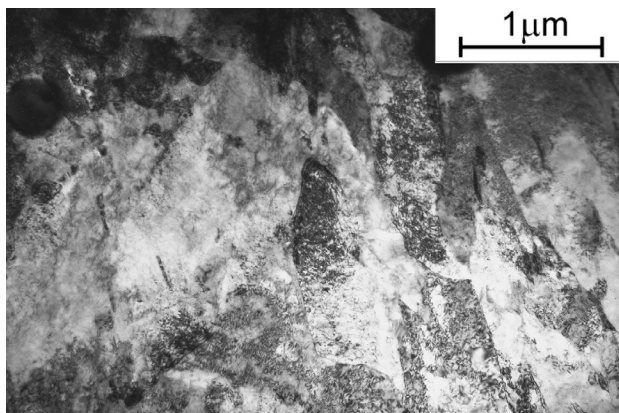


**Figure 7:** Acicular low-carbon martensite in as-welded sample 5s  
**Slika 7:** Acikularni maloogljični martenzit v vzorcu zvara 5s

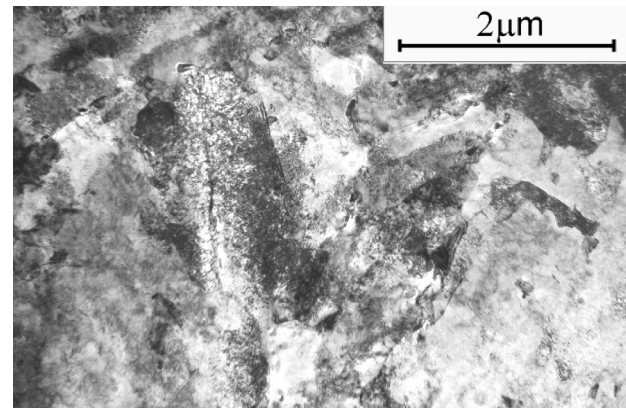


**Figure 9:** Carbides on former austenite grain boundaries in as-welded sample 10s  
**Slika 9:** Karbidi na avstenitnih mejah v vzorcu zvara 10s

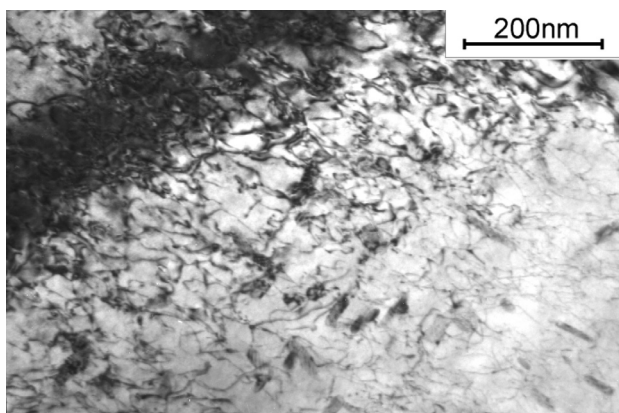


**Figure 8:** Cementite precipitated on dislocation tangles in as-welded sample 5s  
**Slika 8:** Izločki cementita na vozliščih dislokacij v vzorcu zvara 5s

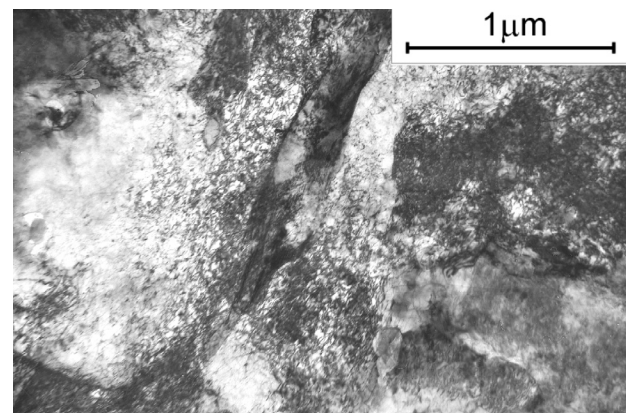


**Figure 10:** High density of dislocations in martensite of as-welded sample 10s  
**Slika 10:** Velika gostota dislokacij v martenzitu v vzorcu zvara 10s

### 3.2 Post-weld heat-treated samples 6s and 8s

The post-weld heat-treated samples 6s and 8s had a tempered martensite microstructure with numerous subgrains, often retaining orientation of the former martensite laths (**Figures 11–13**). In both 6s and 8s samples, the former austenite grain boundaries as well as the post-martensitic lath boundaries were marked with coagulated  $M_{23}C_6$  carbides. A very high dislocation density appeared in grains and subgrains of the inter-bead heat affected zones in sample 8s where also spheroidal carbides were present (**Figure 14**), while the overall microstructure of the sample 6s was much better recovered i.e. the dislocation density in it was visibly lower (**Figure 12**).

## 4 DEVELOPMENT OF MICROSTRUCTURE DURING ACT

Most of the accelerated creep tests were carried out up to appearance of fracture, in order to gain the date representative to the creep life of the materials.

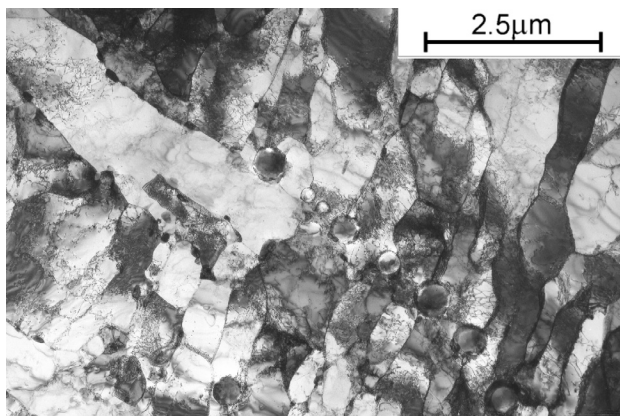


**Figure 11:** Arrays of ferrite subgrains and elongated grains in tempered sample 6s

**Slika 11:** Mreža podzrn ferita in podolgovata zrna v popuščenem vzorcu 6s

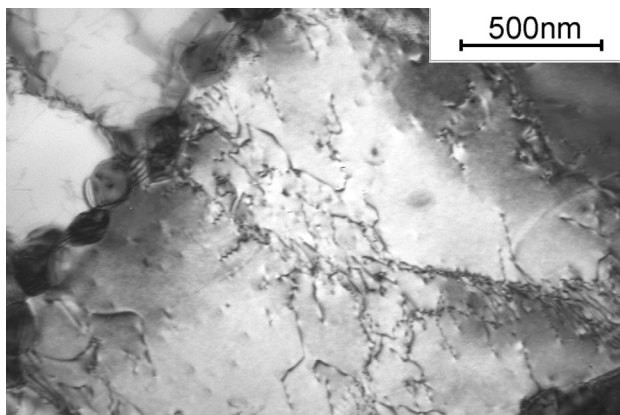


**Figure 12:** Chain of carbides along grain / subgrain boundary in sample 6s

**Slika 12:** Niz karbidov na meji zrno-podzrno v vzorcu 6s

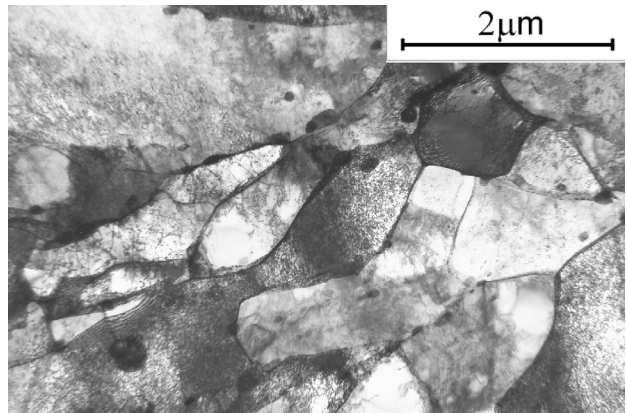


**Figure 13:** Fine ferrite grains/subgrains with high dislocation density in sample 8s

**Slika 13:** Majhna zrna/podzrna ferita v vzorcu 8s

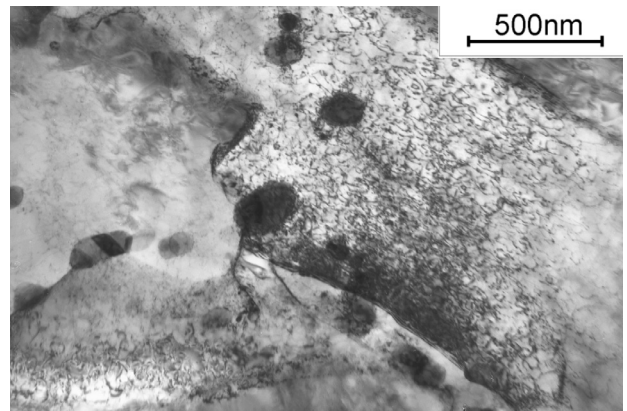


**Figure 14:** Spheroidal carbides in ferrite in the sample 8s

**Slika 14:** Sferoidirani karbidi v feritu v vzorcu 8s

Nevertheless, for the purpose of this study on the sequence of precipitation processes and changes in the weld metal matrix, several tests were interrupted and microstructure of the partly transformed samples examined.

### 4.1 ACT of sample 5s

The accelerated creep test of the as-welded sample results in transformation of the matrix and stimulates precipitation of carbides. Semi-recovered subgrains sized about 1–2 μm form in the matrix before the sample reaches 50 % of its life time in ACT (**Figure 15**). By this stage also the coalescence of subgrains begins, causing oriented chains of carbides to appear within the grains (**Figure 16**). By 80 % of the ACT duration the recrystallising ferrite grains reach 5 μm or more due to the coalescence of finer subgrains (**Figure 17**). At this stage, well-pronounced agglomerates of coagulated carbides can be observed along the former austenite grain boundaries, in particular near to the "triple points" (**Figure 18**). These carbides were mainly of  $M_{23}C_6$  type, although some  $M_6C$  carbides could be identified as well.

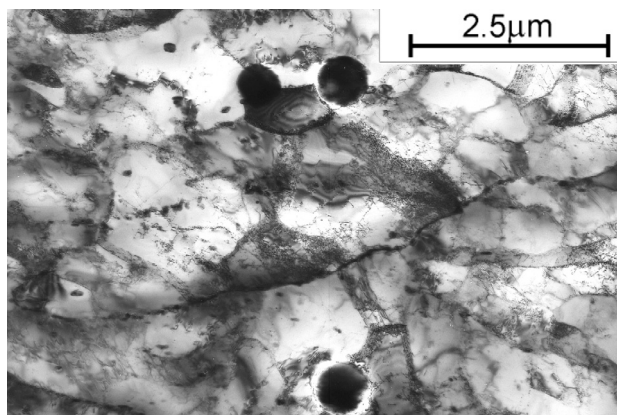


**Figure 15:** Formation of subgrains in sample 5s at half-life in ACT  
**Slika 15:** Nastanek podzrn pri polovici trajnostne dobe vzorca 5s v ACT

The finest precipitates dominating within the recovered post-martensitic subgrains, were positively identified as of cubic MX type, while some larger and elongated appeared to be of hexagonal  $M_2X$  type. On thin foil specimens, taken from near to fracture after

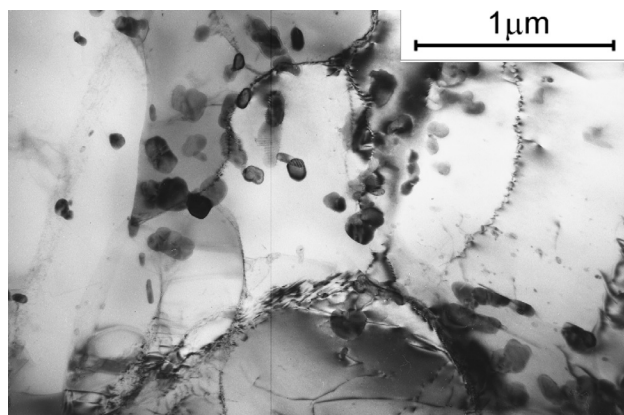


**Figure 18:** Agglomerate of carbides in the sample 5s at 80 % of life in ACT  
**Slika 18:** Aglomerat karbidov v vzorcu 5s pri 80 % trajnostne dobe v ACT

completion of the ACT and examined in TEM, still some of these fine precipitates could be seen within the recrystallised ferrite grains.

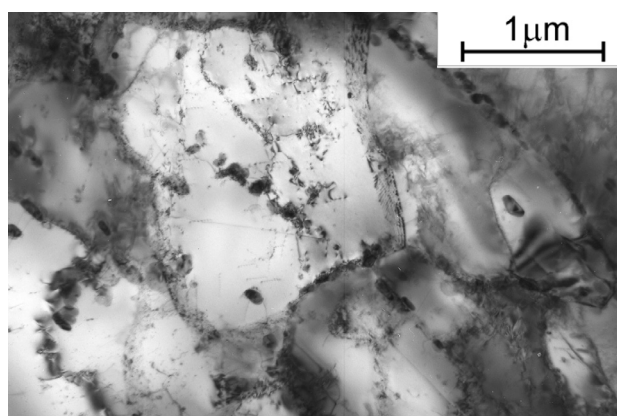


**Figure 16:** Chain of carbides inside growing subgrain in sample 5s  
**Slika 16:** Nizi karbidov v rastočih podzrnih v vzroču 5s

#### 4.2 ACT of samples 6s and 8s

In the over-tempered sample 6s, having already a well-recovered ferrite matrix with low dislocation density before the ACT, the ACT resulted in a fast recrystallisation of the matrix by coalescence of subgrains and coagulation of  $M_{23}C_6$  carbides (**Figures 19 and 20**). The fine precipitates of MX carbo-nitrides disappeared almost entirely and the fine acicular  $M_2X$  phase also could not be found. Some larger precipitates appearing after completion of the ACT were identified as Laves phase.

The sample 8s having an initially less transformed matrix than 6s, with a high dislocation density, around the half of its life in the ACT showed substantial recovery of the dislocation substructure and intensive precipitation of mainly MX phase on the dislocations (**Figures 21 and 22**). This situation persisted till 80 % of

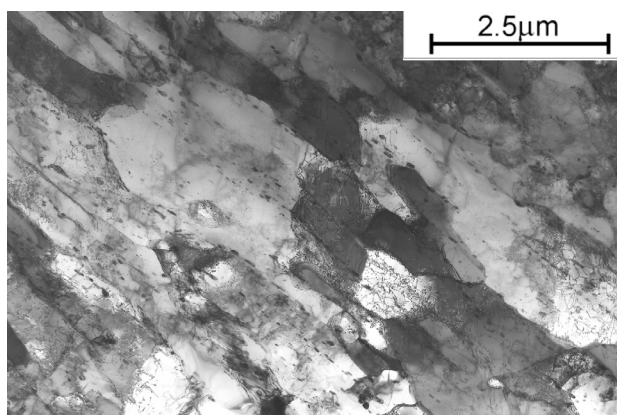


**Figure 17:** Incipient coalescence of subgrains in sample 5s at 80 % of life in ACT  
**Slika 17:** Začetek koalaescence podzrn v vzorcu 5s pri 80 % trajnostne dobe v ACT

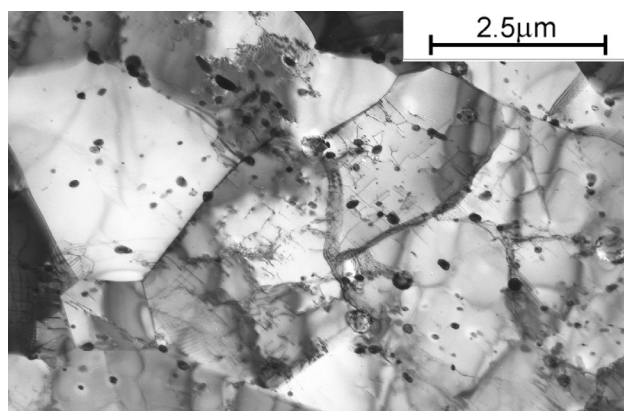


**Figure 19:** Fine recrystallised ferrite grains after ACT in sample 6s  
**Slika 19:** Drobna rekristalizirana zrna ferita v vzorcu 6s po ACT

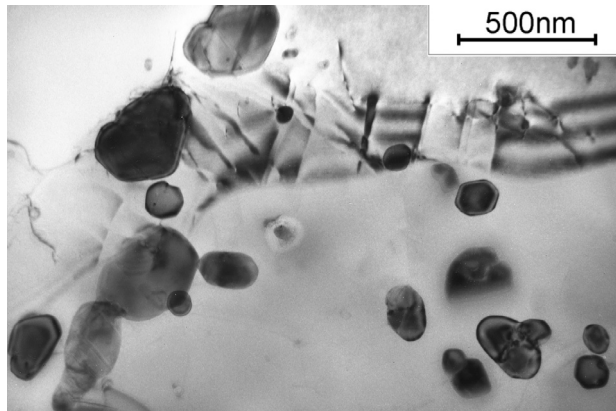


**Figure 20:** Spheroidised carbides after ACT in sample 6s  
**Slika 20:** Sferoidizirani karbidi v vzorcu 6s po ACT

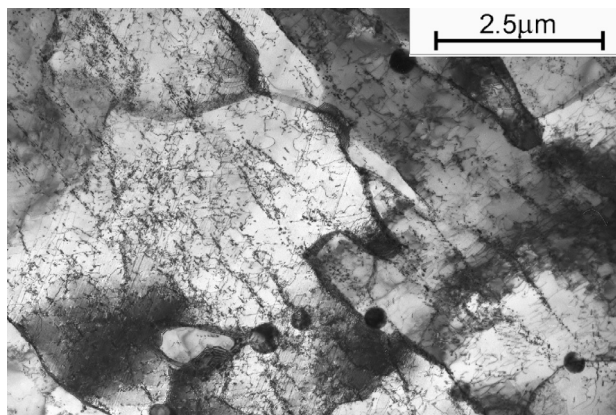


**Figure 21:** Subgrains with medium-density dislocations in sample 8s at half-life in ACT  
**Slika 21:** Podzrno s srednjo gostoto dislokacij v vzorcu 8s po polovici ACT trajnostne dobe

the ACT duration, when visible coarsening of fine precipitates within subgrains occurred and more coagulated carbides of  $M_{23}C_6$  and  $M_6C$  appeared on subgrain boundaries, as well as coalescence of subgrains progressed. Further on, till fracturing of the ACT sample, the fine precipitates within ferrite grains still

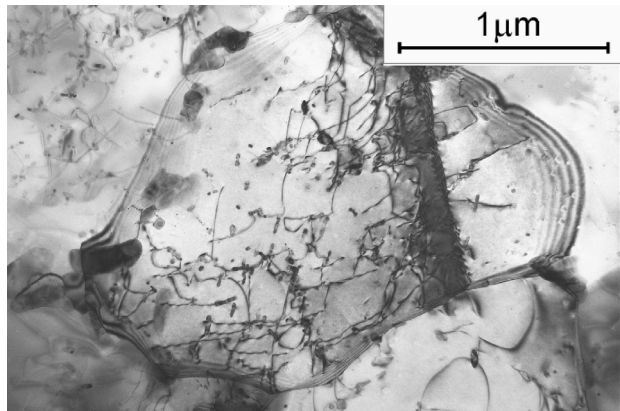


**Figure 23:** Recrystallised small grain with a few fine precipitates after ACT; sample 8s  
**Slika 23:** Majhno rekristalizirano zrno s majhnimi izločki po ACT, vzorec 8s

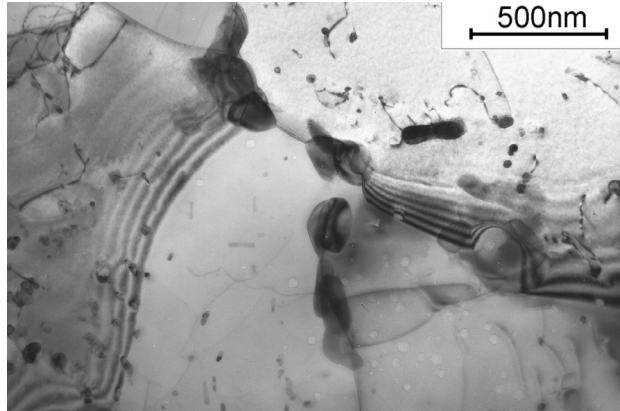


**Figure 24:** Agglomerate of platelike carbides at grain boundary after ACT; sample 5s  
**Slika 24:** Aglomerat ploščatih karbidov na kristalni meji po ACT

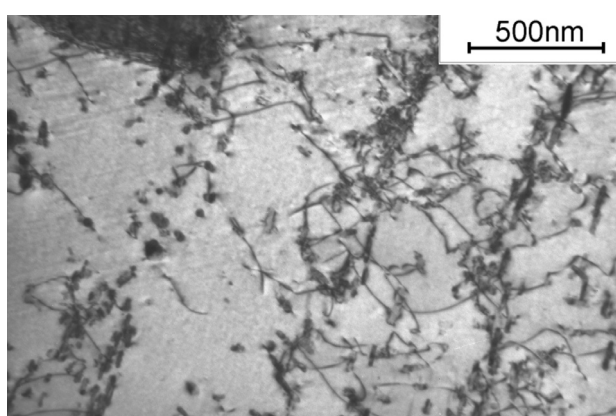


**Figure 22:** MX precipitates on dislocations in sample 8s  
**Slika 22:** Izločki MX na dislokacijah v vzorcu 8s

existed (**Figure 23**), interacting with dislocations as well as pinning ferrite grain boundaries (**Figure 24**). Agglomerates of larger precipitates consisted mainly of  $M_{23}C_6$  and  $M_6C$ , and minor amounts of Laves phase particles were associated with them.

#### 4.3 ACT of sample 10s

The as-welded initial microstructure of sample 10s contained already the  $M_{23}C_6$  carbides along prior austenite boundaries and MX plus  $M_2X$  phases within martensite laths before ACT. In the first half of the ACT duration the  $M_{23}C_6$  carbides grew while the fine MX and  $M_2X$  prevented the dislocation recovery within subgrains (**Figures 25 and 26**). Around 80 % of the ACT life, mixed substructure dominated consisting of small recrystallised grains co-existed with non-recovered and well-recovered subgrains. By the end of ACT, the recrystallised ferrite grains (**Figure 27**), still co-existed with the subgrains, in which fine precipitates interacted with the medium-density configurations of recovered dislocations (**Figure 28**).

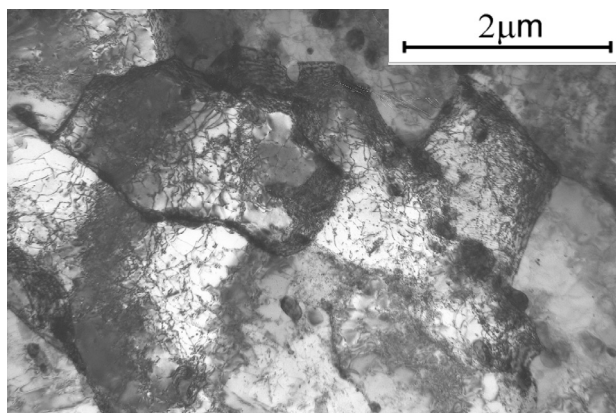


**Figure 25:** Subgrains with high dislocation density at half-life in ACT; sample 10s

**Slika 25:** Podzrno z visoko gostoto dislokacij v vzorcu 10s pri polovici ACT trajnostne dobe

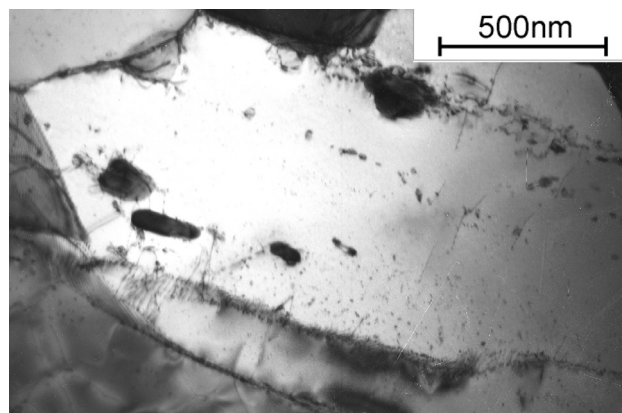


**Figure 27:** Small recrystallised ferrite grain with precipitates after ACT in sample 10s

**Slika 27:** Majhno rekristalizirano zrno z izločki po ACT vzorca 10s

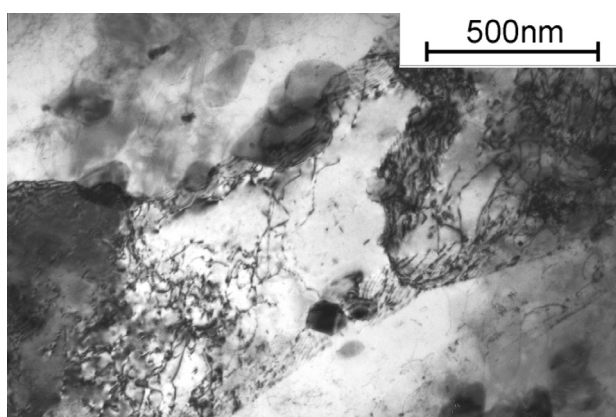


**Figure 26:** Precipitated coagulated carbides in sample 10s

**Slika 26:** Izločeni koagulirani karbidi v vzorcu 10 s

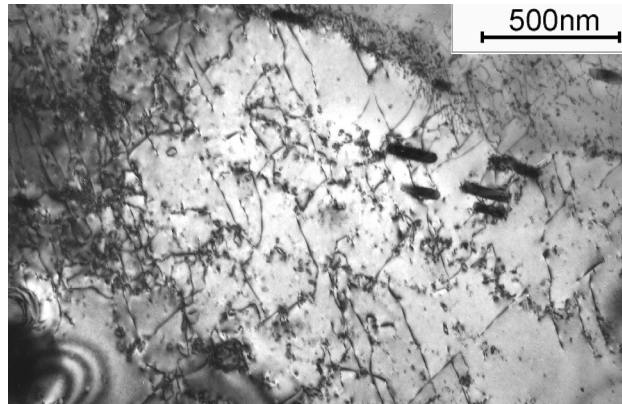


**Figure 28:** Recovered dislocations after ACT interacting with fine carbides; sample 10s

**Slika 28:** Dislokacije po popravi, ki reagirajo s drobnimi karbidi po ACT v vzorcu 10s

## 5 DISCUSSION

The results of this work show the behaviour of some P91 grade weld metals during accelerated creep tests. They allow comparing the standard / lean as-welded material 5s with the optimized one 10s, as well as evaluate the influence of heat treatment on the creep strength on the example of samples 6s and 8s.

Characteristic of the optimized weld metal 10s in its initial state were tortuous prior austenite grain boundaries in the inter-bead heat affected zones (**Figure 29**). This element of the microstructure was retained during the ACT and after completion of the test the precipitated carbides formed a pattern along the meandering grain boundaries (**Figure 30**). This might have been one of major factors responsible for the enhanced creep strength of the sample 10s in ACT and for its long creep life. In the case of the post-weld heat-treated weld metals 6s and 8s, evidently the heat treatment reduces the elevated temperature strength and for the samples tested by ACT in the simulated creep conditions this means reduction of the creep strength

and creep life. The accelerated creep test evidently causes further transformation of the microstructure and

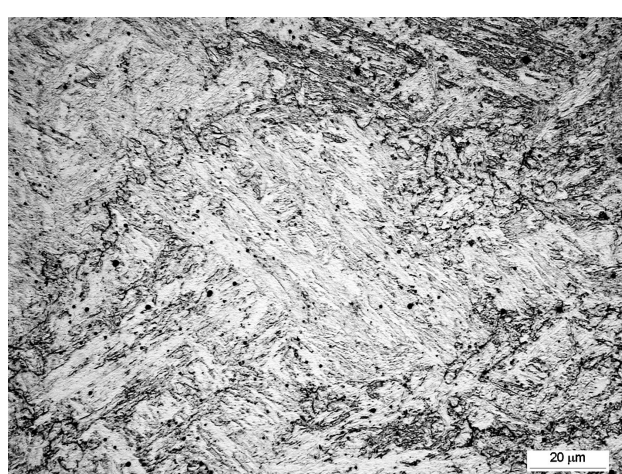


**Figure 29:** Tortuous prior austenite grain boundaries in as-welded sample 10s

**Slika 29:** Vijugasta meja avstenitnega zrna v zvaru vzorca 10 s

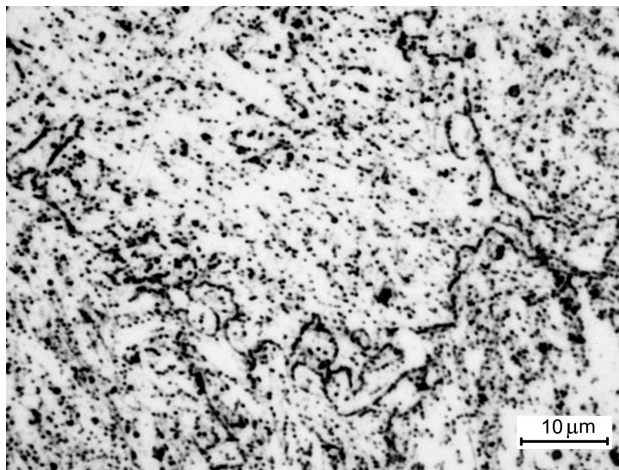


**Figure 30:** Meandering pattern of carbides precipitated after ACT in sample 10s

**Slika 30:** Meandraste oblike karbidov, ki so se izločili po ACT v vzorcu 10s

enhances the precipitation. The question to be answered is whether all the ACT samples fail at the adequate transformation of the microstructure, similar to that of the real creep and are comparable with the results of other creep tests.

The results of EDS x-ray microanalysis are summarized in Table 4 below, together with Thermocalc data. Here (L) indicates the Laves phase present only in a part of the temperature range, while (Z) probably the z-phase not confirmed by diffraction. Then (x) refers to precipitates found on carbon extraction replica taken from ACT fracture while [x] the phases identified by SAD in thin foil specimens in TEM.

This table shows quite good correlation of ACT results with Thermocalc, except for the  $M_7C_3$  presence on the replicas taken from the ACT fracture of the 8s sample. However, this non-equilibrium carbide may form when vast amount of dislocations annihilates, like during the recrystallisation after cold drawing of the

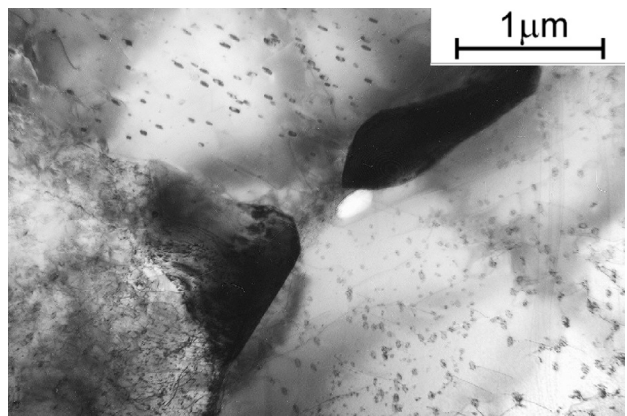


**Figure 31:** Fine MX precipitates in crept for 18 years 1.5Cr-1Mo-0.25V steel

**Slika 31:** Drobni MX-izločki v jeklu z 1.5Cr-1Mo-0.25V, ki je bilo 18 let izpostavljeno lezenju

10Cr-2Si-Mo steel<sup>2</sup>. In fact, the ACT procedure uses a similar phenomenon of generating dislocations, allowing them to "inhale" interstitials and delivering the interstitials to the sites where dislocations annihilate.

Another question is due to the difference shown in Table 3 between ACT and STCT results on sample 6s, considered as over-tempered. In this sample from the beginning till the end of the ACT the finely-dispersed MX phase was almost absent. The MX is considered as an important creep strengthener, stable up to above 700 °C, interacting with dislocations and grain boundaries in steels exposed to creep<sup>7</sup>. Thus, in a 1.5Cr-1Mo-0.25V grade steel after exposure to creep for 18 years the MX is still present in most of ferrite grains (**Figure 31**). In the STCT tests of this research, the fine MX phase particles were only found in the as-welded material 5s, in minor amount of subgrains on thin foils taken from near to grip portions of the samples. Their traces could also be found in gauge portion of 8s STCT sample (**Figure 32**), but entirely not in the neck portion of 5s STCT

**Table 4:** Phase compositions of selected P91 weld metals (EDS microanalysis from carbon extraction replicas)

**Tabela 4:** Fazna sestava izbranih P91-zvarov (EDS-analiza na ogljikovih ekstrakcijskih replikah)

Sample & treatment	Accelerated creep test conditions	Phase composition / carbides						
		$M_7C$	$M_{23}C_6$	$M_7C_3$	$M_2X$	$M_6C$	MX	Laves etc.
5s – AW MMA, P91	Initial state	[x]	x				x	
	STCT – 620 °C/130/381h		x			x	x	
	ACT – 600 °C/26.6 ks		x			x	x	
8s – HT MMA, P91	STCT – 620 °C /130/31h		x				x	
	ACT – 600 °C/24.5 ks		x	(x)		x	x	L
5s & 8s	Thermocalc phase content at 500–620 °C		X			X	X	(L)
10s – AW MMA, P91	Initial state		x		x		x	
	ACT – 600 °C/82.6 ks		x			[x]	x	(Z)
10s	Thermocalc phase content at 500–620 °C		X			X	X	

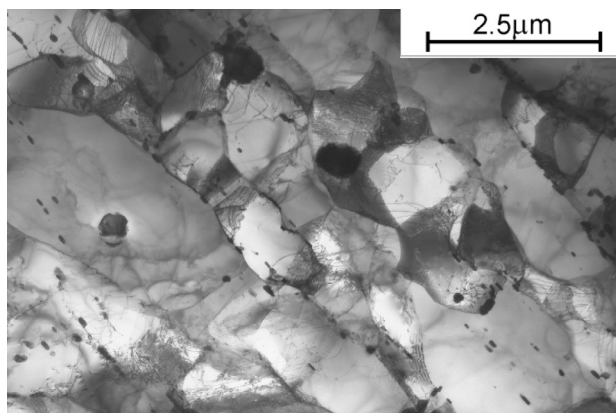


**Figure 32:** Subgrains and few fine carbides in gauge portion of 8s sample after STCT

**Slika 32:** Podzrna in drobni karbidi v merilni dolžini vzorca 8s po STCT

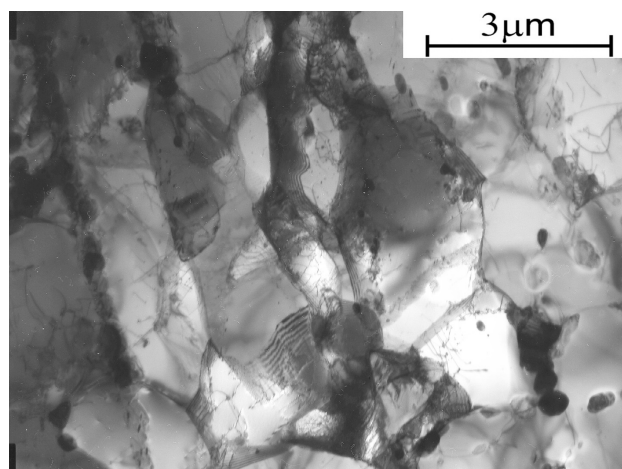


**Figure 34:** Elongated grains and subgrains of ferrite in crept sample 1344/3

**Slika 34:** Podolgovata zrna in podzrna ferita v vzorcu 1344/3, ki je bilo izpostavljen lezenju

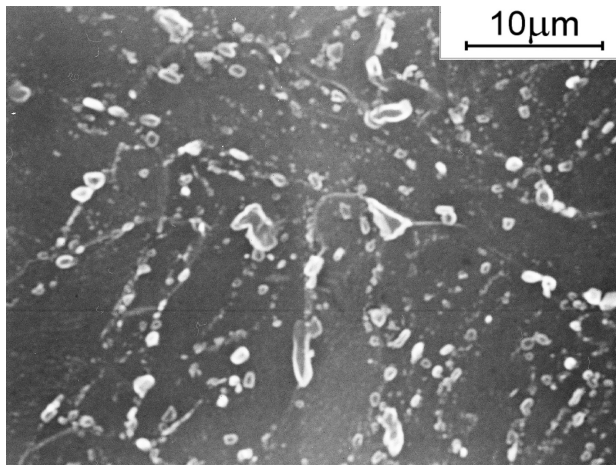


**Figure 33:** Different size carbides in crept for 9 years P91 weld metal; sample 1344/3

**Slika 33:** Karbidi različne velikosti v zvaru jekla P91, ki je bil izpostavljen lezenju 9 let, vzorec 1344/3

sample, where refinement of ferrite grains dominated certainly resulting from localized substantial strain. This grain refinement in the neck portion of the STCT samples was also characteristic of samples 6s and 8s.

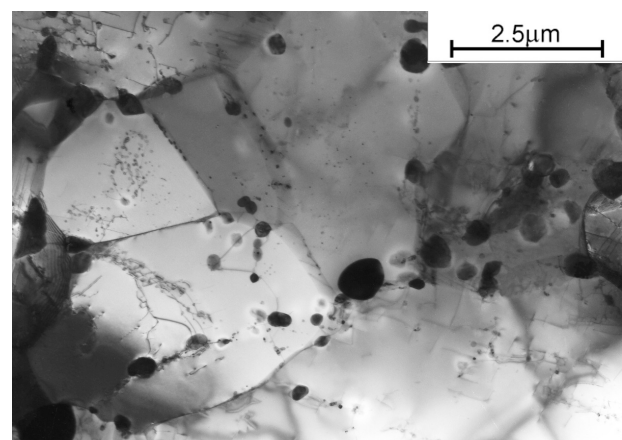


**Figure 35:** Recrystallised ferrite grains with coagulated  $M_{23}C_6$  carbides; sample 1344/3

**Slika 35:** Rekrystalizirano zrno ferita s koaguliranimi karbidi, vzorec 1344/3

As in this research the long-term creep tests were not carried out, a comparison is made here with the P91

**Table 5:** Chemical compositions of reference P91 weld

**Tabela 5:** Kemična sestava referenčnega zvara P91

Sample	Element, w/%									
	C	Mn	Si	Cr	Ni	Mo	V	Ti	Nb	N
KA 1344/3/ weld	0.10	0.42	0.28	8.01	0.14	0.92	0.21	0.00	0.060	0.045

**Table 6:** Phase compositions of reference P91 weld

**Tabela 6:** Fazna sestava referenčnega zvara P91

Sample	Creep conditions	Phase composition / carbides						
		$M_3C$	$M_{23}C_6$	$M_7C_3$	$M_2X$	$M_6C$	$MX$	Laves
KA1344/3 weld	Exploited $\approx 600$ °C/ 170 bar/9 years		x				x	L
KA1344/3	Thermocalc phase content at 550–640 °C		X				X	L

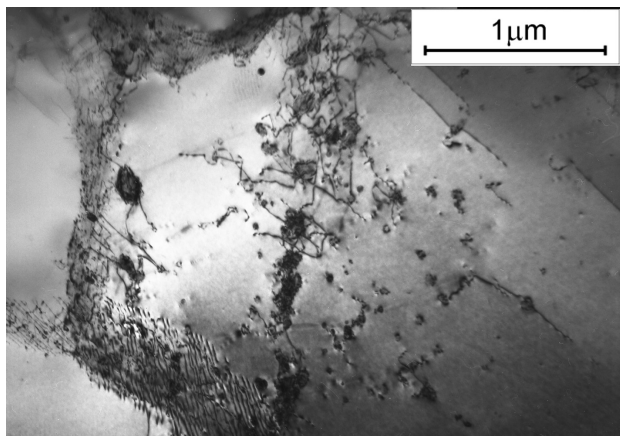


**Figure 36:** Fine MX precipitates interacting with dislocations in sample 1344/3

**Slika 36:** Drobni MX-izločki, ki reagirajo z dislokacijami v vzorcu 1344/3

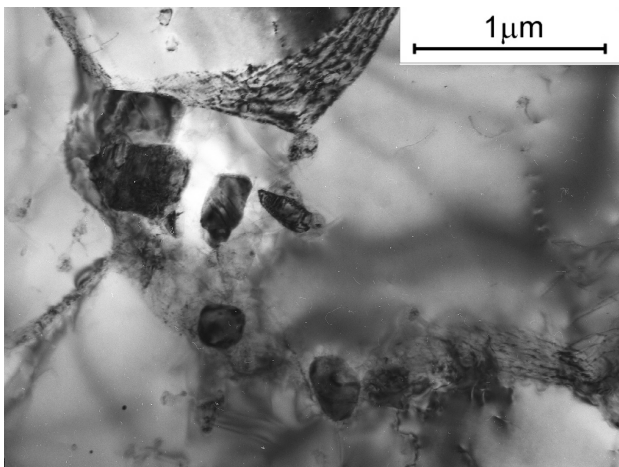


**Figure 38:** Medium size MX and  $M_{23}C_6$  precipitates in sample 1344/3

**Slika 38:** Srednjeveliki izločki MX in  $M_{23}C_6$  v vzorcu 1344/3

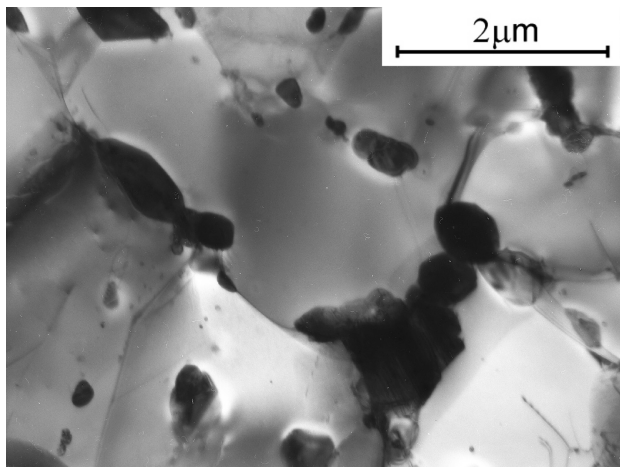


**Figure 37:** Agglomerates of  $M_{23}C_6$  carbides in recrystallised matrix of sample 1344/3

**Slika 37:** Agmomerati  $M_{23}C_6$ -karbidov v rekristalizirani matici v vzorcu 1344/3

grade weld metal of a power plant component, marked KA 1344/3, which failed after exposure to creep at  $\approx 600$  °C/170 bar/9 years. The chemical composition of this reference weld is given in the **Table 5**, while the results of the phase identification are summarized in the **Table 6**.

Microstructure of this reference weld after 9 years exposure to creep, consisted of post-martensitic / ferritic matrix with precipitated phases of various sizes, some very large (**Figure 33**). A closer look into this microstructure by means of TEM on thin foil specimens, revealed the presence of numerous fine grains / subgrains retaining the post-martensitic orientation (**Figure 34**), as well as recrystallised equiaxial ferrite grains (**Figure 35**), with usually random distribution of carbides.

In numerous fine grains and subgrains some very fine MX precipitates were found interacting with dislocations

and low-angle boundaries (**Figure 36**). On former austenite grain boundaries and in the intersecting regions of former martensite laths, colonies of large carbides appeared, consisting of mainly  $M_{23}C_6$  carbides and with a few MX precipitates (**Figure 37**). Other medium-size MX precipitates were found in the separate colonies, interacting with ferrite grain boundaries (**Figure 38**). The large  $M_{23}C_6$  carbides often consisted of several crystallites separated by stacking faults and low angle boundaries (**Figures 39–40**). In several cases large  $M_6C$  carbides were identified, usually growing on the  $M_{23}C_6$  carbides (**Figures 41 and 42**). Numerous of the large ( $>500$  nm)  $M_{23}C_6$  carbides possessed a substructure of "acicular type", which could be identified as a sandwich of stacking faults and/or very-thin ( $<10$  nm) plate-like crystals (**Figures 43 and 44**). SAD patterns from such substructure exhibit double / multiple diffraction effects as well as reveal details of relative rotations between the

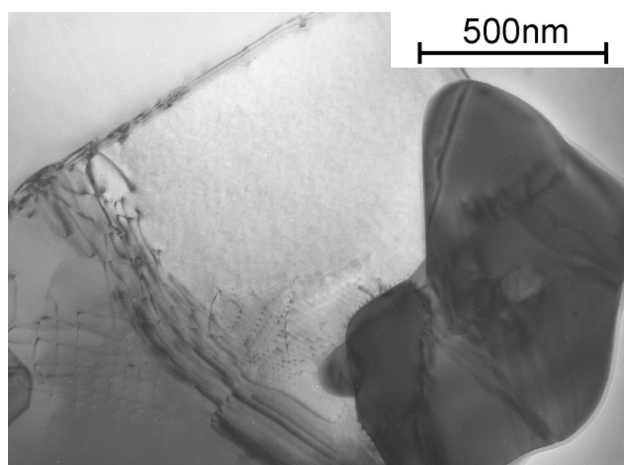


**Figure 39:** Large  $M_{23}C_6$  carbide in recrystallised ferrite; sample 1344/3

**Slika 39:** Velik izloček karbida  $M_{23}C_6$  v rekristaliziranem feritu, vzorec 1344/3

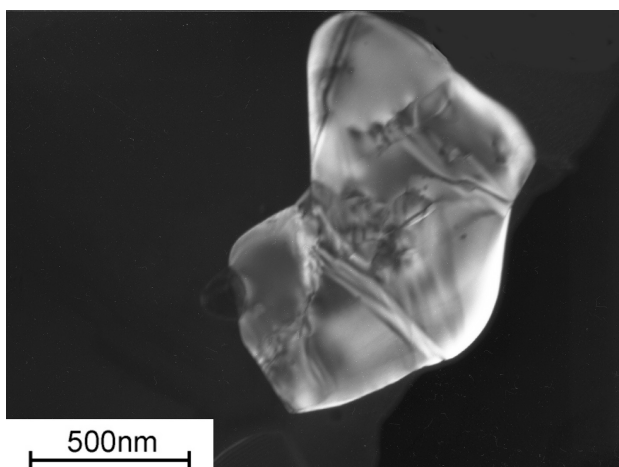


**Figure 40:** Dark field image of Figure 39: visible substructure / defects in the carbide

**Slika 40:** Karbid s slike 39 v temnem polju. Vidne so podstruktura in napake v karbidu

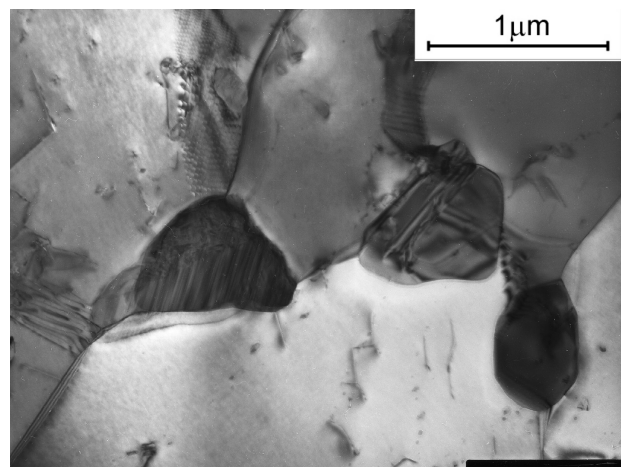


**Figure 43:**  $M_{23}C_6$  carbides with stacking faults and fine plate-like substructure

**Slika 43:** Karbidi  $M_{23}C_6$  z napakami zloga in fino ploščato podstrukturo

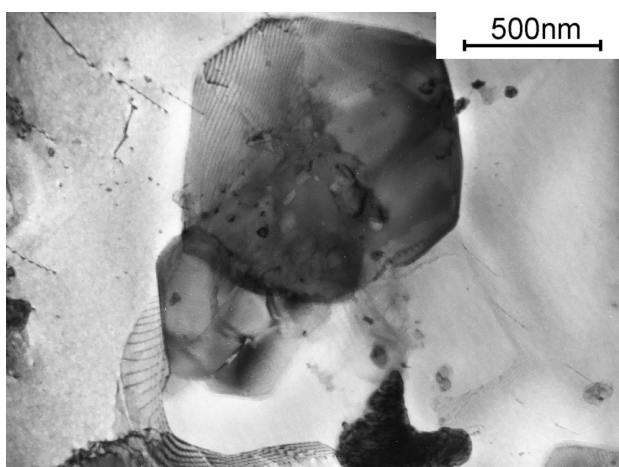


**Figure 41:** Large thin plate-like  $M_6C$  carbide overlapping with  $M_{23}C_6$  carbide

**Slika 41:** Velik ploščat izloček karbida  $M_6C$ , ki se prekriva s karbido  $M_{23}C_6$



**Figure 44:** Diffraction from Figure 43, showing double-diffraction effects

**Slika 44:** Difrakcija s slike 43 z dvojnim difrakcijskim odsevom

platelets. In some cases Laves phase  $Fe_2Mo$  was identified as appearing in the sandwich structure.

In general, in the reference material 1344/3 the microstructure was inhomogeneous, which is typical for the weld metal. Accordingly, during creep it transformed non-uniformly, showing large precipitates next to completely recrystallised grains and some fine particles, mainly MX, interacting with dislocation and low angle boundaries in the regions where post-martensitic grains were retained.

As to the finely dispersed MX phase, which should support the creep strength, it was rather seldomly observed; more often the coagulated MX carbo-nitrides were present. It was recently suggested that the vanishing of the MX phase and decay of the creep strength might be due to formation of the Z-phase<sup>8</sup>. Although the observed features and chemical composition of the 1344/3 weld metal might have suggested that the Z-phase should appear in it, this phase was not

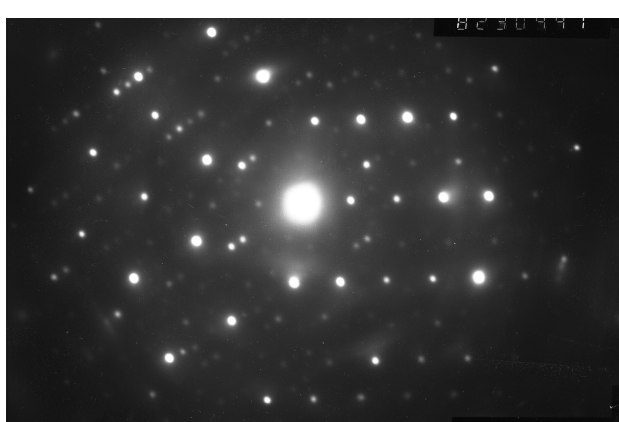


**Figure 42:** Diffraction from carbides of Figure 41, with double-diffraction effects

**Slika 42:** Difrakcija karbidov na sliki 41, dvojna difrakcijska slika

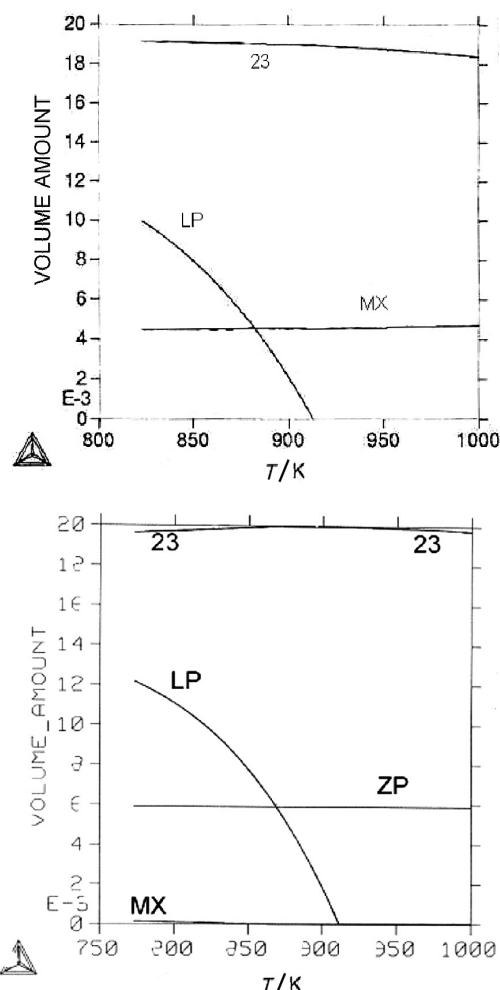


**Figure 45:** Thermocalc graphs for the reference P91 weld metal, for equilibrium state, without and with Z-phase (ZP); symbols: 23 =  $M_{23}C_6$ , LP = Laves phase

**Slika 45:** Thermocalc diagrami za referenčni var P91 za ravnotežno stanje brez in z Z-fazo; označbe: 23 =  $M_{23}C_6$ , LP = Lavesova faza

found in TEM/EDS investigation neither on carbon extraction replicas nor on thin foils.

From the above graphs (**Figure 45**) it is evident that when the Z-phase is present then the MX carbo-nitride disappears. Therefore the main question to be solved in

further research is what caused the substantial decrease of the MX amount in the weld 1344/3, which had to be decommissioned prematurely due to the decrease of its high temperature strength. The lack of the Z-phase there might be explained by the failure occurring much before the phase equilibrium is reached. But this also confirms that the Z-phase was not here involved in the dissolution of the MX and decay of the properties. On the contrary, the Z-phase (or similar compound) appeared after ACT in the optimized P91 test weld metal 10s. However in this 10s material up to the failure of the ACT sample a large amount of the MX phase was still present.

## 6 CONCLUSIONS

1. The accelerated creep test on Gleeble (ACT) transforms microstructure of creep resisting weld metal in less than 50 hours similarly to that calculated by Thermocalc for phase equilibrium conditions.
2. The ACT gives results comparable with short-term creep tests (STCT), nevertheless microstructural investigations are helpful to explain differences if these occur.

## 7 REFERENCES

- <sup>1</sup>Kidin I. N. Fizicheskie osnovy elektrotermicheskoi obrabotki metallov i splavov; Izd. Metallurgia, Moscow 1969 (in Russian)
- <sup>2</sup>Mandziej S., Marciniaik J. TEM investigations on in-situ transformation of  $M_{23}C_6$  carbides; Proc XIth Int Congr on Electron Microscopy, Kyoto 1986, 1271–72
- <sup>3</sup>Mandziej S. T. Low-energy dislocations and ductility of ferritic steels; Materials Science & Engineering A, 164 (1993), 275–280
- <sup>4</sup>Mandziej S. T., Výrostková A. Accelerated creep testing (ACT) procedure for weld metals using Gleeble systems, Gleeble Application Note, DSI, Poestenkill NY, USA, 2001
- <sup>5</sup>Mandziej S. T., Výrostková A. Accelerated creep testing of P91 weld metals, IIW Doc II-1461-02.
- <sup>6</sup>Pepe J. J., Gonyea D. C. Constant displacement rate testing at elevated temperatures in: Fossil Power Plant Rehabilitation, ASM International, Proc Int Conf, Cincinnati OH, Feb.1989, 39–45
- <sup>7</sup>Woodhead J. H., Quarrell A. G. Role of carbides in low-alloy creep resisting steels; Journal of Iron and Steel Institute, (1965) June, 605–620
- <sup>8</sup>Danielsen H. K. and Hald J. Behaviour of Z-phase in 9–12 % Cr steels, Energy Materials, 1 (2006) 1, 49–57



## ZVEZA MED ANALIZNIMI REZULTATI – KARBONATNA BOMBA IN TERMIČNA ANALIZA

### CONNECTION BETWEEN ANALYSIS RESULTS – CARBONATE BOMB AND THERMAL ANALYSIS

Željko Pogačnik

Salonit Anhovo, d. d., Vojkova 1, 5210 Deskle, Slovenija  
zeljko.pogačnik@salonit.si

Prejem rokopisa – received: 2007-09-27; sprejem za objavo – accepted for publication: 2007-10-24

Pri spremljanju reaktivnosti karbonatnih kamnin je treba upoštevati njihove geološke danosti, kot sta struktura in tekstura. Obstaja več načinov določanja masnega deleža karbonata v kamnini; cementna industrija in proizvodnja apna uporablja največkrat TGA-DTA in XRF analizo (zadnja ne poda absolutne vrednosti), medtem pa naftna industrija prisega na t. i. hitro analizo, t. j. uporabo karbonatne bombe (Müller and Gastner, 1971).

V prispevku želim predstaviti primerljivost med analiznima postopkoma, ki temeljita na kislinskem razklopu ter procesu termičnega razpada različnih sedimentnih kamnin. Analizi nista pomembni le za določitev masnega deleža karbonatov, omogočata tudi dopolnjeno sledljivost porabe toplotne energije pri proizvodnji OPC-klinkerja. V ta namen so bili izbrani vzorci flišnih kamnin, ki nastopajo na področju Anhovega. Korelacija rezultatov med TGA-DTA, XRF in XRD analizo ter kislinskim razklopom karbonatne bombe je pokazala, da znaša za določitev Mg karbonatov s termično analizo in analizo karbonatne bombe, faktor korelacije 0, 97.

Ključne besede: analizne tehnike, karbonatna bomba, termična analiza, mineralogija

During the following of carbonate rocks reactivity the geological characteristics like texture and structure must be consider. There are several analyses method in the cement and lime industry, to determinate an amount of  $\text{CaCO}_3$  during the thermal decomposition of rocks. The most uses the TGA-DTA and XRF and analysis (where the last one cannot give an absolute value of carbonate) in the meantime the petroleum industry swear to carbonate bomb analysis (Müller and Gastner, 1971).

In this work I wish to present the comparison results between two analytical methods; acid decomposition and process of thermal decomposition of carbonate minerals. These two analyses are not important only for carbonate determination, during OPC clinker and lime production connected to dissociation of mineral raw material. At the same time they make possible control the amount of consumed heat energy in the process per unit of product. For this purpose We analysed some samples of flyschoid rocks from Anhovo area. The determination results of Mg carbonates with TGA-DTA, XRF, XRD analysis and results of acid decomposition of carbonates by carbonate bomb technique demonstrate a correlation factor of 0,97.

Key words: analaysis procedure, carbonate bomb, thermal analysis, mineralogy

Salonit Anhovo, d. d., litoloških komponent (**slika 1** in **tabela 1**).

Nekatere komponente v tehnološkem procesu lahko nadomestimo tudi s sekundarnimi mineralnimi surovinami <sup>2</sup>, s čimer znižamo porabo toplotne energije ter emisije toplogrednih plinov (TPG). Portland <sup>3</sup> navaja, da je cementna industrija odgovorna za masni delež od 8 do 12 % emisij TPG na letnem nivoju, upoštevajoč izgo-

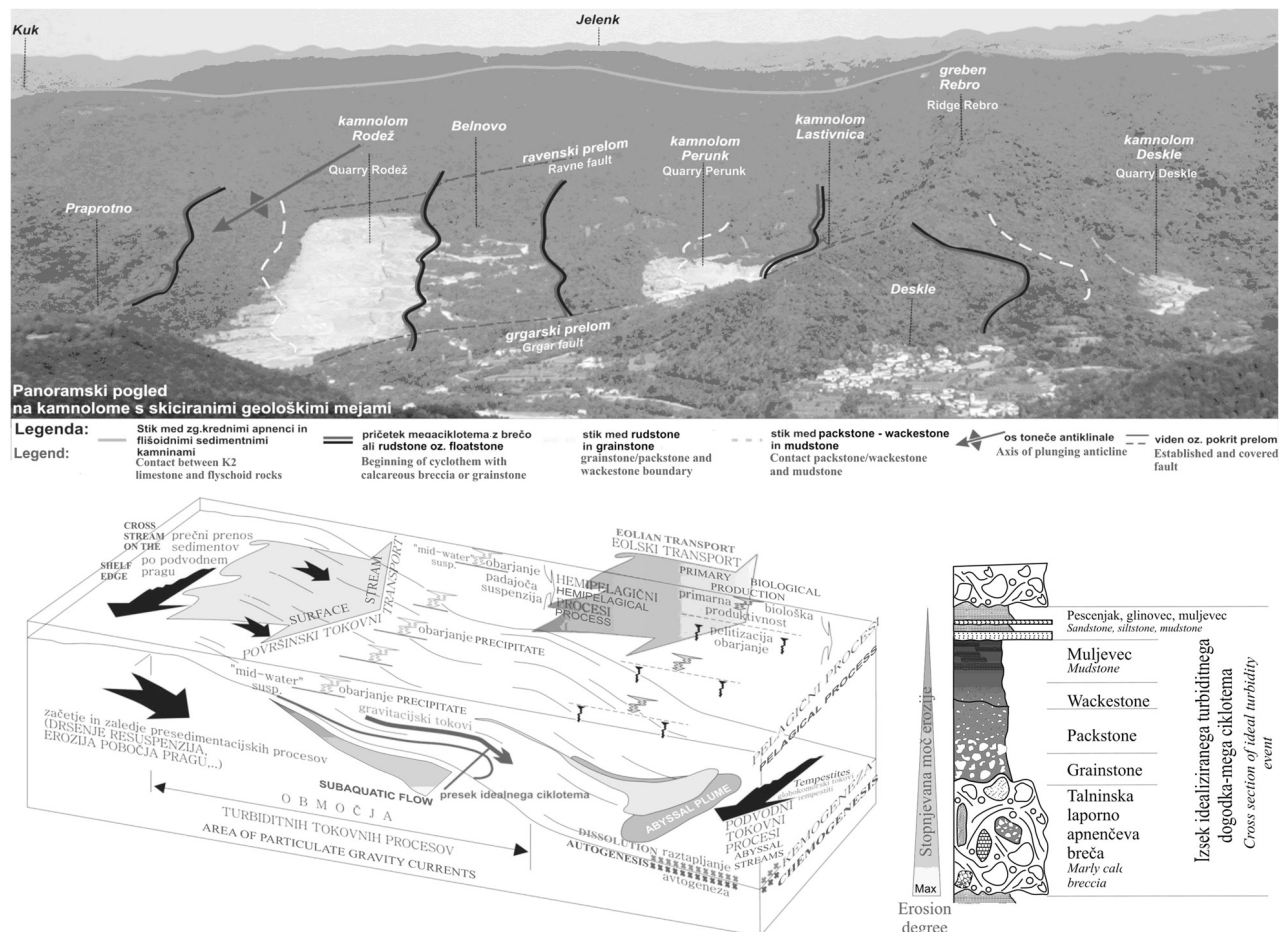
## 1 UVOD

Za izdelavo portlandskega cementa OPC se uporablja mešanica karbonatnih in silikatnih kamnin v ustreznem masnem razmerju. Pri izbiri pravilnega razmerja ima ključen pomen oksidna sestava posameznih kamnin ali v kompleksnejšem sistemu, kot v primeru cementarne

**Tabela 1:** Razlaga poimenovanja litoloških komponent <sup>1</sup>, za katere velja, da delci med seboj niso bili povezani med procesom sedimentacije (AD, AS in AL – notranja nomenklatura komponent mineralne surovine)

**Table 1:** Deffinition of the lithological component <sup>1</sup>. AD, AS and AL are internal nomenclature of lithological units

MUDSTONE	Sestavlajo karbonatni muljevec in delež zrn, ki ne presega 10 mas.% premera med 0,03 mm in 2 mm • Mud supported matrix, with less than 10 % of grains which diameter ranged between 0,03 mm and 2 mm	AD
WACKESTONE	Sestavlajo pretežno karbonatni muljevec kot osnova ter 10 mas.% do 50 mas.% zrn (zrna "lebdijo" v muljasti osnovi) • Matrix consists mainly of mud (particles of clay and fine silt) with more than 10 % of grains larger than 2 mm.	AD
PACKSTONE	Ima že zrnato podporo oz. zrna se med seboj dotikajo. Karbonatni muljevec nastopa le v medzrnskem prostoru • Grain supported with mud particles of clay and fine silt size. Grains are larger than 2 mm.	AS
GRAINSTONE	Ne vsebuje karbonatnega muljevca, nastopajo le zrna v medprostoru, iz katerega se izloča karbonatni cement • Grain supported without lime mud.	AL



**Slika 1:** Idealiziran presek litoloških komponent ciklotema v kamnolomu Rodež s pripadajočo geologijo (panoramska fotografija) in zgodovino nastanka

**Figure 1:** An idealised presentation of lithological component from Rodež quarry (upper panoramic photo) with its corresponding sedimentological process and lithology of cyclothem

revanje vseh fosilnih goriv, kjer je poglavitna emisija  $\text{CO}_2$ . Letno znaša ta delež približno 1 Gt od vseh 13 Gt zavedenih TPG-emisij.

Namen te raziskave je potrditi domnevo, da je večji del MgO vezan v nekarbonatnih mineralih. V termo-dinamičnem pogledu je najzanesljivejši a zamuden vpogled pridobljen s termičnimi metodami. Termični razpad karbonatnega minerala, ki sestavlja sedimentno kamnino je odvisen od njegove oblike in elementne sestave, ki sta odsev njegovega nastanka. Stopnja dekarbonatizacije karbonatnih sedimentnih kamnin  $\varphi$ , je definirana kot  $\varphi = 1 - (\varphi_{\text{CO}_2(\text{CaCO}_3)}) / (\varphi_{\text{CO}_2(\text{celotni})})$  v temperaturnem intervalu od 400 °C do 1000 °C<sup>4</sup>. Funkcija dekarbonatizacije podaja reakcijo v trdi fazi, ki je pomembna pri študiji procesa kalcinacije v toplotnem izmenjevalcu<sup>5</sup>. Raziskave mnogih avtorjev, ki jih Bucchi navaja v svojem prispevku<sup>4</sup>, kažejo linearno časovno odvisnost med dekarbonatizacijo zrna in njegovim premerom. V cementni industriji se za napoved masnega deleža karbonata uporablja rentgenska fluorescenčna analiza – XRF, ki pa količino analita podaja na osnovi preračunanega deleža  $\text{CaCO}_3$ , v kar je

všteta tudi sistematična analitska napaka, vezana na količino CaO in MgO, ki nista vezana na karbonat. Način določitve deleža karbonata v betonih je na podoben način uporabila tudi Géraldine s sodelavci<sup>6</sup>. Slednja je komplementarno združila termogravimetrično (TGA) in klasično kemijsko analizo.

## 2 IZHODIŠČA, METODE DELA IN IZBOR VZORCEV

Rezultati predhodnih raziskav<sup>2</sup> kažejo, da je delež p. CaO (prostega apna) odvisen predvsem od genetskih lastnosti kamnin. Visokokarbonatne litološke komponente so kamnine tipa packstone – grainstone topotopno manj potratne (v pogledu procesa dekarbonatizacije), bolj reaktivne pa so kamnine strukturnega tipa mudstone – wackestone<sup>7</sup>. Geneza teh je vezana na globokomorske gravitacijske procese (**slika 1**).

Za določitev dejanskega deleža Ca in drugih Mg-karbonatov, s tem pa emisije TPG, so bile izvedene rentgenska difrakcijska-XRD in flourescenčna-XRF-analiza, termična – TGA-DTA- in primerjalna analiza s

karbonatno bombo – KB. Statistično opredeljivi vzorci mineralne surovine<sup>2</sup> so bili zmleti in homogenizirani v laboratorijskem mlinu Herzog, katerega kapaciteta znaša 100 g merjenca. S takim načinom priprave vzorca je bil zagotovljen minimalni vpliv velikosti delcev<sup>8,9,10</sup> na analitski postopek. Vzorce smo izpostavili intervalu mletja do 30 s; interval je bil opredeljen na osnovi masnega deleža karbonata.

Snemalni pogoji na rentgenski cevi inštrumenta ARL 8480 za XRF-analizo so bili postavljeni na napetost 30 kV in tok 80 mA, snemalni čas je bil 40 s. Difraktogrami merjencev so bili posneti na Kemijskem inštitutu in Institutu "Jožef Stefan" v Ljubljani (difraktometer Siemens D-5000). Uporabljena je bila refleksijska tehnika in CuK $\alpha$  žarek v območju od 2° do 74°, po koraku 2θ 0,036°, in integracijskim časom 2 × 5 s, z divergenčno in protisipno režo, nastavljeno na 20 mm osvetlitve vzorca, ter sprememno režo 0,6 mm<sup>11</sup>. Difraktogrami klinkerjev so bili posneti z refleksijsko tehniko in CuK $\alpha$ -radiacijo v območju 2θ od 10° do 65°, s korakom 2θ 0,03°, integracijskim časom 2 × 3 s, z divergenčno in protisipno režo, nastavljeno na 20 mm osvetlitve vzorca, ter sprememno režo 0,6 mm<sup>12</sup>. Merjenci so bili analizirani z računalniškim programom *Crystallographica Search Match*<sup>11</sup>.

Kislinski razklop vzorcev je bil izведен na osnovi protokola analize s "karbonatno bombo-KB", ki sta ga objavila Müller in Gastner<sup>13</sup>. Pri termični preiskavi smo uporabili analizator STD 2960 *Simultaneus* TGA-DTA. Meritve smo opravljali z ustaljenim protokolom pri

laboratorijski temperaturi 1200 °C in s temperaturnim korakom segrevanja 10 °C/min. Ta omogoča spremljavo temperaturnega razpada mineralnih struktur in s tem določitev temperaturnih parametrov dekarbonatizacije na osnovi literaturnih podatkov<sup>8,14,10</sup>. Za kalibracijo inštrumentov smo uporabili standard kalcita<sup>1</sup>.

Reaktivnost merjenca je bila določena z meritvo količin, ki so neposredno ali posredno vezane na strukturo mineralov<sup>4</sup>. V tehnološkem procesu je temperatura pričetka (*onset* temperatura) reakcije najpomembnejši faktor, saj pove, pri kateri temperaturi se prične masa in zgradba minerala spremniti zaradi dovedene topote. Maksimalna temperatura –  $T_{\max}$  ali temperatura pri kateri je proces dosegel svoj vrh, je bila določena s prvim odvodom gravimetrične krivulje, temperatura pričetka reakcije, kot jo to poimenuje Yen s sodelavci<sup>15</sup> in jo že Ramachandran nakaže v svojem delu<sup>14</sup>, pa na osnovi drugega odvoda.

### 3 REZULTATI

V tabeli 2 so navedeni masni deleži oksidov in mineralov, pridobljeni s posameznimi preiskovalnimi metodami.

Primerjavo kvantitativne emisije CO<sub>2</sub> glede na posamezno preiskovalno metodo ponazarja slika 2.

Iz rezultatov, ki jih ponazarjati tabeli 2 in 3 lahko izračunamo delež MgO, ki ni vezan v kamnini v obliki karbonata.

**Tabela 2:** Rezultati uporabljenih preiskovalnih metod (XRF, XRD, TG-DTA analize in karbonatne bombe K.B.)  
**Table 2:** Results of XRF, XRD, TG – DTA and "carbonate bomb" analysis

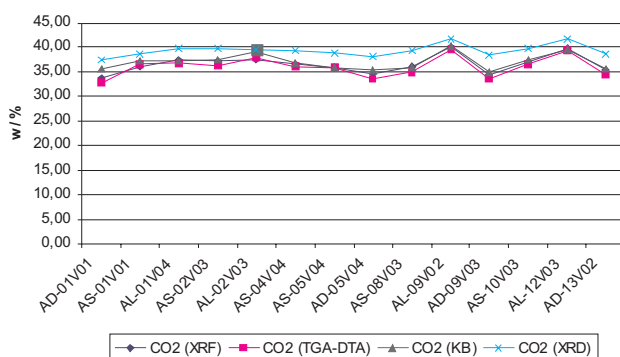
	XRF				XRD (w/%)				K. B.		DTA-TG	
	CaO	MgO	CO <sub>2</sub>	CaCO <sub>3</sub>	Kalcit Calcite	CO** <sub>2</sub>	Enstatit Enstatite	Muskovit Muscovite	Klorit Chlorite	CaCO <sub>3</sub>	CO <sub>2</sub>	CaCO <sub>3</sub>
MERJENEC SAMPLE												
AD 01V01	42,97	1,36	33,76	76,70	85,50	37,62	3,27	1,21	3,06	81,09	32,84	74,64
AS 01V01	46,04	1,26	36,17	82,18	88,12	38,77	3,09	0,69	2,28	84,58	36,59	83,16
AL 01V04	47,92	1,10	37,65	85,54	90,86	39,98	1,72	0,42	1,31	84,58	36,88	83,82
AS 02V03	47,44	1,11	37,26	84,67	90,44	39,79	2,15	0,62	1,32	85,57	36,48	82,91
AL 02V03	47,90	1,09	37,63	85,49	89,97	39,59	2,47	0,27	1,45	89,05	38,02	86,41
AS 04V03	46,51	1,16	36,54	83,02	89,78	39,50	2,22	0,45	1,81	83,58	36,25	82,39
AS 05V04	45,68	1,23	35,88	81,54	88,74	39,05	2,04	0,83	1,86	81,59	35,97	81,75
AD 05V04	44,27	1,30	34,78	79,02	87,03	38,29	2,54	0,96	2,84	80,60	33,51	76,16
AS 08V03	46,03	1,18	36,16	82,16	89,54	39,40	1,62	0,81	1,6	81,59	35,03	79,61
AL 09V02	50,95	0,91	40,03	90,95	95,10	41,84	1,07	0,21	0,56	91,54	39,67	90,16
AD 09V03	44,04	1,23	34,60	78,61	87,37	38,44	1,66	1,25	2,6	79,60	33,52	76,18
AS 10V03	47,28	1,11	37,15	84,40	90,40	39,78	1,78	0,7	1,49	85,57	36,66	83,32
AL 12V03	50,68	0,93	39,82	90,47	94,70	41,67	1,05	0,19	0,61	90,05	39,37	89,48
AD 13V02	45,06	1,21	35,40	80,43	88,07	38,75	2,03	0,93	2,03	81,09	34,43	78,25

<sup>1</sup>CARLO ERBA REAGENTI, calcium carbonate ACS-ISO-for analysis, CaCO<sub>3</sub>, minimum essay, 99,5 % – komplexometric.

<sup>2</sup>\*\* Preračunan na delež CaCO<sub>3</sub> (Calculated on w/% of CaCO<sub>3</sub>).

**Tabela 3:** Oksidna sestava mineralov, ki nastopajo v vezivu sedimentne kamnine-merjenca (<http://webmineral.com/>), določena z XRD-analizo  
**Table 3:** Total oxide composition (<http://webmineral.com/>) of minerals (detected by XRD analysis)

Mineral	Emperična formula Empirical formula	Oksidna sestava (w/%) Total oxide composition						
		CaO	Al <sub>2</sub> O <sub>3</sub>	SiO <sub>2</sub>	Fe <sub>2</sub> O <sub>3</sub>	K <sub>2</sub> O	Na <sub>2</sub> O	MgO
Klorit Chlorite	Na <sub>0,5</sub> Al <sub>4</sub> Mg <sub>2</sub> Si <sub>7</sub> AlO <sub>18</sub> (OH) <sub>12</sub> ·5(H <sub>2</sub> O)		26,18	43,19			1,59	8,28
Enstatit Enstatite	Mg <sub>2</sub> Si <sub>2</sub> O <sub>6</sub>			59,85			40,15	
Muskovit Muscovite	KAl <sub>3</sub> Si <sub>3</sub> O <sub>10</sub> (OH) <sub>1,8</sub> F <sub>0,2</sub>		38,36	45,21		11,81		4,07

**Slika 2:** Masni delež CO<sub>2</sub> glede na rezultate preiskovalnih metod (TGA-DTA in KB izmerjena, XRF in XRD preračunana na masni delež CaO oz. CaCO<sub>3</sub>)**Figure 2:** Amount of CO<sub>2</sub>, concording the results of mineralogical (XRD), chemical (XRF and "carbonate bomb") and thermal (TG-DTA) analysis

## 4 DISKUSIJA

Ob določitvi deleža karbonata s termično analizo je treba upoštevati obliko in položaj endotermnega vrha<sup>8</sup>, ki je odvisen od statičnega pritiska CO<sub>2</sub> na površini vzorca med procesom dekarbonatizacije. Razlika v procesu dekarbonatizacije se pokaže v tipu lokalne atmosfere, kjer poteka reakcija: če poteka proces v zraku – laboratorijski atmosferi, je temperatura razpada nižja kot pa v atmosferi CO<sub>2</sub>. Položaj endotermnega vrha je izpostavljen tudi nekaterim eksotermnim reakcijam kovinskih oksidov, ki nastanejo ob razpadu karbonata. Na obliko vrha imajo vpliv tudi soli ali Fe v magnezitu (nastanek breunnerita ((Mg,Fe)[CO<sub>3</sub>])) z atomskim razmerjem Mg : Fe od 90 : 10 do 70 : 30<sup>8</sup>), ki navidezno poviša maksimalno temperaturo, ki jo vrh krivulje doseže.

Iz pridobljenih rezultatov ugotavljamo, da CaO in MgO nista v celoti vezana v karbonatne minerale. TGA-analiza standarda kalcita kaže na 0,469-odstotno nenatančnost analize in kvantitativne določitve emisije CO<sub>2</sub>. Ob primerjavi natančnosti TGA-analize merjencev z XRF-analizo je v zadnji opaziti pribitek CaO, vezanega

na karbonat (kljub upoštevani natančnosti metode pri določitvi CaO), kar ponazarja **slika 3**.

Razliko v odmiku rezultatov XRF-TGA analize gre pripisati uporabi standarda pri določitvi CaO z XRF-metodo. Prav tako ima tudi TGA-metoda svoje pomajnike kljivosti pri določitvi karakteristične temperature razpada karbonata. Treba je namreč upoštevati prekrivanje endotermnih vrhov pri analizi polimineralnih merjencev različne kristaliničnosti, lastnosti, ki so vezane na nastanek karbonatnih mineralov sedimentnih kamnin (vpliv oblike osnovne celice na temperaturo razpada; **tabela 5**).

Tako sta deleža CaO in MgO (**tabela 4**) določena z XRF-metodo lahko vezana tudi na nekatere minerale glin (**tabela 6**).

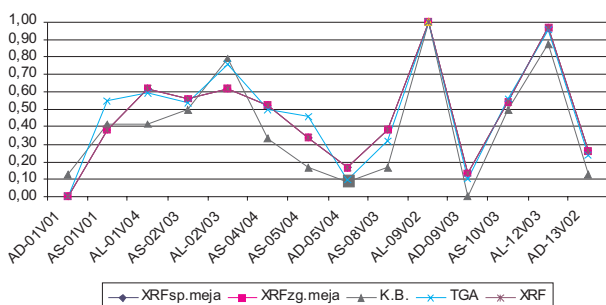
Delež MgO, ki ni vezan na enstatit in klorit (**tabela 4**), bi lahko bil vezan v karbonatih le:

- če bi bil s TGA- in XRD-analizo določen dolomit CaMg(CO<sub>3</sub>)<sub>2</sub>; kot monomineral vsebuje masni delež MgO do 21,86 %; dolomit je pokazatelj diagenetskih

**Tabela 4:** Masni delež MgO, ki ni vezan na karbonat**Table 4:** Amaount of MgO oxide which is not a part of carbonate minerals

MERJENEC SAMPLE	(w/%)						
	XRF			XRD		Δ <sup>3</sup>	
	CaO	MgO <sup>4</sup>	CO <sub>2</sub>	Enstatit Enstatite	Klorit Chlorite	MgO	
AD 01V01	42,97	1,36	33,76	3,27	3,06	-0,20	
AS 01V01	46,04	1,26	36,17	3,09	2,28	-0,17	
AL 01V04	47,92	1,10	37,65	1,72	1,31	0,30	
AS 02V03	47,44	1,11	37,26	2,15	1,32	0,14	
AL 02V03	47,90	1,09	37,63	2,47	1,45	-0,03	
AS 04V03	46,51	1,16	36,54	2,22	1,81	0,12	
AS 05V04	45,68	1,23	35,88	2,04	1,86	0,25	
AD 05V04	44,27	1,30	34,78	2,54	2,84	0,05	
AS 08V03	46,03	1,18	36,16	1,62	1,6	0,40	
AL 09V02	50,95	0,91	40,03	1,07	0,56	0,43	
AD 09V03	44,04	1,23	34,60	1,66	2,6	0,34	
AS 10V03	47,28	1,11	37,15	1,78	1,49	0,28	
AL 12V03	50,68	0,93	39,82	1,05	0,61	0,45	
AD 13V02	45,06	1,21	35,40	2,03	2,03	0,23	

<sup>3</sup>Delež prostega oksida, ki bi lahko bil vezan v obliku karbonata (Attributed to CaCO<sub>3</sub>).<sup>4</sup>Napaka meritve deleža MgO z XRF-analizo znaša 0,09 w/% (The error of MgO detection by XRF analysis is 0,09 w/%).



**Slika 3:** TGA-določitev  $\text{CaCO}_3$  v primerjavi z normiranimi rezultati (na ordinatni osi) XRF-analize

**Figure 3:** Results of TGA analysis compared with normalised XRF results

**Tabela 5:** Delitev karbonatnih mineralov glede na obliko osnovne celice in karakteristično temperaturo razpada<sup>8</sup>

**Table 5:** Distribution of carbonates according their crystallographic form and characteristic temperature<sup>8</sup>

SKUPINA KALCITA CACLITIC GROUP			SKUPINA DOLOMITA DOLOMitic GROUP			SKUPINA ARAGONITA ARAGONITIC GROUP		
Oblika osnovne celice heksagonalna Space group $R\bar{3}c$			Oblika osnovne celice heksagonalna Space group $R\bar{3}$			Oblika osnovne celice ortorombična Space group $Pm\bar{C}n$		
Mineral	emp. enačba Empirical formula	$T_{\text{karakteristična}}^{\circ}\text{C}$	mineral	emp. enačba Empirical formula	$T_{\text{karakteristična}}^{\circ}\text{C}$	mineral	emp. enačba Empirical formula	$T_{\text{karakteristična}}^{\circ}\text{C}$
Kalcit Calcite	$\text{CaCO}_3$	878,6 <sup>5</sup>	Dolomit Dolomite	$\text{CaMg}(\text{CO}_3)_2$	745	Aragonit Aragonite	$\text{CaCO}_3$	920
Magnezit Magnesite	$\text{MgCO}_3$	670	Ankerit Ankerite	$\text{Ca}(\text{Mg},\text{Fe})(\text{CO}_3)_2$	730	Viterit Witherite	$\text{BaCO}_3$	830
Rodohrozit Rhodochrosite	$\text{MnCO}_3$	610	Kutnohorit Kutnohorite	$\text{CaMn}(\text{CO}_3)_2$		Stroncianit Strontianite	$\text{SrCO}_3$	930

**Tabela 6:** Minerali glin, na katere je vezan delež  $\text{CaO}$  (<http://webmineral.com/>)

**Table 6:** Amount of  $\text{CaO}$  and  $\text{MgO}$  within some other minerals (<http://webmineral.com/>) which can be found in carbonate rocks

Mineral	Emperična formula Empirical formula	Oksidna sestava (w/%) Total oxide composition (w/%)						
		CaO	$\text{Al}_2\text{O}_3$	$\text{SiO}_2$	$\text{Fe}_2\text{O}_3$	$\text{K}_2\text{O}$	$\text{Na}_2\text{O}$	MgO
Odinit Odinite	$\text{Fe}^{3+}0,7\text{Mg}_{0,7}\text{Al}_{0,5}\text{Fe}^{2+}0,3\text{Ti}_{0,1}\text{Mn}^{2+}0,1\text{Si}_{1,8}\text{Al}_{0,2}\text{O}_5(\text{OH})_4$		11,87	35,98	18,59 <sup>6</sup>			9,39 <sup>7</sup>
Montmorillonit Montmorillonite	$\text{Na}_{0,2}\text{Ca}_{0,1}\text{Al}_2\text{Si}_4\text{O}_{10}(\text{OH})_2(\text{H}_2\text{O})_{10}$	1,02	18,57	43,77			1,13	
Volkonskoit Volkonskoite	$\text{Ca}_{0,1}\text{Mg}_{0,1}\text{Cr}_{1,2}\text{Mg}_{0,8}\text{Fe}^{3+}0,3\text{Si}_{3,5}\text{Al}_{0,5}\text{O}_{10}(\text{OH})_{2,3,6}(\text{H}_2\text{O})$	1,18	5,36	44,21	5,04			7,63
Swinefordite <sup>8</sup>	$\text{LiCa}_{0,5}\text{Na}_{0,1}\text{Al}_{1,5}\text{Mg}_{0,5}\text{Si}_3\text{O}_{10}(\text{OH})_{1,5}\text{F}_{0,5}\cdot2(\text{H}_2\text{O})$	7,06	19,25	45,38			0,78	5,07
Hidrobiotit Hydrobiotite	$\text{Mg}_{2,3}\text{Fe}^{3+}0,6\text{K}_{0,3}\text{Ca}_{0,1}\text{Si}_{2,8}\text{Al}_{1,2}\text{O}_{10}(\text{OH})_{1,8}\text{F}_{0,2}\cdot3(\text{H}_2\text{O})$	1,21	13,17	36,21	10,31	3,04		19,95
Illite	$\text{K}_{0,6}(\text{H}_3\text{O})_{0,4}\text{Al}_{1,3}\text{Mg}_{0,3}\text{Fe}^{2+}0,1\text{Si}_{3,5}\text{O}_{10}(\text{OH})_2\cdot(\text{H}_2\text{O})$		17,02	54,01	1,85 <sup>#</sup>	7,26		3,11
Vermikulit Vermiculite	$\text{Mg}_{1,8}\text{Fe}^{2+}0,9\text{Al}_{4,3}\text{SiO}_{10}(\text{OH})_2\cdot4(\text{H}_2\text{O})$		43,48	11,92	12,82 <sup>#</sup>			14,39
Bramalit Brammallite	$\text{Na}_{0,66}(\text{H}_3\text{O})_{0,33}\text{AlMg}_{0,6}\text{Fe}^{2+}0,1\text{Si}_3\text{AlO}_{10}(\text{OH})_2\cdot(\text{H}_2\text{O})$		26,02	46,00	1,83 <sup>#</sup>		5,22	6,17
								11,47

<sup>5</sup>Povprečna temperaturna izračunana na osnovi  $T_{\text{karakteristična}}$ , ki jo podaja Mackenzie<sup>8</sup>, (Averaged temperature after Mackenzie<sup>8</sup>).

<sup>6</sup>7,17 FeO

<sup>7</sup>2,36 MnO

<sup>8</sup> $\text{LiO}_2 = 3,76$ ,  $\text{F} = 2,39$

procesov, ki na območju Anhovega ob nastanku kamnin niso bili prisotni, velja pa omeniti, da lahko nastopa kot predstavnik starejših erodiranih in preloženih kamnin v sedimentacijsko okolje, kar bi v primeru merjenj pomenilo kvantitativno od 0,22 % do 2,08 % minerala; z opravljenou XRD-analizo, s katero lahko ločimo minerale z masnim deležem nad 1,0 %, ni bila dokazana prisotnost dolomita, prav tako ne za merjenec z 2,08 %;

2. če bi bil Mg vezan v obliko aragonita, ki je pri normalnih razmerah nestabilna-metastabilna mineralna faza in ga med procesom diageneze največkrat zamenja kalcit. V kamninah pelagične sedimentacije, ki so pokazatelj globalnih sprememb, so nosilci karbonata mikro- in kriptokristalne strukture<sup>16,17</sup> oz.

**Tabela 7:** Korelacija med rezultati, podanih s posamezno preiskovalno metodo**Table 7:** Results correlation between analysis research

	K, B,	TGA-DTA	XRD	XRF
K, B,	1			
TGA-DTA	0,9796655	1		
XRD	0,9385986	0,9393562	1	
XRF	0,8411661	0,8372388	0,8152043	1

fosilni planktonski organizmi in mikroorganizmi. Berner<sup>18</sup> navaja, da je najdba aragonita v globokomorskih sedimentih lahko posledica dolgega prenosa materiala iz plitvovodnega okolja ali pa posledica sedimentacije skeletov odmrlih planktonskih organizmov. Avtor prav tako navaja, da je karbonat z visoko vsebnostjo Mg izpostavljen raztopljanju zaradi vpliva  $p\text{CO}_2$ , raztopljenega v morju, kar potruje ob dodatnem vplivu kemizma morja (masno razmerje Mg/Ca) tudi Tucker<sup>19</sup>. V splošnem velja, da so vse karbonatne kamnine ne glede na njihovo prvotno mineralno sestavo, med diagenezo izpostavljene pretvorbi v kalcit z nizkim deležem Mg<sup>19</sup>. Aragonita v heterogenih sedimentnih kamninah, kot nastopajo v okolici Anhovega in so vezane na podoben nastanek, ni bilo mogoče ugotoviti, saj je njegov prvi endotermni vrh pri 447 °C, ki ponazarja diomorfn prehod aragonita v kalcit<sup>20</sup>. Ta temperatura sovpada z območjem endoternih reakcij mineralov glin. Kljub temu obstaja teoretična možnost pretvorbe kalcita v aragonit, vendar le pri tlakih 2,0 GPa in v temperaturnem območju 600 °C<sup>21</sup>, kar pa v primeru geoloških danosti Anhovega ne gre pričakovati.

Termični razpad karbonatnega minerala, ki sestavlja karbonatno sedimentno kamnino, je odvisen od njegove oblike in elementne sestave, ki so odsev njegovega nastanka (**tabela 5**). Iz rezultatov preiskav je razvidno, da poda termična analiza najbliže realne vrednosti karbonatnega deleža v surovini, saj sledi popolni emisiji CO<sub>2</sub> iz karbonata, ne glede na genezo nastanka kamnine. Vendar pa korelačijski faktor (**tabela 7**) potruje, da obstaja sprejemljiva soodvisnost tudi z analizo karbonatne bombe in XRD-analizo.

## 5 SKLEP

V prispevku je dokazana primerljivost med TGA-DTA-analizo in analizo s t. i., karbonatno bombo po Müller-Gastnerjevi metodi<sup>13</sup>. Iz dobrijih rezultatov lahko potrdimo, da masni delež MgO (do 0,27 % od prvotno ocenjenega na 1,13 %) ni popolnoma vezan na karbonatne minerale.

Ob sklepu je treba dodati, da detajlna mineraloška analiza veziva karbonatnih kamnin še ni bila izvedena. V tem pogledu bodo v prihodnje izvedene študije, ki bodo

ovrednotile masni delež CaO, ki ni vezan na karbonate v osnovni mineralni surovini za proizvodnjo OPC klinkerja.

## 6 LITERATURA

- <sup>1</sup> Wright, V. P. A revised classification of limestones, *Sed. Geol.*, 76 (1992), 177–186
- <sup>2</sup> Pogačnik, Ž. Reaktivnost karbonatnih kamnin in sekundarnih surovin-indikator okoljevarstva in trajnostnega razvoja v cementni industriji; Doctor's degree, Ljubljana: 2006, 124 str.
- <sup>3</sup> Portland, B. Geopolymer – the future? *International Cement review*, (2007), 79–82
- <sup>4</sup> Bucchi, R. Influence of the nature and preparation of raw materials on the reactivity of raw mix, V 7<sup>th</sup> International Congress on the Chemistry of Cement – Volume 1 Principal Reports, Pariz, 1980, 1–43
- <sup>5</sup> Fidaros, D. K., Baxevanou, C. A., Dritselis, C. D., Vlachos, N. S. Numerical modelling of flow and transport processes in a calciner for cement production, *Powder Technology*, 171 (2007) 2, 81–95
- <sup>6</sup> Géraldine, V., Mickaël, T., Gérard, P. Measurement methods of carbonation profiles in concrete: Thermogravimetry, chemical analysis and gammadensimetry, *Cement and Concrete Research*, 37 (2007), 1182–1192
- <sup>7</sup> Dunham, R. J. Classification of carbonate Rocks According To Depositional Texture. V Classification of Carbonate Rocks – a symposium, (1962), 108–122
- <sup>8</sup> Mackenzie, R. C. The differential thermal investigation of clays, London: Mineralogical society (clay minerals group), 1957, 456 str.
- <sup>9</sup> Oates, J. A. H., Lime And Limestones Chemistry And Technology, Production And Uses, Weinheim: Wiley-VCH, 1998, 455 str.
- <sup>10</sup> Taylor, H. F. W. *Cement Chemistry*, 2nd ed, Oxford : Thomas Telford, 1997, 439 str.
- <sup>11</sup> Meden, A. Poročilo o kvantitativni fazni analizi žlindre; specifična naloga, Ljubljana, 2005, 5 str.
- <sup>12</sup> Meden, A. Poročilo o kvantitativni fazni analizi surovin dostavljenih v marcu 2004; specifična naloga, Ljubljana, 2004, 29 str.
- <sup>13</sup> Müller, G., Gastner, M. The "Karbonat-Bombe", a simple device for the determination of the carbonate content in sediments, soils, and other materials: N, Jb, Mineral, Mh, 10 (1971), 466–469
- <sup>14</sup> Ramachandran, V. S., Phil, D. Applications of differential thermal analysis in Cement Chemistry, Chemical pulishing company, 1969, 308 str.
- <sup>15</sup> Yen, F. S., Lo, H. S., Wen, H. L., Yang, R. J.  $\theta$  – to  $\alpha$  – phase transformation subsystem induced by  $\alpha$  – Al<sub>2</sub>O<sub>3</sub> – seeding in boehmite – derived nano – sized alumina powders, *Journal of Crystal Growth*, 249 (2003), 283–293
- <sup>16</sup> Marschner, H. Relationship between carbonate grain and non-carbonate content in carbonate sedimentary rocks, In: Recent developments in carbonate sedimentology in Central Europe, Springer –Verlag, Editors: Müller, G., Frideman, G. M., New York, 1968, 55
- <sup>17</sup> Sprung, S. Effect of the Burning Process on the formation and properties of the clinker, V 7<sup>th</sup> International Congress on the Chemistry of Cement – Principal Reports, Pariz, 1 (1980), 44–60
- <sup>18</sup> Berner, R. A., Honjo, S. Pelagic Sedimentation of Aragonite: Its Geochemical Significance, *Science*, 11 (1981), 940–942
- <sup>19</sup> Tucker, M. E. *Sedimentary petrology*, 3rd ed, Blackwell Publishing company, 2005, 262 str.
- <sup>20</sup> Faust, G. T. Differentiation of Aragonite from Calcite by Differential Thermal Analysis, *Science*, 110 (1949), 402–403
- <sup>21</sup> Hacker, B. R., Kirby, S. H., Bohlen, S. R. Time and Metamorphic Petrology: Calcite to Aragonite Experiments, *Science*, 258 (1992), 110–112

## DEVELOPING AND TESTING A NEW TYPE-8K MOULD FOR TOOL-STEEL INGOT CASTING

### RAZVOJ IN PREIZKUS NOVE KOKILE VRSTE 8K ZA ULIVANJE INGOTOV IZ ORODNEGA JEKLA

**Martin Balcar<sup>1</sup>, Libor Sochor<sup>1</sup>, Rudolf Železný<sup>1</sup>, Pavel Fila<sup>1</sup>, Ludvík Martínek<sup>1</sup>,**  
**Libor Kraus<sup>2</sup>, Dušan Kešner<sup>2</sup>, Jiří Bažan<sup>3</sup>**

<sup>1</sup>ŽĎAS, a. s., Žďár nad Sázavou, Czech Republic

<sup>2</sup>COMTES FHT, s.r.o. Plzeň, Czech Republic

<sup>3</sup>VŠB TU – Ostrava, Czech Republic

martin.balcar@zdas.cz

*Prejem rokopisa – received: 2007-09-26; sprejem za objavo – accepted for publication: 2007-10-15*

The traditional production of machinery and tools at ŽĎAS, a. s., and the increasing requirements placed on the final product, particularly those related to the internal quality of forgings, requires new technological measures for the ingot's casting and solidification. The development and use of the new mould type 8K9.2 for tool-steel ingot casting has reduced the share of forgings with unacceptable quality. A substantial improvement has been achieved, especially in terms of the occurrence of defects, such as cavities and cracks in the ingot body.

Keywords: tool steel, mould, ingot casting, solidification, forging, ultrasonic testing

Tradicionalna proizvodnja strojev in orodij v podjetju ŽĎAS, a. s., in naraščajoče zahteve pri lastnostih končnega proizvoda, ki so povezane z notranjo kakovostjo izkovkov, so zahtevalo nove tehnološke ukrepe pri litju in strjevanju ingotov. Razvoj in uporaba nove kokile vrste 8K9.2 za litje jeklenih ingotov sta zmanjšala delež ingotov nesprejemljive kakovosti. Pomembno izboljšanje je bilo dosegeno pri pogostosti napak, razpok in votlin v notranjosti ingota.

Ključne besede: orodno jeklo, kokila, ulivanje ingotov, strjevanje, kovanje, ultrazvočna preiskava

### 1 INTRODUCTION

The determination of the causes of the internal defects in tool-steel ingots and forgings leads to the implementation of optimisation measures in production technology <sup>1,2</sup>. The requirements for the internal quality of forgings from large blocks, and the conditions for forming in the company ŽĎAS, a. s., represented by the limit of the pressing force, has focused work on the processes of ingot casting and solidification related to ingot-mould shape changes. An optimised form of the ingot 8K9.2 with a mass of 8.9 t, and with a reduced portion of axial defects defined in particular by the Niyama criterion <sup>3</sup> was proposed after a numerical simulation of the casting process and solidification of the forging ingot 8K8.4 with a mass of 7.6 t by applying MAGMA software.

With the use of the new shaped mould 8K9.2 for the casting of tool steel W.Nr. 1.2344 (X40CrMoV51) in ingots with a mass of 8.9 t, the internal quality of the ingots was improved. Ingots with a low share of the poor integrity in the axial part are the basic pre-requisite for the high-quality production of large tool-steel forgings.

### 2 DEFECTS IN INGOTS MADE OF TOOL STEEL

In the company ŽĎAS, a. s. the production of tools is carried out by processing the 8K ingots with masses of

1000 kg to 11700 kg on CKV 630, CKV 1250 and CKV 1800 presses. In 2006 the forming force for the CKV 1800 press was increased from 18 MN to the current value of 22.5 MN.

The traditional assortment of tool steels consists of, e.g., the steel grades **90MnCrV8**, X37CrMoV51, **X40CrMoV51**, 55NiCrMoV7, X210Cr12 and special steels for the rolls in rolling mills: 8CrMoV, **8Cr3MoSiV**, 8CrMoSiV.

When producing forgings from tool steel, the problems are connected with the low plastic properties related to the high content of carbon in combination with the content of the alloying elements, chromium, molybdenum and vanadium. Sufficient forging through the ingot and the elimination of internal defects, particularly in the zone of the end of solidification, in the axial part of the ingot, requires a high degree of forming and a sufficient deformation volume.

In the case of large forgings with a diameter that make it impossible to achieve the necessary deformation in the axial part of the ingot by forging, the required internal quality is obtained with an improvement of the ingot's internal quality.

### 3 VERIFICATION OF THE INGOT 8K9.2

The design of the new mould shape is based on an analysis of numerous modifications to the mould

geometry ensuing from the existing polygonal ingot of the type 8K8.4 with a mass of 7600 kg.

The main changes to the geometry were made from the viewpoint of slenderness and the bevel of the ingot body. The final shape was, afterwards, adapted and verified with modelling of the ingot 8K9.2 with a mass of 8850 kg. A comparison of the basic parameters of the ingot 8K8.4 and the design of the new shape of the ingot 8K9.2 are given in **Table 1**.

**Table 1:** Basic parameters of the ingot 8K8.4 and the design of the ingot 8K9.2

**Tabela 1:** Osnovni parametri ogljika 8k8.4 in načrt ogljaka 8K9.2

Type	Mass and volume					$S$ slen- derness	$V$ taper	
	ingot	head		body				
		kg	kg	%	kg	%		
8K8.4	7 600	800	11%	6 800	89%	2.1	4.8	
8K9.2	8 850	1 200	14%	7 650	86%	1.3	11.0	

The steel **X40CrMoV51** was chosen for the verification of the quality of the ingots and the forgings. Two heats were cast into two ingots, 8K8.4 and 8K9.2, each. One ingot from the heat was always submitted for analyses of the chemical composition from the viewpoint of segregations and structural heterogeneities, while the second ingot was processed by forming on the CKV 1800 press to produce a bar with a diameter of 350 mm with the maximum use of material, i.e., without the technological waste associated with the technology of open-die forging.

### 3.1 Chemical heterogeneity of the ingot

For a comparison of the chemical heterogeneity of the ingots made from the steel grade **X40CrMoV51** the chemical composition of the ingots of the types 8K8.4 and 8K9.2 was determined on a cross-section in the longitudinal direction according to the layout shown in

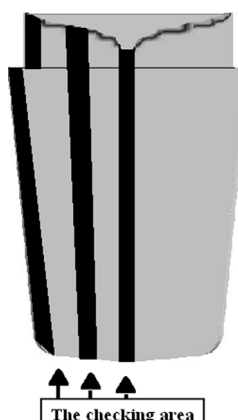


**Figure 1:** Layout of samples for analyses of the chemical composition  
**Slika 1:** Položaj izreza vzorcev za kemijsko analizo

**Figure 1.** The results of these analyses were compared to the results of heat analyses, and on the basis of the differences, positive and negative values of the absolute differences of the individual elements were determined.

The diagrams in **Figure 2** and **Figure 3** show the positions of the greatest differences in the carbon concentration, i.e., in the axis along the height of the ingot of types 8K8.4 or 8K9.2. **Figure 4** shows the changes in the concentration of sulphur in the axis along the height of the ingot of type 8K8.4 and then along the height of the ingot of type 8K9.2.

**Figure 6** and **Figure 7** show the deviations of the molybdenum concentration from the heat analysis in the axis along the height of the ingot type 8K8.4 or 8K9.2.

From the absolute deviations of the elements determined from the samples of steel taken during the casting of ingots it is obvious that with the solidification of steel in the mould 8K9.2 a more distinct segregation of carbon, sulphur and molybdenum occurs along the ingot axis in comparison to the mould 8K8.4.

In **Figure 8** it is possible to compare the differences in the segregation of elements at the surface, at a distance of  $\frac{1}{2}$  of the radius from the surface (middle radius), and in the axis of the ingot 8K9.2. The higher content of carbon at the ingot surface is probably related to the used casting powder, which contains the mass fraction of C up to 21 %. At the place marked as  $\frac{1}{2}$  of the radius (middle radius) and also in the ingot axis, at the foot part the carbon is being negatively segregated and at the top part a positive segregation occurs, whereas the

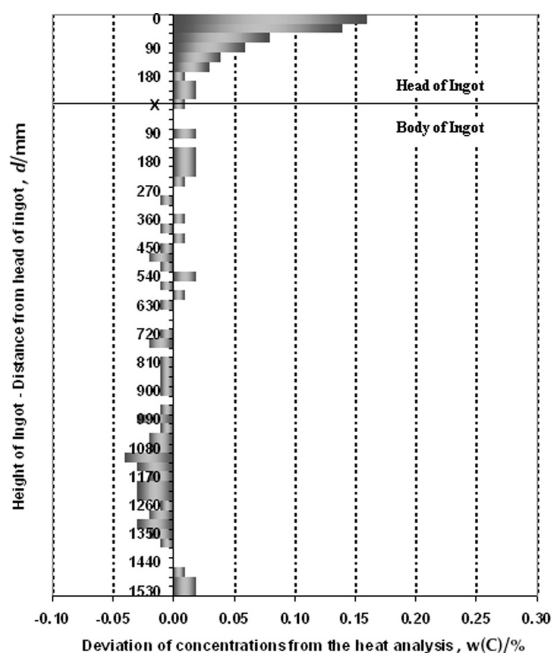


**Figure 2:** 8K8.4 – deviations of carbon concentration from the heat analysis (0.38 wt. % C) along the ingot axis

**Slika 2:** 8K8.4 – odmik pri vsebnosti ogljika od analize taline v masnih deležih ( $w(C) = 0.38 \%$ ) vzdolž osi ingota

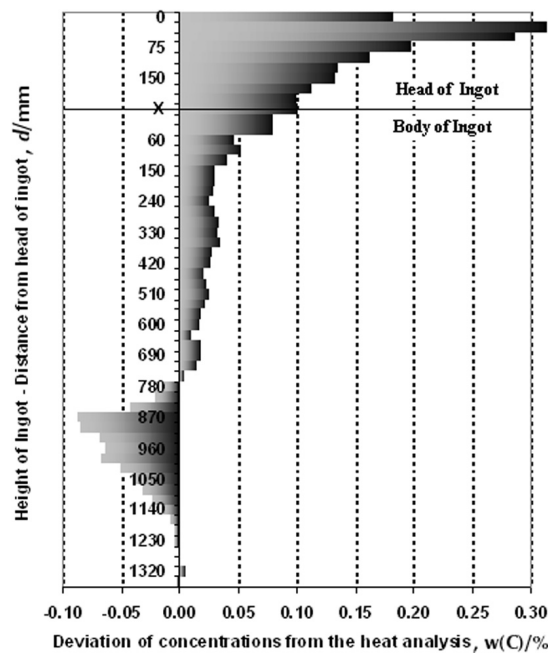


**Figure 3:** 8K9.2 – deviations of carbon concentration from the heat analysis (0.38 wt. % C) along the ingot axis

**Slika 3:** 8K9.2 – odmik pri vsebnosti ogljika od analize taline v masnih deležih ( $w(C) = 0.38 \%$ ) vzdolž osi ingota

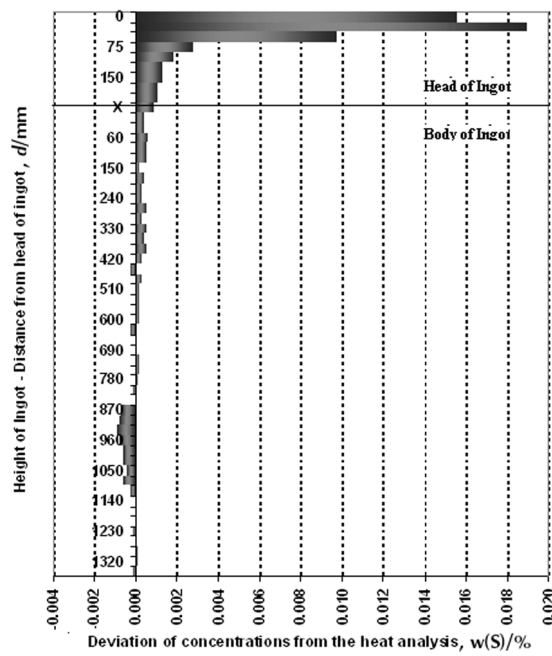


**Figure 5:** 8K9.2 – deviations of sulphur concentration from the heat analysis (0.0035 wt. % S) along the ingot axis

**Slika 5:** 8K9.2 – odmik pri vsebnosti žvepla od analize taline v masnih deležih ( $w(S) = 0.0035 \%$ ) vzdolž osi ingota

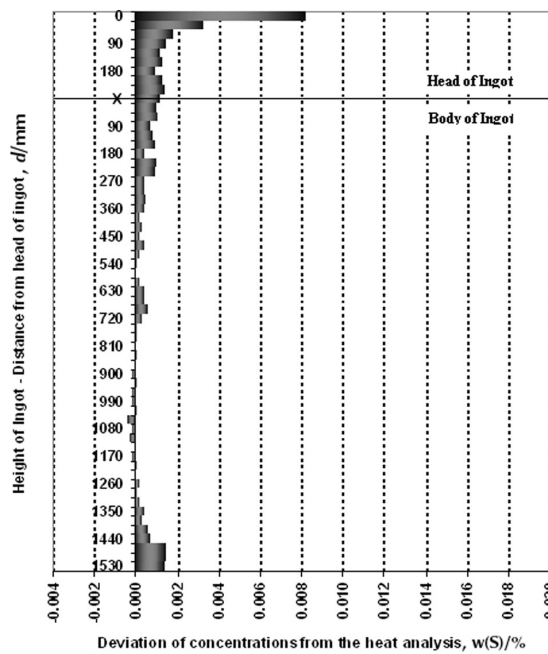


**Figure 4:** 8K8.4 – deviations of sulphur concentration from the heat analysis (0.0060 wt. % S) along the ingot axis

**Slika 4:** 8K8.4 – odmik pri vsebnosti žvepla od analize taline v masnih deležih ( $w(S) = 0.006 \%$ ) vzdolž osi ingota

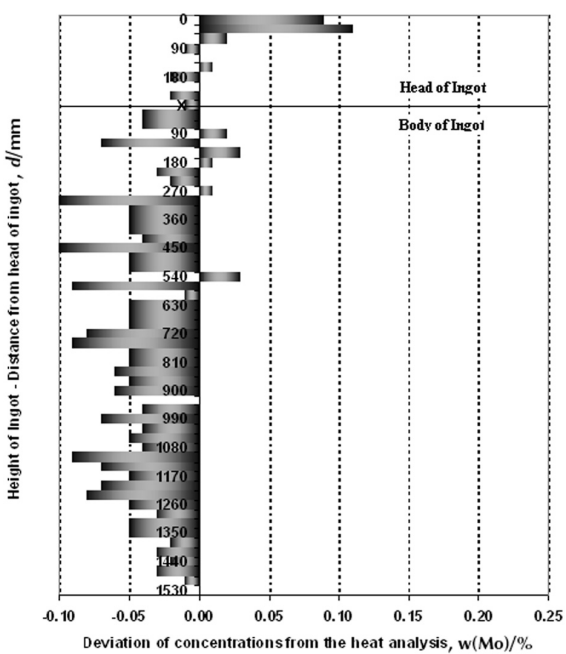


**Figure 6:** 8K8.4 – deviations of the molybdenum concentration from the heat analysis (1.25 wt. % Mo) along the ingot axis

**Slika 6:** 8K8.4 – odmik pri vsebnosti molibdena od analize taline v masnih deležih ( $w(Mo) = 1.25 \%$ ) vzdolž osi ingota

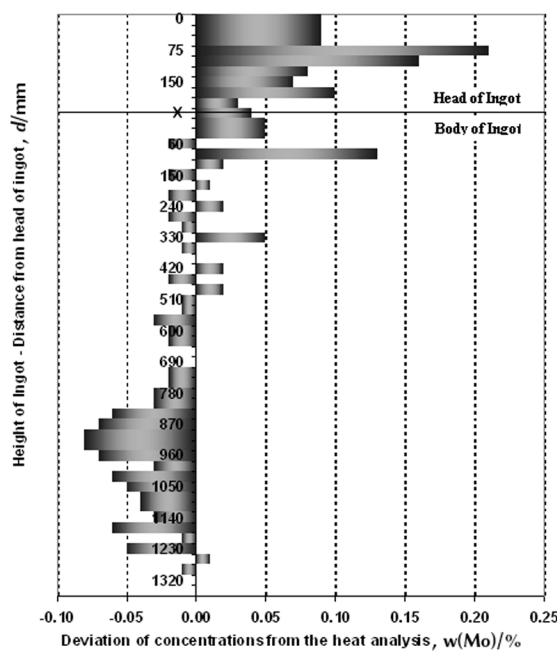


**Figure 7:** 8K9.2 – deviations of the molybdenum concentration from the heat analysis (1.25 wt. % Mo) along the ingot axis

**Slika 7:** 8K9.2 odmik pri vsebnosti molibdena od analize taline v masnih deležih ( $w(\text{Mo}) = 1.25 \%$ ) vzdolž osi ingota

axial part of the ingot is characterised by greater differences in the concentrations.

It is possible to verify the results of the numerical simulation using the MAGMA software with a comparison of the curve in **Figure 8** with the curve in **Figure 9**. It is evident that in real conditions more distinct differences occur from the viewpoint of the absolute change of the carbon concentration. The numerical simulation also does not take into account the possibility of carburisation of the melt by carbon pick up from external sources. The contribution of the numerical simulation is apparent in the area of the determination of

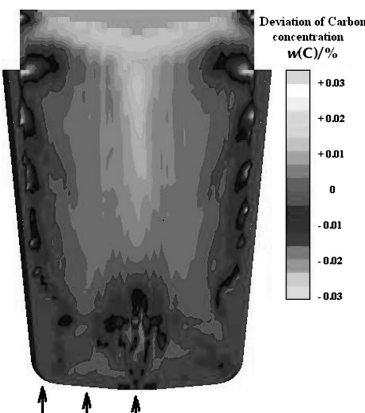


**Figure 9:** 8K9.2 – MAGMA deviations of carbon concentrations along the height of the ingot body

**Slika 9:** 8K9.2 – MAGMA odmik pri vsebnosti ogljika po višini ingota

the distribution of positive and negative segregations on the ingot's cross-section.

### 3.2 Structural defects of ingots

Real forgings were investigated for a practical verification of the spread of internal defects. The following ingots were cast from the steel X40CrMoV51:

- ingot 8K8.4 – **bottom casting**
- ingot 8K8.4 – **top casting**
- ingot 8K9.2 – **bottom casting**

After cutting the ingots and completing a capillary test by wet testing, the pictures that were taken were changed to a graphical transformation with the aim to accentuate the ingot defects. The obtained appearance of an internal part of the ingot in cross-section is shown in **Figure 10** to **Figure 12**.

The pictures confirm the influence of the casting technology and the shape of the mould on the spread of internal defects. A more detailed investigation of the size

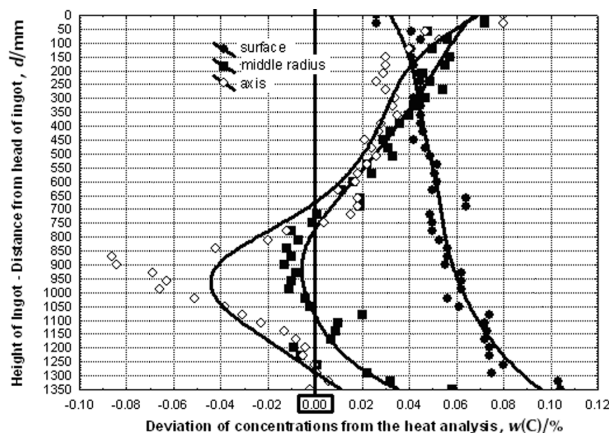


**Figure 8:** 8K9.2 – deviations of carbon concentration from the heat analysis (0.38 weight % C) along the height of the ingot body

**Slika 8:** 8K9.2 – odmik pri vsebnosti ogljika od analize taline v masnih deležih ( $w(\text{C}) = 0.38 \%$ ) po višini ingota

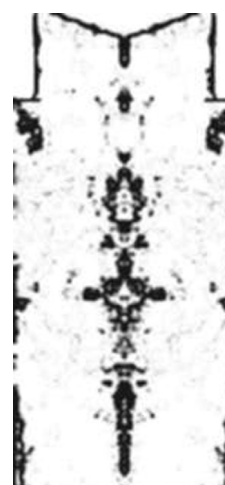


**Figure 10:** 8K8.4 bottom cast ingot – ingot defects

**Slika 10:** 8K8.4 ingot ulit od spodaj – napake v ingotu



**Figure 11:** 8K8.4 top cast ingot – ingot defects  
**Slika 11:** 8K8.4 ingot ulit od zgora – napake v ingotu



**Figure 12:** 8K9.2 bottom cast ingot – ingot defects  
**Slika 12:** 8K9.2 ingot ulit od spodaj – napake v ingotu

of individual defects shows that the ingot 8K9.2 contains cracks that are 1 mm wide and with a length up to 10 mm, while the ingot 8K8.4 contains along the ingot axis – regardless of the casting technology – continuous cracks and voids with widths above 5 mm and lengths up to several centimetres, in some cases.

### 3.3 Results of ultrasonically testing the forging

The main part of the evaluation of the influence of changes of the mould shape on the production of forgings made from tool steels were tests of the internal quality of forgings with ultrasonics in accordance with the standard **SEP 1921**. The verification of the quality of the experimental forging from the ingot 8K9.2 of steel **X40CrMoV51** was performed according to the degrees

A/a, B/b, C/c, D/d, E/e, with the level **D/d** or possibly **E/e**, considered as acceptable for the given steel.

On the basis of measurements and from the comparison of the results of the statistical evaluation of the previous production of forgings from the steel grade X40CrMoV51, summarised in **Table 2**, it is evident that a change in the mould shape brought a significant increase in the utilisation of the ingot, as well as an enhancement of the forging's internal quality.

**Table 2:** Utilisation of ingots of steel X40CrMoV51 – ultrasonic testing according to the SEP 1921

**Tabela 2:** Uporaba ingotov iz jekla X40CrMoV51 – ultrazvočna kontrola po SEP 1921

Type	Mass kg	Guaranteed US	Ingot utilisation	
			kg	%
8K8.4	7600	B/b	5950	78%
		C/c	5450	72%
		D/d	4600	61%
		E/e	0	0%
8K9.2	8850	E/e	7300	82%

The test bar forged from the ingot 8K9.2 satisfied the requirements of all the degrees of ultrasonic tests and the length of the bar corresponded to 82 % of the utilisation of the ingot's volume. The remaining material in the forging could not be used due to cracks in the ingot's head and footing crop end due to material flow and the necessity of aligning the forging's front face with machine cutting.

The optimistic conclusions based on an investigation of one forging were confirmed by the results obtained on real forgings of bars and blocks from tool steels with a mass up to 7 t and a bar diameter up to 600 mm, or the height of a block up to 500 mm.

## 4 CONCLUSIONS

The verification of the results of a numerical simulation with examinations on real ingots confirms the influence of changes of the mould geometry on the segregation in the ingot. The degree of chemical heterogeneity of the ingot also depends a great deal on the type of cast steel.

The change of the casting technology did not decrease the quantity of defects, such as cracks and voids, along the axial part of the ingot to an acceptable level. Important changes in the distribution and shape of the internal defects of the ingot were noted in ingots cast into the new shapes of the moulds of the type 8K9.2.

On the basis of the results of the investigation it was possible to obtain a substantial enhancement of the internal quality of the forgings with a simultaneous reduction in the share of unsatisfactory forgings that did not pass the ultrasonic testing, as a consequence of the change in geometry of the forging ingot of the type 8K9.2 with a mass of 8.9 t.

*The investigations were performed within the TANDEM program of the FT\_TA/061 project. The project was funded partially with the financial support of the Ministry of Industry and Trade of the Czech Republic.*

## 5 LITERATURE

<sup>1</sup> Martínek, L., Balcar, M., Novák, J., Sochor, L.: Analysis of internal non-integrities of the ingot made of tool steel, 6<sup>th</sup> International metallurgical symposium, Rájecké Teplice, 2003

<sup>2</sup> Martínek, L., Balcar, M., Novák, J., Sochor, L.: Internal structure of the ingot made of tool steel, 20<sup>th</sup> conference Theory and practice of making and processing of steel, Rožnov, Tanger, 2003

<sup>3</sup> Carlson, K. D., Shouzhu OU, Hardin, R., Beckerman, CH.: Development of new feeding – distance rules using casting simulation: Part I. Methodology.

<sup>4</sup> <http://www.engineering.uiowa.edu/čbecker/documents.dir/FeedingPart1.pdf>

## AN AES INVESTIGATION OF BRUSHED AISI 304 STAINLESS STEEL AFTER CORROSION TESTING

### AES-PREISKAVE KRTAČENEGA NERJAVNEGA JEKLA AISI 304 PO KOROZIJSKEM PRESKUSU

**Matjaž Torkar, Djordje Mandrino, Martin Lamut**

Institute of Metals and Technology, Lepi pot 11, 1000 Ljubljana, Slovenia  
matjaz.torkar@imt.si

*Prejem rokopisa – received: 2007-07-19; sprejem za objavo – accepted for publication: 2007-11-16*

During a test in a wet salt (NaCl) chamber rusty spots and elongated pits appeared on the brushed surface of a prototype casing for a household device made from AISI 304 stainless steel. The corrosion pits only formed on the brushed surface and on the deformed edges. Metallography revealed deformation-induced martensite and delta ferrite in the microstructure. In the wet salt environment the brushed surface showed a lower corrosion resistance than the non-brushed surface. The corrosion was explained as being due to damage to the protective oxide layer with brushing, insufficient re-passivation and the presence of iron particles. The corrosion propensity of the brushed surface of the casing was increased by the presence of deformation-induced martensite, delta ferrite and, probably, the remains of iron particles. The use of AISI 316 stainless steel, alloyed with molybdenum, would be more appropriate for avoiding the formation of corrosion pits due to chloride ions in a wet environment.

**Key words:** stainless steel, pitting corrosion, passivation, deformation-induced martensite, AES analysis

Obišče prototipne gospodinjske naprave je bilo izdelano iz nerjavnega jekla AISI 304. Iz dekorativnih razlogov je bila površina krtičena. Med preskusom vlažni slani komori se je pojavila korozija v obliki rjastih madežev in podolgovatih jamic vzdolž zakriviljenega roba. Predstavljeni so rezultati metalografske preiskave in analiza korozijskih produktov. Korozijске jamicice se opazi samo na predhodno krtičeni površini in po deformiranih robovih. Z metalografskimi preiskavami smo odkrili v mikrostrukturi po deformiranih robovih prisotnost deformacijskega martenzita in delta ferita. V vlažnem slanem (NaCl) okolju je krtičena površina pokazala slabšo korozijsko odpornost v primerjavi z neobdelano površino. Glavna razloga za korozijo sta med krtičenjem poškodovan oksidni sloj in slaba repasivacija po krtičenju. Dodatno so lahko k pojavi korozije prispevali še deformacijski martenzit, delta ferit in ostanki delcev železa na površini. Posledica slabše korozijskih odpornosti je pojav jamičaste korozije v vlažnem, slanem okolju. Za zmanjšanje možnosti pojava jamičaste korozije bi bila bolj primerena izbira nerjavnega jekla AISI 316, ki je legirano z molibdenom in s tem bolj odporno proti pojavi jamičaste korozije.

**Ključne besede:** nerjavno jeklo, jamičasta korozija, pasivacija, deformacijski martenzit, AES analiza

## 1 INTRODUCTION

The passive film on a stainless-steel surface consists of a mix of iron oxide and chromium oxide. The chromium oxide film is formed instantaneously in the air, if the stainless steel surface is clean and dry. However, complete passivation cannot be achieved if the product-contact surfaces are not clean or they contain surface defects. The polishing of the stainless steel's surface, therefore, improves the corrosion resistance<sup>1</sup>. The resistance to pitting corrosion is also increased by alloying the stainless steel with molybdenum. The beneficial effect of molybdenum on the corrosion resistance of stainless steels is widely recognized<sup>2,3,4</sup> and has been attributed to several factors<sup>4</sup>, such as: the enrichment of Cr in the oxide layer; the enrichment of Mo in the passive film or in the alloy layer just below the passive film; the thickening of the passive film; and the stabilisation of the Cr oxides by the presence of six-valence Mo<sup>5</sup>.

The interaction between the different oxides and the passivation/corrosion characteristics of stainless steel are very complicated and not yet fully understood.

Different surfacing techniques are applied to stainless steel to obtain a special visual effect on the surface. The brushing of stainless steel's surface is popular because it gives an attractive look to the surface. The protection from contamination of the steel surface requires the brushing of the stainless steel to be with stainless-steel brushes. In the event that iron particles on the stainless-steel surface are not removed by cleaning or by passivation in acid, subsequent pitting corrosion usually appears in a wet environment<sup>6</sup>.

An additional influence on the corrosion resistance of the material comes from different constituents of the microstructure, like carbides, martensite, delta ferrite and inclusions. Also well known is the harmful influence of deformation-induced martensite<sup>7,8</sup>, which forms during the cold working of stainless steel. After cold working the stainless steel needs to be annealed at 1050 °C in order to transform the martensite to austenite. Furthermore, residual stresses in the material can induce stress-corrosion cracking and accelerate the appearance of other corrosion forms when the material is exposed to a corrosive environment. Pitting corrosion due to chloride ions can cause considerable damage to the steel

surface; it penetrates deep into the material and causes local weak points or even perforations of the wall.

The process of pitting corrosion is well defined, but frequently the reasons for its starting are not clearly defined. The pit can form only in places where the passive layer is interrupted. The well-known standard work on corrosion<sup>8</sup> states that pits form more readily on etched or ground surfaces than on a polished surface, and the presence of cold working can increase the propensity to pitting.

The corrosion resistance of stainless steel also depends on the amount of carbon in the steel. The precipitation of carbides depletes the neighbourhood of chromium and accelerates the intercrystalline and pitting corrosion. Besides martensite and the presence of iron particles, the corrosion is also accelerated by delta ferrite and sulphide inclusions.

When the pits start to grow, the corrosion process diminishes the pH in the pit bottom and chloride ions move towards the pit. This accelerates the pit growth in terms of depth, which can lead to the perforation of the sheet and a leak in the wall or the failure of the structure. For these reasons, many factors should be considered for the selection of suitable stainless steel. The investigated stainless steel showed failures typical for pitting corrosion.

The aim of the investigation was to analyse the corrosion residue on the stainless steel's surfaces and to identify the main reasons for the corrosion.

## 2 EXPERIMENTAL

The investigated samples were from a corrosion-tested AISI 304 stainless-steel casing with a previously brushed surface. The composition of the investigated steel is listed in **Table 1**.

The corroded surface of the casing was carefully visually and macroscopically surveyed and typical corroded samples were cut for a metallographic investigation and for an AES analysis. The samples for metallographic observation were prepared by the standard procedure and etched in aqua regia. The microstructure was investigated with an optical microscope, the surface defects were observed with a stereo microscope and in a scanning electron microscope. The corrosion products were analysed by Auger spectroscopy (AES). Before the AES analysis, the surface was cleaned for 45 min with ion etching. For the AES analysis an electron source of Mg Ka (1253.6 eV) was used, and the results were compared with the

reference database of binding energies<sup>9</sup> accessible at the URL: <http://srdata.nist.gov/xps/>.

## 3 RESULTS AND DISCUSSION

A careful visual and stereo-microscope examination revealed spots of rust, white remnants identified as sodium chloride (**Figure 1**) and corrosion pits on the surface of the case. After the corrosion test a difference was observed when comparing the brushed (**Figure 2**) and non-brushed surface (**Figure 3**) of the case. The corrosion pits were only observed on the brushed surface, while the non-brushed surface was without any corrosion damage.

The rusty spots in **Figure 1** represent the remains of dried rust and were easily removed from the non-brushed surface. Most of the surface below the rusty spots was without any corrosion damage. The possible sources of rust were cut edges, holes for screws and deformed regions where the sheet was bent. It is also important not to neglect the remnants of other material that was in contact with the sheet, like for instance, fragments of the brush. It seems that a liquid, contaminated with rust, was spread over the sheet, and after drying the rust spots remained on the non-corroded steel surface.

SEM microscopy of the brushed surface revealed individual corrosion pits and groups of corrosion pits (**Figure 2**). The longitudinal traces of brushing are evident on one side of the sheet, while the opposite side

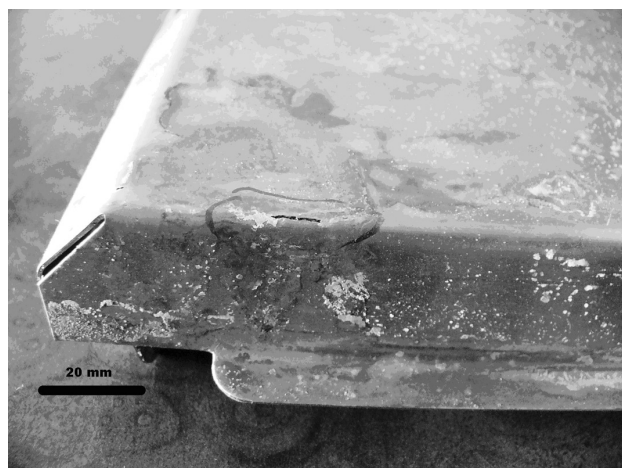


**Figure 1:** Remains of rust and NaCl on the surface of AISI 304 stainless steel after a corrosion test in wet salt chamber. The longitudinal pit is present on the bent edge

**Slika 1:** Ostanki rje in NaCl na površini AISI 304 nerjavnega jekla po koroziskem preskusu v vlažni slani komori. Na upognjenem robu se opazi vzdolžno jamičasto izjedo

**Table 1:** Chemical composition of the AISI 304 steel

**Tabela 1:** Kemična sestava jekla AISI 304

Composition	Element in mass fractions wt/%								
	C	Si	Mn	Cr	Ni	Mo	N	Cu	S
AISI 304	0.053	0.48	1.42	17.4	8.3	0.39	0.04	0.14	0.024

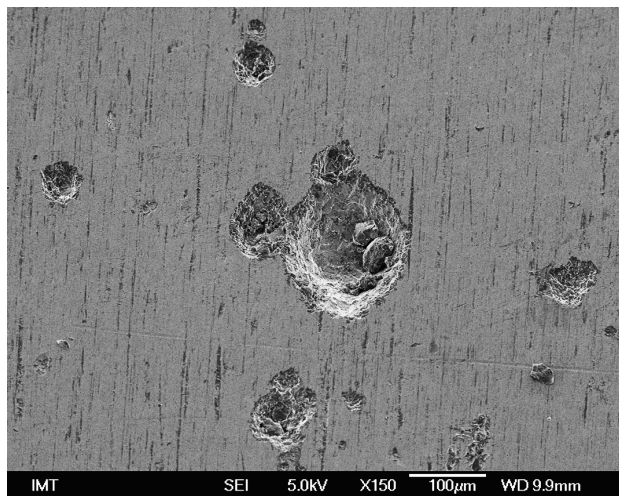


**Figure 2:** Corrosion pits on the brushed surface after the corrosion test. SEM

**Slika 2:** Jamičasta korozija na krtačeni površini po koroziskem preskusu. SEM

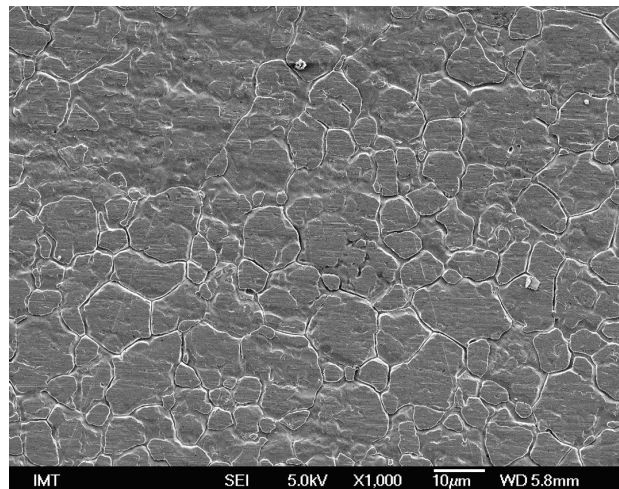


**Figure 3:** Untreated surface after the corrosion test. SEM

**Slika 3:** Neobdelana površina po koroziskem preskusu. SEM

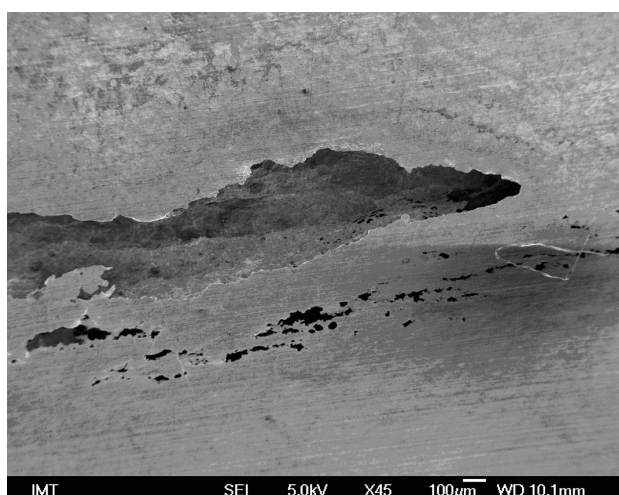


**Figure 4:** Longitudinal corrosion pit on the bent edge. SEM

**Slika 4:** Vzdolžne koroziske jamice na upognjenem robu. SEM

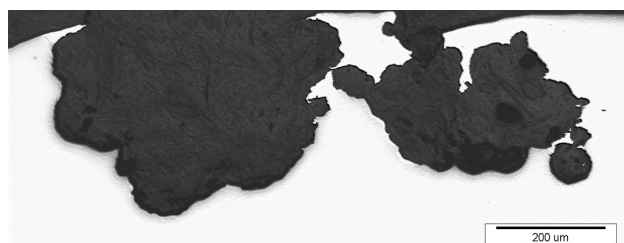


**Figure 5:** Micrograph of cross-section of the corrosion pit on the bent edge. Local corrosion advanced deep into the material of the case wall

**Slika 5:** Posnetek preseka koroziskske jamice na upognjenem robu.

Lokalno je korozija prodrla globoko v material stene ohišja

of the sheet and the non-brushed surface revealed equiaxed grains with clearly defined grain boundaries (**Figure 3**). Only the brushed surface and the bent edge of the sheet were damaged by corrosion, and on the curved edge longitudinal pits were observed (**Figure 4**). In corrosion-damaged regions we observed either the aggregation of shallow pits or individual deep pits (**Figures 2 and 5**).

The metallography revealed martensite in the deformed regions in the austenitic matrix. Also, elongated delta ferrite (**Figure 6**) was present in the matrix. Both phases were a possible source of the corrosion, when in contact with the corrosion medium.

Because of the wet environment and the presence of chloride ions in the salt chamber, the local pitting corrosion process started and advanced to the middle of the sheet, as revealed by the optical microscopy in the cross-section (**Figure 5**). The corrosion process was also accelerated by the presence of deformation-induced martensite. To transform the martensite into austenite, it is necessary to anneal the stainless steel after cold deformation.

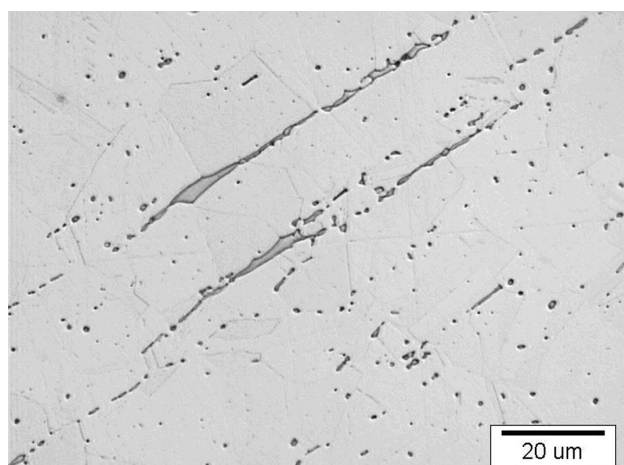


**Figure 6:** Microstructure of austenitic stainless steel AISI 304 with elongated delta ferrite. In deformed regions the deformation-induced martensite was also present. Etched with aqua regia.

**Slika 6:** Mikrostruktura avstenitnega nerjavnega jekla AISI 304 z razpotegnj enim delta feritom. V deformiranih področjih je bil prisoten tudi deformacijski martenzit. Jedkano v zlatotopki.

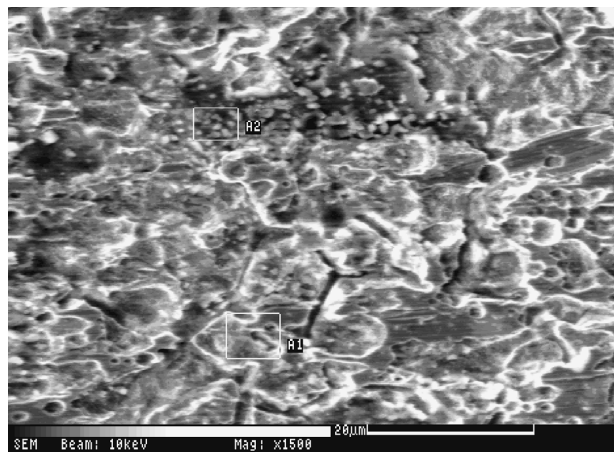


**Figure 7:** Surface damaged by corrosion (SEM). A1 and A2 mark the areas analysed with AES. Before the analyses the surface was ion etched for 45 minutes.

**Slika 7:** Površina poškodovana s korozijo (SEM). A1 in A2 sta področji, ki sta bili analizirani z AES. Pred analizo je bila površina 45 minut ionsko jedkana.

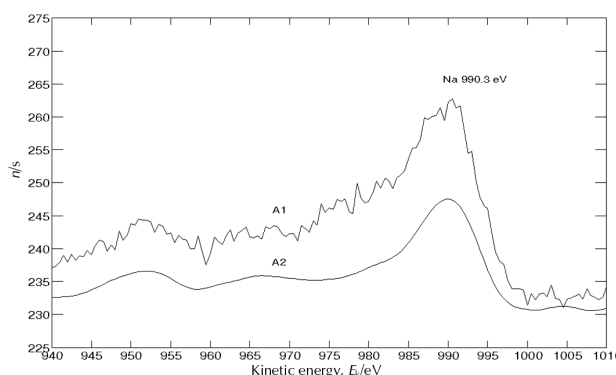


**Figure 8:** AES spectrum on the corroded places A1 and A2 marked in **Figure 7**. Presented peak for Na KLL at 990.3 eV in non-differentiated spectrum of AES corresponds to Na in NaCl<sup>9</sup>

**Slika 8:** AES-spekter na področjih korozije A1 in A2 označenih na sliki 7. Predstavljen vrh za Na KLL pri 990,3 eV v nediferenciranem spektru AES ustreza Na v NaCl<sup>9</sup>

The AES analysis of the corroded steel surface (**Figures 7 and 9**) after the wet salt chamber test revealed that in the corrosion pits either sodium and chlorine or only chlorine were present (**Figure 8 and 10**). The binding energy of the analyzed element sodium corresponded to NaCl (**Figure 8**). The source of the NaCl was the wet salt chamber. No traces of sodium or chlorine were detected on the non-corroded surface (**Figure 10, P2**). But in typical use a possible source of chloride ions is from the environment (sprayed brine, the salt in food, cleaners).

The investigation of the prototype case for use in domestic and outdoor activities, e.g., a barbecue, revealed several deficiencies. The AISI 304 stainless steel is less appropriate for a wet environment where chloride ions are present. The brushing of the surface, due to aesthetic reasons, damaged the passive film on the



**Figure 9:** Surface with corrosion pit. At the points P1 and P2 the AES analyses were performed. The presence of Cl was detected only in the pit. SEM

**Slika 9:** Površina z jamičasto korozijo. Točki P1 in P2 sta bili analizirani z AES. Samo v jamici je bil prisoten Cl

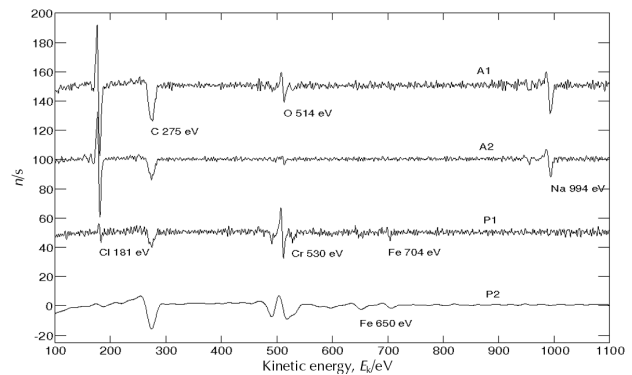


**Figure 10:** AES spectrum in the areas A1 and A2 (**Figure 7**), and at the points P1 and P2 (**Figure 9**). Only in the corroded areas A1 and A2 was the presence of Na and Cl detected. In the pit P1 only Cl was detected. Out of the pit no Na or Cl was detected.

**Slika 10:** AES spekter s področja A1, A2 (slika 7) in v točkah P1, P2 (slika 9). Samo na korodiranih področjih A1 in A2 je bila odkrita prisotnost Na in Cl, v jamici P1 pa samo prisotnost klorja. Izven jamicje ni bilo Na ali Cl.

steel's surface. A possible accelerator of the corrosion was the presence of deformation-induced martensite and delta ferrite in the microstructure of the steel, as well as unremoved iron particles on the steel's surface.

#### 4 CONCLUSIONS

The corrosion test in the wet salt chamber revealed that the brushed surface was sensitive to pitting corrosion, but the unbrushed surface was corrosion resistant. From this we concluded that the corrosion of the prototype stainless-steel casing is very probably due to the smoothing that damaged the passive layer on the steel's surface. The re-passivation was too weak and the pitting corrosion appeared during the corrosion test due to the presence of iron particles and chloride ions in the

wet environment. The appearance of pitting corrosion is also to be expected during use.

The investigation of the prototype casing revealed that the wrong type of stainless steel had been selected for the proposed application.

Compared to AISI 304 the AISI 316 stainless steel should be more suited to the application in a wet environment where chloride ions are also present. Alloying with 2–3 wt% of molybdenum reduces the sensitivity of the steel to pitting corrosion.

It is also advisable to passivate the surface of the stainless steel with diluted nitric acid to remove the iron particles from the surface. Later, during the use of the casing, it is important to clean thoroughly and to rinse with clean water all surfaces that may come into contact with chloride ions.

## 5 REFERENCES

- <sup>1</sup> Leonardo S. Andrade, Sandro C. Xavier, Romeu C. Rocha-Filho, Nerilso Bocchi, Sonia R. Biaggio, Electropolishing of AISI-304 stainless steel using an oxidizing solution originally used for electrochemical coloration, *Electrochimica Acta*, 50 (2005) 13, 2623–2627
- <sup>2</sup> Z. Szklarska-Smialowska, Pitting corrosion of metals, Houston, NACE, TX, 1986, 143–157
- <sup>3</sup> A. Kocijan, Č. Donik, M. Jenko, Electrochemical and XPS studies of the passive film formed on stainless steel in borate buffer and chloride solutions, *Corrosion Science*, 49 (2007) 5, 2083–2098
- <sup>4</sup> M. F. Montemor, A. m. p. Simões, M. G. S. Ferreira, M. Da Cunha Belo, The role of Mo in the chemical composition and semi-conductive behaviour of oxide films formed on stainless steels, *Corrosion Science*, 41 (1999) 1, 17 – 34
- <sup>5</sup> A. Frontini, I. Milošev, B. Pihlar, Vpliv vsebnosti molibdena na biokompatibilnost nerjavnega jekla, Kovine zlit. tehnol., 33 (1999) 3–4, 185–188
- <sup>6</sup> R. R. Maller, Passivation of stainless steel, *Trends in Food Science & Technology*, 18 (2007) 1, S112–S115
- <sup>7</sup> Torkar, M., Corrosion of AISI 316 Ti in 50% KOH due to deformation induced martensite. *Eng fail. anal.* 13 (2006) 4, 624–628
- <sup>8</sup> M. G. Fontana, N. D. Greene, *Corrosion Engineering*, 1978, 2<sup>nd</sup> Edition, McGraw Hill, New York
- <sup>9</sup> Reference database of binding energies: <http://srdata.nist.gov/xps/>



## USING A FIB TO PREPARE Al(OH)<sub>3</sub> SAMPLES FOR THE TEM

### UPORABA FIB ZA PRIPRAVO VZORCEV Al(OH)<sub>3</sub> ZA TEM

Irena Nikolic<sup>1</sup>, Velimir Radmilovic<sup>2</sup>, Toll Z. Sholklapper<sup>3</sup>, Dragoljub Blečić<sup>1</sup>

<sup>1</sup> University of Montenegro, Faculty of Metallurgy and Technology, 81000 Podgorica, Montenegro

<sup>2</sup> LBNL, NCEM, MS-72, University of California, Berkeley, CA 94720, USA

<sup>3</sup> LBNL, MSSM, University of California, Berkeley, CA 94720, USA

irena@cg.ac.yu

Prejem rokopisa – received: 2007-09-25; sprejem za objavo – accepted for publication: 2007-10-23

One of the basic applications of a focused ion beam (FIB) tool is the preparation of samples for transmission electron microscopy (TEM) analysis. A dual-beam FIB system combines multiple experimental systems within the same chamber and the combinations of different techniques can be accommodated by unique sample preparation, manipulation and analysis methods. The system contains both the focused Ga<sup>+</sup> ion beam and a field-emission scanning electron column. In this paper we described a procedure for preparing Al(OH)<sub>3</sub> samples for TEM analysis using a FIB.

Key words: focused ion beam, Al(OH)<sub>3</sub>, milling, deposition, sample preparation

Ena od temeljnih vrst uporabe fokusiranega ionskega curka (FIB) je priprava vzorcev za presevno elektronsko mikroskopijo. Dualni FIB-sistem kombinira v isti komori več eksperimentalnih sistemov, kombinacija različnih tehnik pa omogoča enkratno pripravo vzorcev, manipulacijo in analizo. Sistem ima oboje: fokusirani in ozki curek Ga<sup>+</sup> in vrstično elektronsko kolono s poljsko emisijo. V članku je opisan postopek uporabe FIB za pripravo vzorcev Al(OH)<sub>3</sub> za presevno elektronsko mikroskopijo.

Ključne besede: fokusirani ionski curek, Al(OH)<sub>3</sub>, mletje, depozicija, priprava vzorcev

## 1 INTRODUCTION

The two main features of the FIB tool are the capability to remove material from the sample by sputtering (micro-machining) and to add materials to the sample by depositing at sub-micron dimensions. There are a wide variety of applications for a FIB, but they can be segmented into three main categories <sup>1-3</sup>, i.e.,

- IC review and modification, where sputtering is used to create a cross-section or modification to the sample, and where cutting is desired together with the deposition of either metallic or insulating materials to either modify existing structures or to create new structures.
- TEM and STEM sample preparation, where the FIB is used to form a thin slice of material by sputtering trenches on either side of a slice.
- Producing thin-film specimens.

In this paper we explain a step-by-step approach to preparing samples of Al(OH)<sub>3</sub> for an investigation with transmission electron microscopy using an FEI Strata Dual Beam FIB. Investigating the mechanism of Al(OH)<sub>3</sub> crystal growth required the use of both scanning and transmission electron microscopy (SEM and TEM). The data obtained with the SEM are not sufficient to draw a reliable conclusion about the mechanism of Al(OH)<sub>3</sub> growth, with respect features such as twinning, and a determination of the twinning plane and direction. This means that TEM is required and a special way of preparing samples for such an investigation needs to be developed.

## 2 EXPERIMENT

The crystals of Al(OH)<sub>3</sub> were obtained by a crystallization process from a caustic soda solution. They crystallized in the form of small particles joined together in larger agglomerates. When such particles were exposed to the ion beam, they started to dissipate. In order to prevent the dissipation process we put Al(OH)<sub>3</sub> powder in the cannon mod and then filled it up with liquid epoxy. The vacuum, liquid epoxy filled up all the vacancies inside the Al(OH)<sub>3</sub> crystals. After 12 h the epoxy was solidified and made the particle interior stronger. After this, the cannon samples were polished in order to remove excess epoxy and coated with gold so they were conductive. The samples prepared in such a way were ready for the FIB treatment.

## 3 DISCUSSION

The preparation of the Al(OH)<sub>3</sub> sample for the TEM analysis using the FIB was carried out in the National Center for Electron Microscopy, Lawrence Berkeley Laboratory, University of Berkeley, California. A picture of the FIB is shown in the **Figure 1**.

**Figure 2** shows a step-by-step approach to the preparation of a sample for transmission electron microscopy using the selective focused ion beam (FIB) milling technique.

After the area of interest is found, the first step is the deposition of platinum. The platinum is deposited, either under an ion or electron beam, in the strip with dimensions of approximately 25 x 1 x 2) µm (length,



**Figure 1:** FEI Strata Dual Beam FIB in NCEM LBNL, University of California, Berkeley

**Slika 1:** Strata dualni curek FIB pri NCEM LBNL, Univerza v Kaliforniji, Berkeley

width, height). We used an ion beam with a beam current corresponding to double the area of the deposition (**Figure 2a**).

The next step is milling of the cleanup trenches on both sides of a platinum strip (**Figure 2b**). Before the milling procedure begins, the milling stair step pattern needs to be defined in terms of shape and position. The shape of the stair-step pattern is shown in **Figure 3**,<sup>1</sup>

The milling procedure consists of two steps. A large beam current (20 000 pA) is used in the first step of the bulk removal with the aim to reduce the time of milling when the ion beam is positioned far from the platinum strip. In the next step, after the bulk of the material has been removed, the face of the specimen slice must be cleaned up using a lower beam current. Again, a stair step pattern must be defined. After the final milling the platinum strip must retain the defined thickness.

After the final milling is finished, the sample is tilted by 45° in order to make a cross-section of the obtained sample slice. Under a beam current of 7000 pA a thin slice of the specimen is cut free from the three sides leaving a small "bridge" in the upper-left corner (**Figure 2c**).

In the next stage (**Figure 2d**), the sample stage in the chamber (z-position) is lowered (to avoid any needle damage) and a platinum needle is inserted into the chamber. Then, the sample stage is raised again. Using a manipulator the Pt needle is navigated and attached to the free upper (right) corner. The needle is welded to the specimen slice by depositing platinum in the same way as in the case of the deposition of a platinum strip. For this test a smaller pattern (approximately (1x1) µm) and a lower beam current were used. Finally, the remaining bridge connecting the slice sample to the sample bulk is cut free using the 300 pA beam current. In the next step the sample stage in the chamber must be lowered slowly to lift out the membrane – the thin specimen slice.

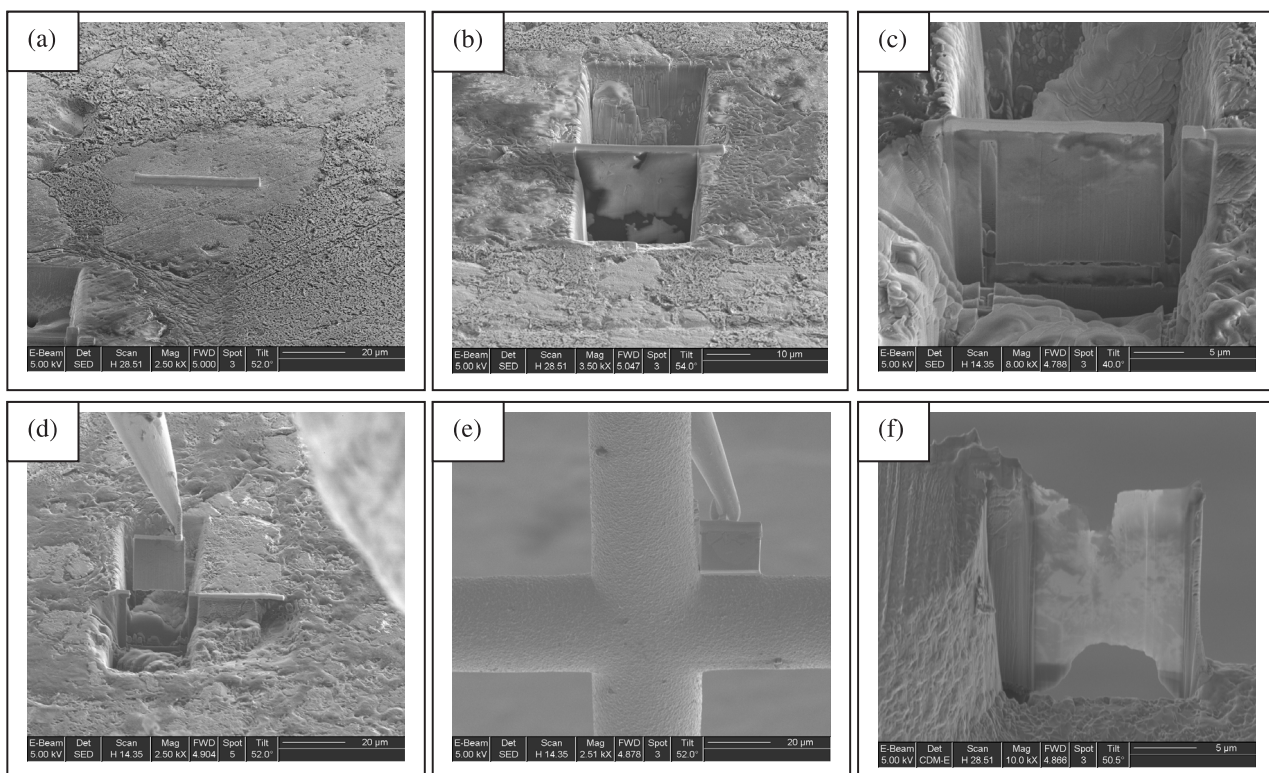


**Figure 2:** Step-by-step approach to preparing Al(OH)<sub>3</sub> samples for TEM using a FIB

**Slika 2:** Stopnje priprave vzorcev za TEM z uporabo FIB

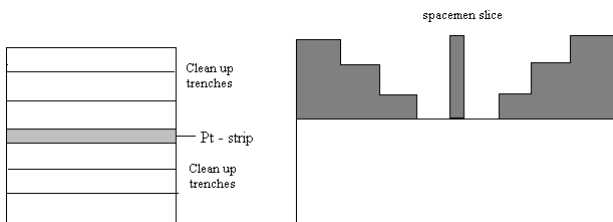


**Figure 3:** Shape of stair-step pattern used for the bulk removal of material

**Slika 3:** Shema stopničastega načina odvzema materiala

The last sequence is welding the membrane to the half-cut copper grid. Prior to this the copper grid is placed in the holder in the chamber and aligned horizontally. The membrane is then placed in a pre-milled trench located near the flat side of the grid and welded to the grid with platinum deposition (**Figure 2e**). When the membrane is welded to the grid, the platinum needle is cut free from the membrane. After this step the specimen slice is still too thick for any TEM analysis and the bulk of the FIB dust (the result of milling) is present on the surface of the membrane. Thus, a final thinning on the grid is necessary and, indeed, vital; this is the last step in the preparation of the Al(OH)<sub>3</sub> sample for TEM analysis. There is, however, a final step; it is good practice to let the ion beam scan (for a short time) the thin section using a low beam current (50–100 pA). The picture of the sample after the final thinning on the grid is shown in **Figure 2f**. Such a thin sample (about 50 nm) is appropriate for a TEM investigation.

## 4 CONCLUSION

The application of a focused ion beam in the preparation of Al(OH)<sub>3</sub> crystals for TEM is shown to be a good technique. Problems related to the dissipation of Al(OH)<sub>3</sub> particles under the ion beam can be successfully avoided by using epoxy. A general problem related to the FIB technique is the re-deposition of dust (removed material) during the milling step. In addition, the problem that may occur during the preparation of the sample for the TEM analysis is related to the last steps when the sample slice is very thin and the handling needs to be very delicate. The procedure of cleaning the sample slice on the grid must be carefully performed with the choice of an appropriate beam current. The lower beam current is recommended, as is the repetition of the cleaning procedure several times until the desired sample thickness is achieved. If the sample is too thin the sample slice may break.

## 5 REFERENCES

- <sup>1</sup>J. Orloff, M. Utlaut, L. Swanson, High Resolution Focused Ion Beams: FIB and Its Applications, Kluwer Academic /Plenum Publishers, New York, 2003
- <sup>2</sup>L. A. Giannuzzi, F. A. Stevie, Introduction to focused ion-beams: instrumentation, theory, techniques and practice, Springer, New York, 2005
- <sup>3</sup>Z. Rahman, S. Shkula, H. Cho, S. Seal: Microscopy and Analysis, 20 (2006) 3, 11–13

